POLITECNICO
MILANO 1863

SCUOLA DI INGEGNERIA INDUSTRIALE
E DELL'INFORMAZIONE

Molecular Excitons in Dielectric Metasurfaces

MASTER OF SCIENCE IN
MATERIALS ENGINEERING AND NANOTECHNOLOGY -
INGEGNERIA DEI MATERIALI E DELLE NANOTECNOLOGIE

[1]CENTER FOR NANOSCIENCE AND TECHNOLOGY, (IIT), MILAN
[2]CENTRE FOR DISRUPTIVE PHOTONIC TECHNOLOGIES,
NANYANG TECHNOLOGICAL UNIVERSITY, SINGAPORE

Author: Marco Marangi

Student ID: 964537
Supervisor: Prof. Guglielmo Lanzani[1]
Co-supervisor: Prof. Cesare Soci[2]
Academic Year: 2021-2022

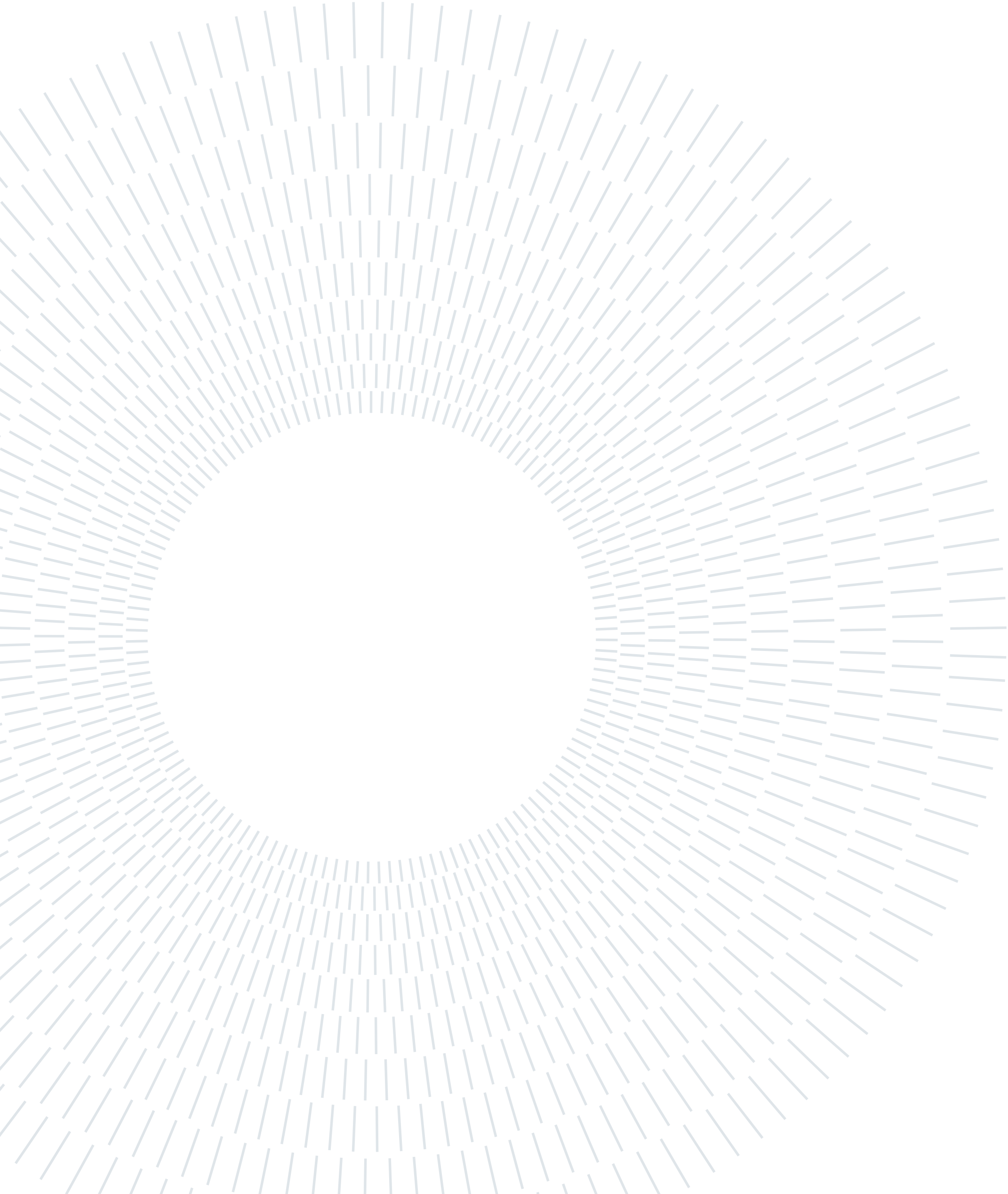

Abstract

J-aggregates, consisting of coupled molecular emitters in which the dipole transition moments are naturally aligned, are quantum systems capable of manifesting cooperative behavior leading to an intense burst of highly directional emission [17]. This phenomenon, known as superradiance, has been predicted in theory but its emergence under experimental conditions is hard to achieve. Previous attempts to stimulate superradiance have been attempted by coupling quantum emitters to plasmonic structures [35], but their intrinsically lossy nature in the visible range has not provided stable enough grounds to induce such cooperative behaviour.

In this work, dielectric metasurfaces have been designed to resonantly enhance the emission of a J-aggregate thin film by Purcell effect [54] and impart tunable direction to the emission. Compared to plasmonic systems, the dielectric nature of the nanoresonators makes them a suitable resonant system to induce superradiance due to their intrinsically low losses and high refractive index in the range of emission investigated. The role of the metasurface in this work is to confine and enhance the electromagnetic field of the incoming excitation so that the photonic bands of the metasurface can be populated by the emitted photons from the J-aggregates. Once the photonic bands are populated, the previously isotropic molecular exciton will be imparted with directional emission.

Evidence of coupling between the molecular aggregate thin film and the dielectric metasurface is shown through both numerical simulations and experimental angle-resolved photoluminescence measurements. The possibility to further extend this work towards highly directional polaritonic devices is discussed, along with the role that the resonant dielectric metasurface could have in fostering superradiance.

Our results suggest that coupling J-aggregates with designer dielectric metasurfaces offers a new way to control the radiative properties of exciton-polaritons in cooperative molecular systems and could lead to the development of ultrabright and fast-switchable light-emitting devices based on the phenomenon of superradiance.

Keywords: nanophotonics, metasurfaces, exciton-polaritons, J-aggregates, superradiance

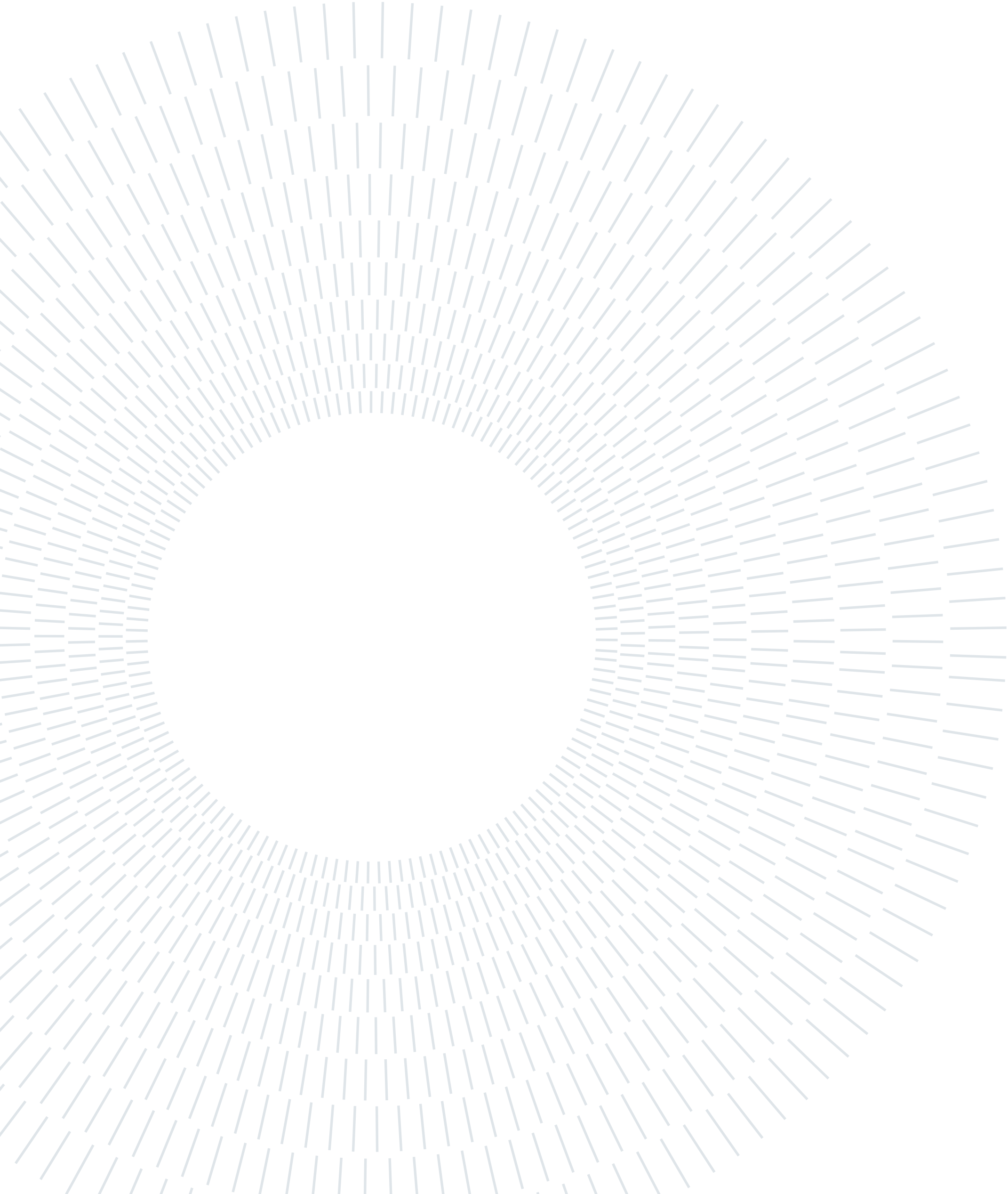

Abstract in lingua italiana

Gli aggregati molecolari di tipo J, composti da emettitori molecolari accoppiati i cui momenti di transizione dei dipoli sono naturalmente allineati, sono stati teoricamente dimostrati essere sistemi quantistici in grado di manifestare un comportamento cooperativo che porta ad un'intensa emissione altamente direzionale [17]. Questo fenomeno è noto come "superradiance" e, sebbene possibile in teoria, la sua emergenza in condizioni sperimentali è difficile da dimostrare.

In questo progetto, una serie di metasuperfici dielettriche sono state progettate per incrementare l'emissione di uno strato sottile di aggregati J mediante l'effetto Purcell [54] e per controllare la direzionalità di emissione. La natura dielettrica dei nanorisonatori li rende un candidato ideale per questo ruolo a causa delle loro basse perdite ed alto indice di rifrazione nello spettro del visibile. Il ruolo della metasuperficie in questo lavoro è quello di confinare il campo elettromagnetico dell'eccitazione in modo che le bande fotoniche della metasuperficie possano essere popolate dai fotoni emessi dagli aggregati molecolari. Una volta popolate le bande fotoniche, i fotoni che precedentemente non manifestavano alcuna dipendenza dall'angolo di emissione assumono una più marcata direzionalità.

Prove dell'interazione tra lo strato sottile di aggregati molecolari e la metasuperficie dielettrica sono presentate sia attraverso simulazioni numeriche che mediante misure di fotoluminescenza angolare. Viene inoltre discusso il possibile sviluppo di dispositivi polaritonici altamente direzionali ed il ruolo che le metasuperfici potrebbero avere nella promozione della "superradiance".

I nostri risultati suggeriscono che l'interazione tra aggregati molecolari e metasuperfici dielettriche sia un nuovo modo per controllare le proprietà radiative degli eccitoni-polaritoni negli aggregati molecolari e potrebbe portare allo sviluppo di dispositivi ad emissione intensa e rapida basati sul fenomeno della "superradiance".

Parole chiave: nanofotonica, meta superfici, polaritoni, aggregati J, superradiance

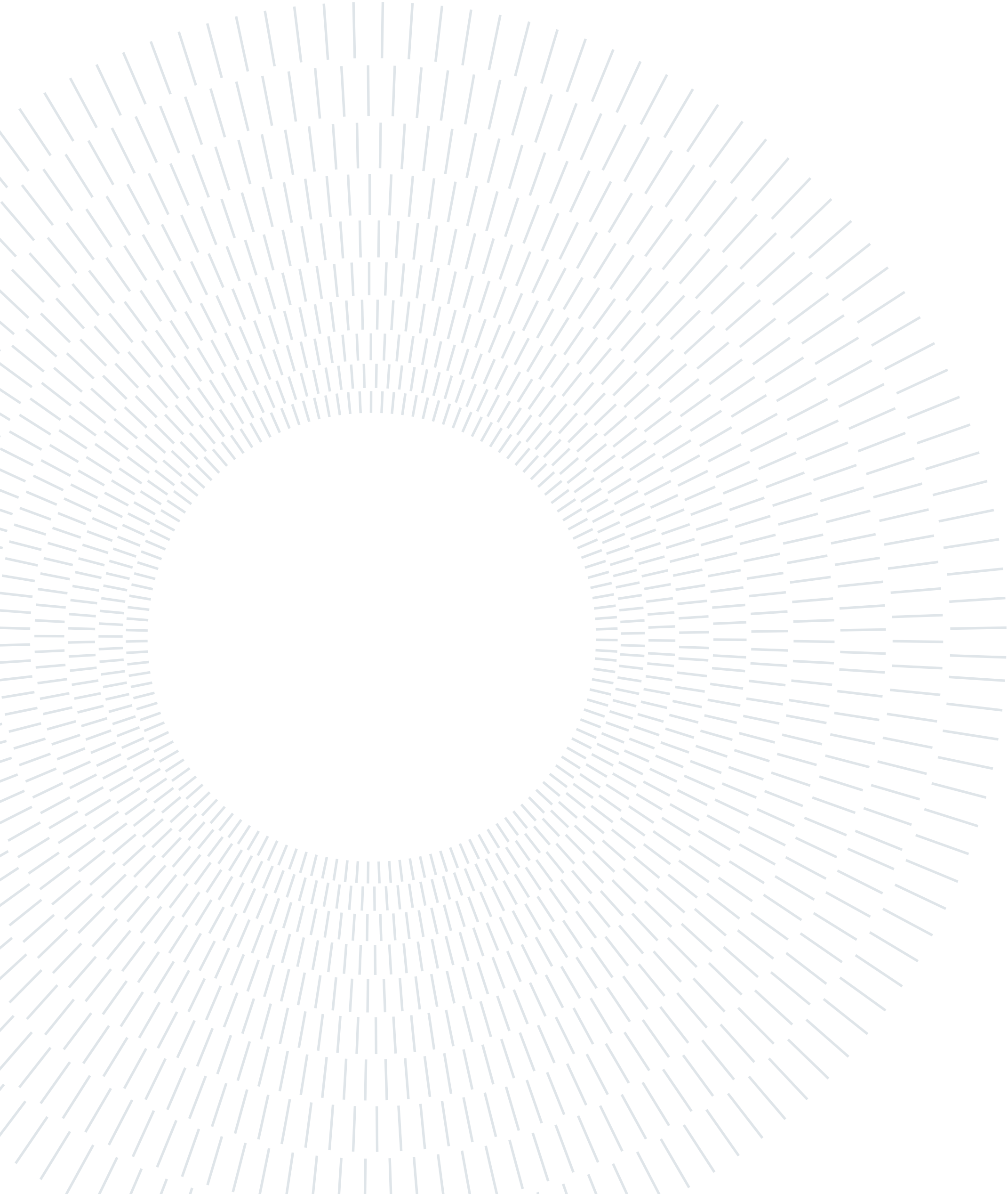

Contents

Abstract i

Abstract in lingua italiana iii

Contents v

1 Introduction 1

2 Theoretical Background 3
- 2.1 Dielectric Metasurfaces 3
- 2.2 Molecular Excitons 5
  - 2.2.1 Introduction to Superradiance 7

3 Metasurface Design 11
- 3.1 Numerical Simulation Methods 11
  - 3.1.1 Finite-Difference Methods 11
- 3.2 Optical Resonances 16
- 3.3 Design Process 17
  - 3.3.1 Critical Geometrical Feautures 17
  - 3.3.2 Mie Resonances 18
  - 3.3.3 Quasi-Bound States in the Continuum 30
  - 3.3.4 Quality Factor 35

4 Materials and Methods 37
- 4.1 Materials 37
  - 4.1.1 Sputtering of TiO_2 thin films 37
  - 4.1.2 Synthesis and Deposition of TDBC Thin Films 38
- 4.2 Nanofabrication of Dielectric Metasurfaces 43
  - 4.2.1 Electron Beam Lithography of TiO_2 [53] 43
  - 4.2.2 Dry Etching of TiO_2 47

5 Experimental Results and Discussion **51**
5.1 Characterization of Dielectric Metasurfaces 51
5.1.1 Normal-incidence Transmittance 51
5.2 Characterization of J-Aggregates Thin Films 55
5.2.1 Photoluminescence as a Function of Pumping Power 55
5.3 Characterization of the Coupled System 58
5.3.1 Angle-resolved Photoluminescence Measurements 58

6 Conclusions and Future Work **65**

Bibliography **67**

List of Figures **75**

List of Tables **81**

Acknowledgements **83**

1 | Introduction

The interaction between light and matter has been an area of interest due to its broad range of applications, including biosensors, sub-diffraction limit imaging, quantum information processing [71], ultralow-threshold lasing [40], ultrafast all-optical circuits, among many others [21, 36, 38, 58]. With recent advancements in nanoscale fabrication techniques, complex structures can now be designed to interact with light in a variety of ways. Notable examples that will be explored in this work include the amplification of emission (or absorption) via Purcell effect, and the achievement of weak to strong coupling leading to the formation of exciton-polariton quasi-particles.

One major challenge is the choice of materials for such devices. Metals have traditionally been used to fabricate metasurfaces, and although the field of plasmonics allows the formation of strong surface plasmon-polaritons [64, 66], they also suffer from considerable Ohmic losses in the visible range. Additionally, even though the enhancement of emission at room temperature has been shown to be feasible for a variety of emitters, achieving strong coupling at room temperature is not as easy and working in the visible range poses further challenges in the fabrication process due to the reduced size of the resonators. This is the case for a variety of reasons, including the strict fabrication tolerances required to obtain high quality factor resonant cavities, the naturally noisy environment at room temperature, and the generally higher dissipative losses at lower wavelengths of most materials.

The next logical step for the development of room-temperature polaritonic devices in the visible range is to switch the focus to dielectric materials. Although this field has been rapidly developing and has already achieved outstanding results in terms of high Q-factor cavities [35, 42, 55], the implementation of these structures into more complex polaritonic devices at room temperature and in the visible range has yet to be thoroughly explored. At the same time, close attention must also be given to the excitonic side of the device, so as to reduce exciton-related bottlenecks (e.g. coherence length, saturation, photobleaching, etc..) in the performance of the complete device.

The specific materials that will be used throughout this manuscript are TiO_2 as the dielectric metasurface and TDBC (cyanine dye J-aggregate) as the emissive counterpart.

Current state-of-the-art metasurfaces are capable of enhancing signals via the Purcell effect and achieving strong coupling with a variety of emitters. However, there are still several challenges that must be addressed to develop hybrid devices that operate at room temperature and in the visible spectrum. These challenges include the need for better emitters, less dissipative metasurfaces, and more precise nanofabrication techniques.

J-aggregates and photonic dielectric metasurfaces have already been extensively explored in their respective fields and have numerous standalone applications. However, integrating these two fields remains a challenge that has not yet been extensively explored. This could be attributed to the experimental challenges associated with controlling the spatial position and orientation of the quantum emitter within the metasurface [18].

A variety of simulations and experimental measurements will be presented throughout this work, in order to prove that dielectric metasurfaces are ideal candidates to serve as a fully controllable substrate to tune the radiative properties of molecular excitons.

This thesis aims to address the challenges of developing room temperature molecular excitonic devices that can achieve both weak and strong coupling in the visible range. To achieve this, appropriate materials will be selected, metasurface designs will be developed while accounting for fabrication tolerances, and the optical properties of the emissive material will be fine-tuned through supramolecular chemistry. These steps will allow the control of both sides of the exciton-polariton, resulting in easy-to-fabricate and efficient devices with tunable radiative properties. Additionally, J-aggregates have been demonstrated to be intrinsically coherent emitters and possibly prime candidates to exhibit superradiance [17], an experimentally elusive phenomenon in which the subunits of a quantum system interact constructively leading to a strong, highly directional and ultrafast pulse of light. With this in mind, our work provides insights and paves the way towards utilizing dielectric metasurfaces to foster cooperative behaviour in J-aggregates.

This thesis aims to provide novel insights regarding the design and uses of dielectric metasurfaces/molecular aggregates hybrid devices through both simulated and experimental results. The findings of this study will provide solid foundations for future research on fostering superradiance in J-aggregates and experimental evidence of the possibility of tuning the radiative properties of molecular excitons through the use of dielectric metasurfaces.

2 | Theoretical Background

2.1. Dielectric Metasurfaces

In recent years, studying light-matter interactions has been at the centre of attention for many researchers due to the possibility of controlling light-confinement on the nanoscale. Recent advances in nanofabrication have made this into a reality, leading researchers to both design and fabricate nanostructured materials that can control and enhance the electromagnetic field distribution of light in a variety of ways.

The whole idea is based on the principle of light scattering with structures of size comparable to the incoming wavelength, which according to Mie theory causes strong scattering resonances both in metallic and dielectric structures. In its simplest form, Mie theory tells us that the scattering phenomena associated to a material will depend on its permittivity and a size parameter defined by the geometry of the object. Intuitively, the response of a metallic material will differ from that of a dielectric, the reason being that the dielectric permittivity has opposite signs for the two [11].

Typically, the interaction between light and a metallic particle whose size is comparable to that of the incoming radiation causes an electric response from the particle that can be associated to a so-called localized surface plasmon resonance. While the interaction with a dielectric particle can generally cause both an electric and magnetic response according to the specific displacement currents generated in the material.

Plasmonic resonators have long been employed in the field of signal enhancement due to their capability to efficiently confine the electric field to small volumes and thus have small mode volumes in correspondence of the plasmonic resonance. These systems have been shown to reach Purcell factors of up to a thousand [8], but are still heavily limited by the low radiation efficiency bottleneck caused by their considerable Ohmic losses, particularly in the visible range [18]. The problem with metallic resonators becomes evident by analysing the formula for the Purcell factor [54]

$$F_P = \frac{3}{4\pi^2}\frac{\lambda^3}{n^3}\frac{Q}{V}.$$

Although the reduced mode volume (V) that can be obtained with metals has a positive effect on the enhancement of emission, the Ohmic losses greatly diminish the Q-factor of the cavity.

Based on this it should become evident why high refractive index dielectric materials have generated so much interest in the last decade. Multiple studies that have shown how the high real refractive index and low dissipative losses of these materials can lead to high quality factor nanostructures that work for a variety of resonances [35, 42, 55].

It is very common in literature to refer to such structures as resonators or nanoantennas [51] due to their ability to shape the electric and magnetic fields of an incoming radiation, as well as to increase its intensity in space in a controllable manner.

The type of response and its strength strongly depend on the refractive index of the material and, up to a certain extent, of the surrounding volume. It is also heavily affected by the specific geometry of the object, modifying the geometrical features of the resonator will inevitably alter the relative spectral position of the resonances involved as well as its optical character [44, 61].

The concepts discussed until now are valid for single particle studies, while their extension to periodic arrays of resonators requires more attention. The periodic repetition in space of a planar pattern of resonators within subwavelength thicknesses is known as a metasurface [73]. In these structures the optical response of the bulk pattern will differ from that of the single resonator, hence the design criteria between the two will differ even though all that has been mentioned above regarding size and permittivity still holds true. The base concept of light interacting with a scatterer also remains present in metasurfaces, but the presence of multiple resonators that interact with the same incoming radiation allows for more freedom in the design process and a variety of possible applications. When working with metasurfaces, the spacing between single nanoantennas, the relative orientation between both other resonators and the incoming radiation will all influence the optical response of the material.

The design flexibility of metasurfaces allows researchers to accomplish impressive feats such as wavefront shaping [67, 68], nearly perfect absorption, reflection or transmission, induced polarization [29] and chirality [59], high quality factor cavities [19], along with many more applications [21, 36, 38, 58].

It should also be noted that working with a large number of resonators, designing for a specific resonance wavelength becomes a sensitive task due to the potential impact of fabrication tolerances and error propagation. Fabrication defects can affect not only a single resonator but can also propagate throughout the pattern, leading to errors that shift the resonance wavelength and reduce its strength. Despite recent advances in fabrication techniques that have reduced the presence of such artifacts, the complexity of the fabrication process inevitably increases when moving to visible wavelengths due to the reduced size of the resonators.

While it is possible to design a metasurface to be less sensitive to fabrication tolerances, achieving high quality factor cavities in the visible spectrum remains a relatively new and challenging field. The sensitivity to fabrication tolerances is a significant obstacle to overcome, especially when working with visible light, as the requirements for precision increase. Further advances in fabrication techniques are necessary to achieve more robust and reliable metasurfaces in the visible spectrum [5].

2.2. Molecular Excitons

J-aggregates are a class of molecular aggregates constituted by highly ordered molecular assemblies of dyes or other chromophores, in which the units are arranged in a one-dimensional chain-like structure that allows the strong electronic coupling between its subunits. This can result in unique optical properties such as enhanced absorption, emission, and circular dichroism [33, 37].

The J-band peak red-shifted from the one associated to its monomeric form emerges from the excitonic coupling between the units in the aggregate (Figure 2.1), resulting in a delocalized excitonic state of great intensity. What separates these structures from other emissive materials is that the J-band that arises from aggregation is drastically red-shifted (up to roughly 100 nm), highly symmetric and with narrow linewidths (10-15 nm). Additionally, the Stoke shift between absorption and emission is quite small due to their rigid structure, making them interesting candidates as both absorbing and emissive materials when coupled to structures that are generally designed to affect only one of the two phenomena.

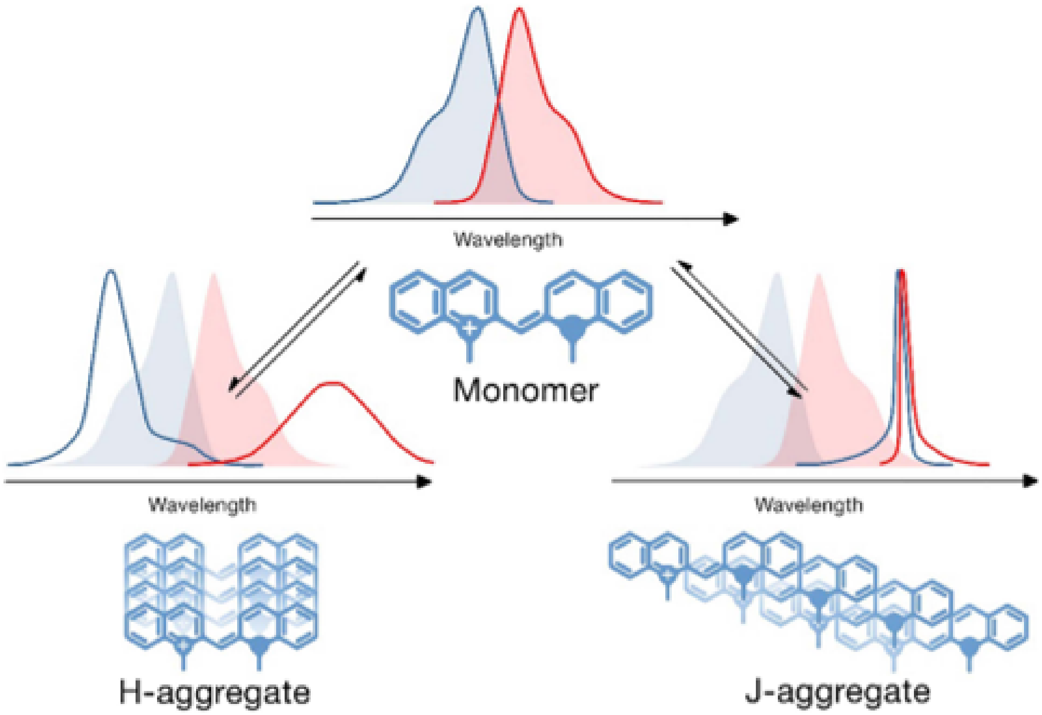

Figure 2.1: Schematic representation of the spectral changes following the formation of H- and J- aggregates in cyanine dyes [37].

As already mentioned, the ordered self-assembled structure of J-aggregates allows for the formation of delocalized excitonic states spanning over multiple subunits. Within the framework of molecular excitons developed by Davydov [16], the strong electronic interactions between the monomeric units are translated into a coherent oscillation shared between multiple units of the aggregate. Under these conditions, the radiative decay of emissive states is enhanced leading to an increase in the rate of emission of the aggregates. Surprisingly, the same phenomenon can be further enhanced under more restrictive conditions such as low temperatures and low local disorder [50], allowing cooperative behaviour between the units and thus a collective response of the aggregate when excited. Classically this can be seen as a collection of dipoles oscillating in phase forming a large collective dipole with amplitude given by the constructive interference between the interacting unit dipoles [22].

This culminates into a decay rate that is proportional to the number of coupled monomers [24] and a strong dependence on pumping power for their photoluminescence intensity. This phenomenon is an extension of the concept of “superradiance” introduced by R. H. Dicke in 1953 for which J-aggregates appear to be perfect candidates due to their highly ordered molecular structure [17].

J-aggregates can be formed by a wide range of dyes and chromophores, including cyanine dyes, porphyrins, phthalocyanines, and others. The formation of J-aggregates is influenced by a number of factors, including the chromophore structure, the solvent polarity, and the aggregation conditions. In general, J-aggregates are favored in non-polar solvents and at high chromophore concentrations, where the intermolecular interactions between chromophores are strong enough to overcome any repulsive forces, but the aggregation pathway is strongly dependent on the specific aggregate and the environmental conditions mentioned above, as is usually found for many other self-assembled structures.

The optical properties of J-aggregates make them an attractive emissive material for a wide range of applications, including sensing, imaging, and optoelectronics. J-aggregates have been used as fluorescent probes for biomolecules and cells, as well as for the detection of environmental pollutants. They have also been incorporated into organic solar cells and light-emitting diodes, where their unique optical properties can improve device performance.

Currently, researchers are actively exploring ways to control the formation and morphology of J-aggregates [25] in order to be able to exploit their astounding unique optical properties in more complex systems in tandem with other materials [7, 12, 48, 48, 52, 72].

2.2.1. Introduction to Superradiance

R.H. Dicke introduced the phenomenon of superradiance, which is based on the idea that molecules interacting within a shared radiation field cannot be considered as independent oscillators, and their radiative behavior will be influenced by their degree of coherence [17].

Initially developed for gas molecules, Dicke's results have been extended to any system with a magnetic or electric dipole transition that has the capability of radiating. The peculiarity of this phenomenon is that the dipole moment of the ensemble of radiating objects is given by the sum of the expectation values of each dipole moment. Additionally, such systems will radiate coherently in the direction of excitation since all the other components will interact to cause transitions to states of lower cooperation number.

The sequence of photons emitted by these systems is known to possess angular correlation. It has been demonstrated that the probability that all subsequent photons emitted by the system after being excited in a generic direction (k) is twice the probability averaged over all other directions as shown by $I(k_s) = I_0(k_s)\frac{P_s(\frac{1}{2}+m_0-s+1)}{P_{s-1}(n-s+1)}$. This is to say that in the presence of an oscillating collective dipole the angular distribution of a generic photon is dependent on the direction of the previously emitted photon and its probability scales with the number of photons previously emitted in the same direction.

The first definitive experimental evidence of superradiant emission has been demonstrated by Hettich et al. [27] in a system made up of two terylene molecules embedded in a p-terphenyl crystal at a distance of 12 nm. The two molecules showed distinct one-photon resonances at low pumping powers, while a third peak roughly located at the middle frequency of the two one-photon resonances appeared by increasing the pumping power (Figure 2.2). This phenomenon has been associated to the simultaneous excitation of the two molecules through a two-photon process, the first evidence of nonlinear cooperative behavior between two molecules. The same study also observed the arisal of photon antibunching for both one-photon emission and photon bunching for the cooperative two-photon resonance, confirming the entanglement between the two molecular eigenstates and thus their cooperativity.

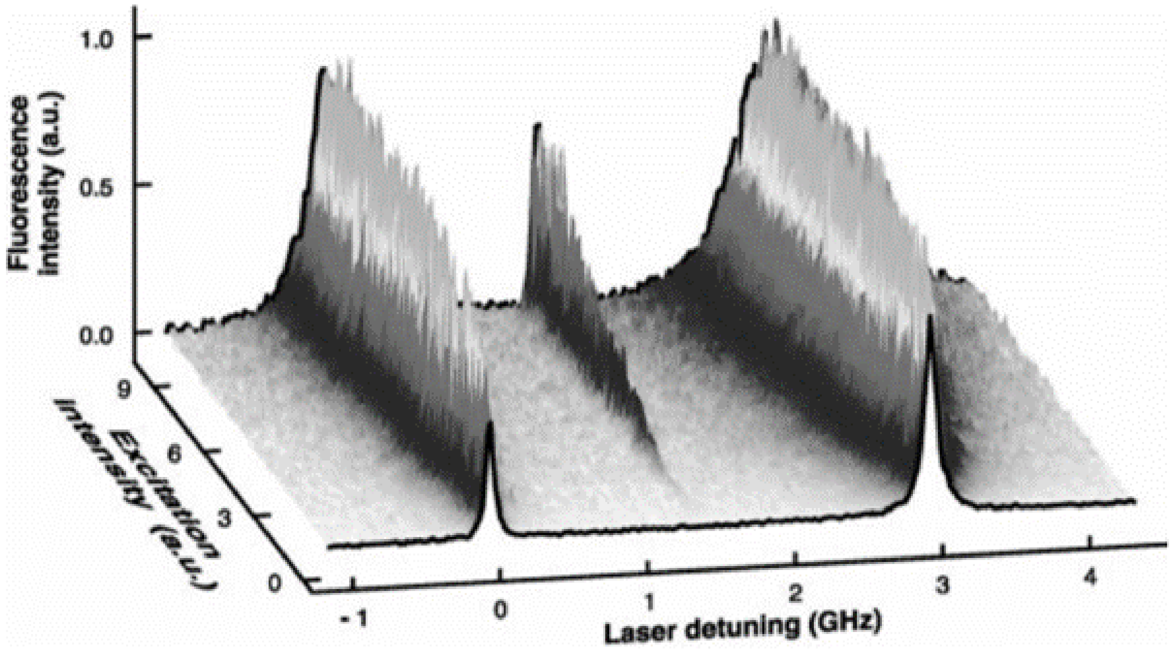

Figure 2.2: Fluorescence spectra of two coupled terrylene molecules as a function of pumping power, showing the arisal of a pump fluence dependent peak associated with the emergence of cooperative emission [27].

Following Dicke's paper, in the past few decades researches have confirmed the validity of Dicke's model and have further developed more advanced theoretical frameworks [13, 20, 23, 46].

As briefly mentioned above, the requirements to achieve superradiance experimentally are quite restrictive since local disorder, inhomogeneous broadening, and temperature-related phenomena have been shown to disrupt the conditions for cooperativity both in theory and in practice [50] by causing dephasing between the many oscillating dipoles and thus a reduction of coherence within the system. Regardless of it being a challenging phenomenon to observe, claims of superradiant behaviour have been reported in literature during the past few years. The concept of cooperativity between oscillating dipoles has been extended to a variety of materials such as H-Aggregates [47] and other organic systems [63], quantum dots [30, 32, 56], and perovskites thin films [9].

From a purely theoretical standpoint, a superradiant system will show the following three phenomena simultaneously: an increase in the decay rate of emission, a burst in the cavity mode population, and a non-linear (often a power law with exponent between 1 and 2) dependence of the maximum of photoluminescence from the number of coupled emitters [46].

Experimentally the two fingerprint signals that identify superfluorescence are non-linearity of emission in pump fluence measurements, and photon bunching, both typical of strongly coupled systems of quantum emitters. It is also very common to perform time-resolved measurements to highlight the enhanced decay rate of superradiant emissive states which has been shown by many theoretical models to be a direct consequence of cooperativity, although it cannot always be univocally attributed to coupled emitters when dealing with more complex systems such as plasmonic or dielectric metasurfaces or cavities that are known to affect the radiative behaviour of emitters by Purcell effect. Hence the latter should be paired with some of the other above mentioned techniques to be univocally attributed to superfluorescence.

Overall, achieving superradiance experimentally and being able to foster its arisal at room temperature is a field of great interest due to the possibility to exploit it to create ultrafast, highly selective and directional emitters for applications in a variety of fields such as bio-imaging, multi-photon high-brightness quantum light sources, as well as in fields on the rise such as optical and quantum computing.

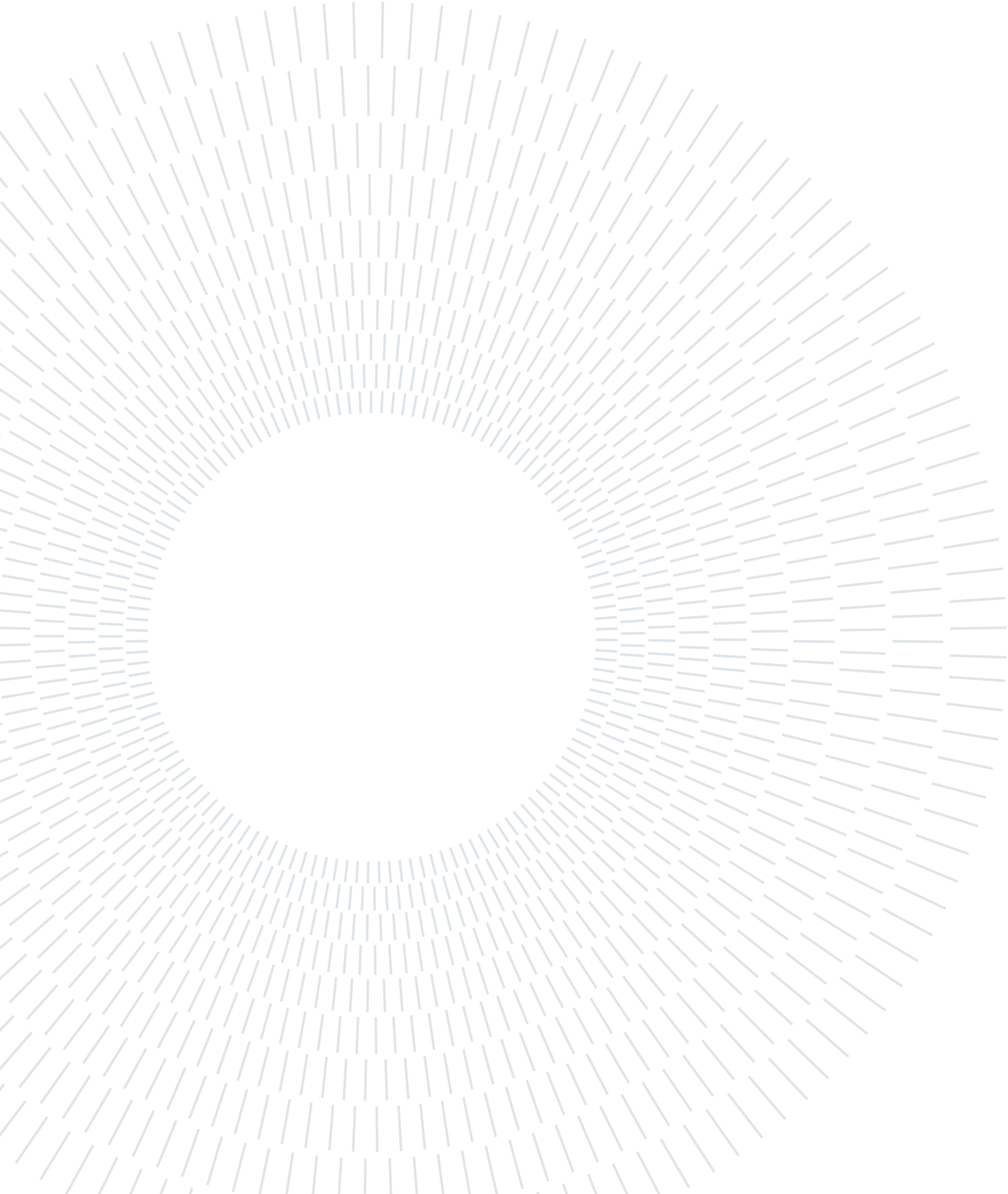

3 | Metasurface Design

3.1. Numerical Simulation Methods

3.1.1. Finite-Difference Methods

Lumerical Finite-Difference Time-Domain

Finite-difference time-domain or FDTD for short is a numerical analysis method developed by Kane S. Yee to compute electrodynamics in the time-domain. More specifically, FDTD approximates the solutions for the time-dependent Maxwell's equations by defining space as a discretized grid and then solving the local partial differential equations at each instant of time. This procedure works because the electric field in every point in space is computed at a time instant that precedes the computation of the magnetic field, thus respecting the dependence on the former from the latter, as stated by Maxwell's equations (3.1)[62].

$$\begin{cases} \nabla \cdot \boldsymbol{D} = \rho, \\ \nabla \times \boldsymbol{E} + \dfrac{\partial \boldsymbol{B}}{\partial t} = \mathbf{0}, \\ \nabla \cdot \boldsymbol{B} = 0, \\ \nabla \times \boldsymbol{H} - \dfrac{\partial \boldsymbol{D}}{\partial t} = \boldsymbol{J}. \end{cases} \tag{3.1}$$

The same process is repeated at every time step for the magnetic field at every point of space. This allows the user to model both the electric and magnetic properties of a material with great accuracy.

To better understand Yee's algorithm, the concept of Yee cell (Figure 3.1a) and leapfrog approach must be introduced.

The former is a physical construct associated to a three-dimensional unit cell in which each electric field vector occupies a point in space that is shifted from the origin and that is then surrounded by four magnetic field vectors. This configuration allows the algorithm to relate the E and H field in space for every single point in volume, which is equivalent to

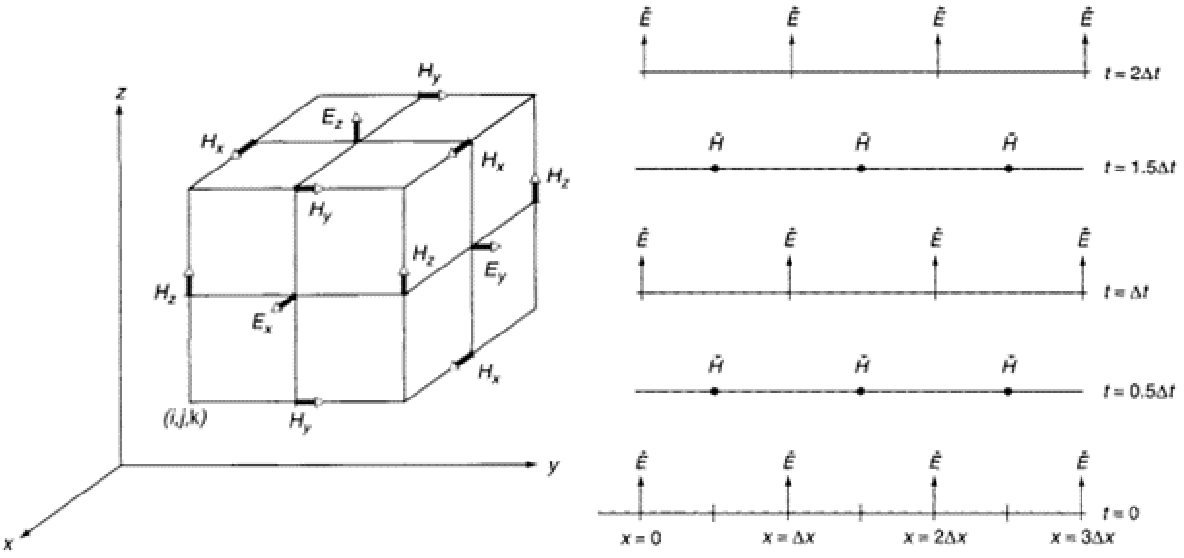

(a) (b)

Figure 3.1: a) Electric and magnetic field vector components for a cubic unit cell in the Yee lattice [62]. b) Schematic representation of the leapfrog phenomenon introduced by Yee in his algorithm [62].

defining both the pointwise differential and the macroscopic integral forms of Maxwell's time-dependent equations.

The latter is a way of computing the electric and magnetic fields in time to account for the mutual dependence of the two quantities. This is achieved by computing and storing all the components of the electric field in space (for each Yee cell) at a certain point in time and then computing the magnetic field using the electric field computed at the step before. The next electric field components are then computed based on the magnetic field data just computed (Figure 3.1b) and so on until convergence to a solution.

To correctly evaluate the propagation of waves in space and time within a limited amount of data, FDTD requires the user to define a simulation domain. This implies that the simulation must be truncated at the end of the space domain, hence these physical constraints must be correctly defined to avoid unphysical reflections at the boundaries.

To do so the user must define a series of grid truncation conditions also known as absorbing boundary conditions. Yee's algorithm does not allow for their direct definition since every field data at a certain time step must be computed for both sides of a point in space, which is not possible with a distinct simulation boundary.

The solution implemented by Lumerical - FDTD comprises of defining a perfectly matched layer or PML as the boundary region to limit the reflected waves to very small numerical values.

Throughout this work, FDTD Lumerical was used to compute the normal-incidence transmission spectra, the corresponding electric field distribution, a variety of parameter sweeps, along with the quality factor and mode volume of the different resonances investigated.

Simulation Environment

All FDTD - Lumerical simulations discussed in this work comprise a 1 mm thick quartz substrate, covered by a 200 nm TiO_2 patterned thin film which is itself surrounded by a TDBC J-aggregate of varying thicknesses.

It is worth noting that during the simulation stage, the position of the TDBC:PVA film with respect to the TiO_2 metasurface has undergone three iterations to account for a realistic result after its deposition. The three iterations considered are shown in Figure 3.2.

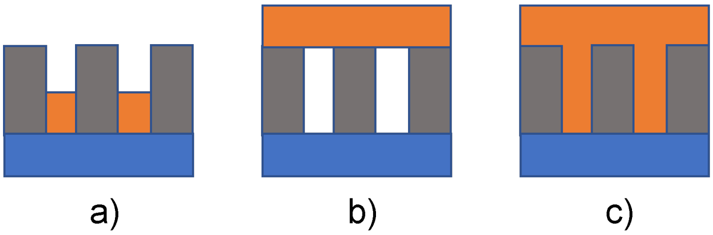

Figure 3.2: Schematic representation of the possible positions the TDBC thin film might assume after spincoating. a) TDBC film between the TiO_2 pillars. b) TDBC film perfectly on top of the metasurface. c) TDBC film completely filling the free volume of the metasurface.

It must be noted that the spincoating solution is water-based, hence its evaporation will not be fast enough for the film to fully form at the top of the TiO_2 metasurface, consequently at the start of spincoating the solution will quickly collapse between the dielectric structures, and it will dry at the bottom of the pillars.

Simulations show that all three configurations lead to similar results for all quantities inspected, with the main discrepancy found in the localization of the mode volume after coupling. Thus, only the results from the one that can be considered as more realistic will be shown in this work.

The real and complex refractive indexes of TiO_2 and TDBC used for the computations are shown in the figures below. The refractive index of the aggregate can vary between different batches due to its dependence on the morphology of the aggregate and quality of the PVA matrix, which can be controlled with changes in temperature, concentration, growth time, and chemical environment. Hence, to make the design process more general the data used for the J-aggregate has been chosen to be the same for all simulations. This choice was made so that the difference in performance is not associated to the quality of the emissive material but only to the different resonances of each configuration (at least during the design and simulation phase).

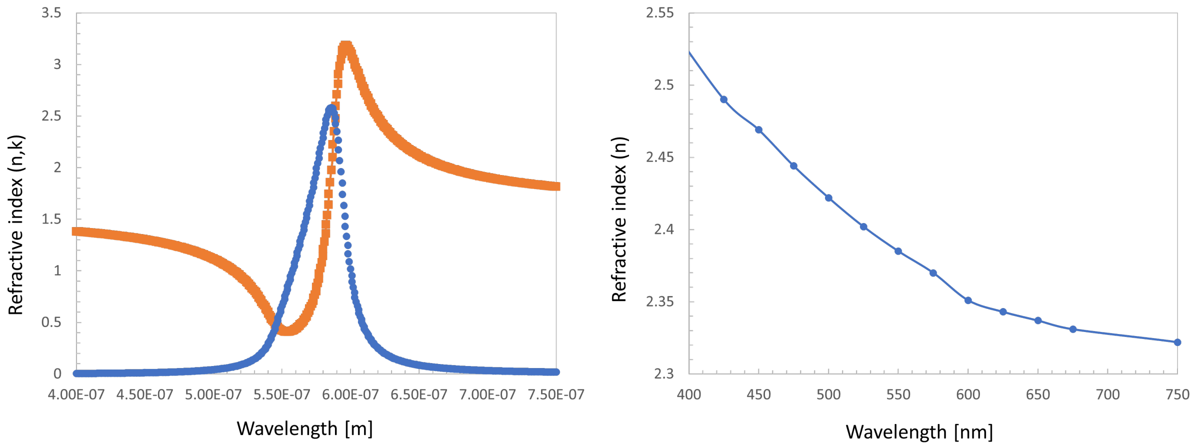

(a) TDBC:PVA (b) TiO_2

Figure 3.3: a) Real (blue) and imaginary (orange) refractive index of the TDBC:PVA thin film. b) Refractive index of the TiO_2 thin film.

Each simulation employed a plane wave source radiating from the bottom of the device with normal incidence and x-polarization. The simulation boundaries along this direction are set as perfectly matched layers to minimize unphysical reflections, while the boundaries along the x and y directions are set as periodic boundaries to extend the unit cell to an infinite array to simulate a metasurface.

The transmittance of the design will be measured for each simulation by placing a frequency domain power monitor above the metasurface perpendicular to the x-y plane in which the unit cell lays, far enough from both the simulation domains and the metasurface itself so as to avoid unphysical reflections with the boundaries and near-field phenomena respectively.

Another frequency domain power monitor will be placed in the x-y plane at a height that crosses the resonators and the molecular aggregate thin film so that the near-field optical response of the metasurface can be studied.

The mesh size utilized varies from a minimum mesh cell of 2.5 to 10 nm depending on the specific geometrical features of the configuration in question. The smaller mesh cells were employed for more complex geometries with sharper features or smaller gaps between structures to avoid unphysical mathematical artifacts during the computation of the electric and magnetic fields.

Of similar importance is also the wavelength resolution of the simulation, which must always be taken into account in order to resolve the various resonances present in the wavelength range span by the source. This is especially relevant when dealing with high Q-factors, and thus narrow linewidths, resonances such as the quasi-BIC that will be shown in the next few chapters. To account for this, the mesh accuracy parameter implemented in FDTD – Lumerical has been varied between values of 2 to 4 according to the Q-factor of the optical resonance.

COMSOL Multiphysics

Comsol Multiphysics works by using a finite element method (FEM) to discretize the geometry of a physical system into small interconnected elements. Each element is described by a set of governing equations that describe the behavior of the system based on the physics being modeled.

It allows the user to define the geometry of the system, specify the material properties of the different components, and set up the governing equations for the various physical phenomena being simulated. It then uses numerical methods to solve the equations and simulate the behavior of the system.

All simulations performed in Comsol Multiphysics employed the Maxwell's equations in a medium characterized by an electric and magnetic permittivity as the governing set of equations in the simulation volume.

The great advantage of Comsol is that it provides multiple tools to fine tune the mesh, allowing the user to increase the precision of the mesh in places where some geometrical features might be particularly critical. In this work, a combination of tetrahedral and triangular mesh elements was employed.

The setup of the unit cell boundaries and the transmittance monitors is analogous to what has been described in the previous chapter.

3.2. Optical Resonances

Under the right conditions, when light interacts with matter, a wide variety of optical resonances can occur. The type of resonance is usually defined according to the electric and magnetic field distribution in space at the resonant wavelength. The same material can undergo resonant behaviour in a variety of ways.

This work will mainly investigate Mie resonances in a dielectric material, also known as morphology dependent resonances, which arise due to photons scattering on objects of size comparable or within a few orders of the incident wavelength inducing displacement currents in the resonators. Under these conditions, the EM field of the incoming photons is redistributed and when the geometry is tuned properly it can lead to high enhancements of the local EM field [61]. Additional simulation-based work will be presented for quasi-bound state in the continuum (Q-BIC) resonances.

The specific pattern of the EM field distribution induced by the excitation can be classified in a variety of resonances. Some common examples include the electric (ED) and magnetic dipole (MD) [74], higher order multipoles, quasi-BICs and the anapole resonances, which can all be identified by their characteristic field distributions. This thesis will analyse the ED, MD, lattice, and quasi-BICs resonances [35, 42] associated to four distinct geometrical configurations.

Every resonance will behave differently when coupled to another material that does not share the same response at the same wavelength. This stems from the fact that the second material will have a different reaction to the incoming radiation and thus will not display the same displacement currents, resulting in a different electric field distribution. The hybrid electric field distribution of the system will be affected by the geometry and permittivity of both materials, hence the characteristic field distribution of the resonance of the dielectric will no longer be as well defined after coupling. It is of the utmost importance to analyse the field distribution of the coupled system since in order to observe Purcell enhancement, the concentration of the electric field within the emissive material must be significant, hence it is not sufficient for the isolated dielectric structure to show a suitable field distribution.

This can be quantified by calculating the modal volume and comparing its value between all configurations. This comparison is still not enough to find the more suitable configuration, in fact it is also important to evaluate the quality factor of the cavity. The best configuration will comprise a sufficiently dense field distribution within the emissive material, a low value of mode volume, and a high quality factor. Attention must also be given towards the feasibility of fabricating these structures with sufficient precision, since all of these observables are affected by geometry.

3.3. Design Process

The principles behind the design process employed in this work were to provide a variety of metasurfaces working at distinct optical resonances and different quality factors so that different coupling regimes between the metasurface and the molecular aggregates could be investigated.

Since the dimensions of the resonators are comparable to the wavelength of the incoming excitation, the optical resonances of the metasurfaces will be strongly dependent on the size and geometrical features of the resonators. Consequently, finding the right set of geometrical parameters associated to each distinct resonance requires precise investigation of how each parameter affects the optical behaviour. This concept will be studied by performing parameter sweeps, large batches of simulations where one geometrical parameter will be varied within a range while all other parameters will be kept constant.

3.3.1. Critical Geometrical Feautures

As already mentioned, working in the visible range with structures of sizes comparable to the excitation wavelength implies a strong correlation between size and optical response. This becomes particularly relevant when the design has to be fabricated, since fabrication tolerances will greatly impact the performance of the metasurface.

It should now become clear how the design process must inevitably account for the constraints imposed by fabrications, hence certain critical geometrical features should be avoided during the design phase. Such constraints include, but are not limited to, too small or sharp geometrical features, tight gaps between areas that will be exposed sequentially during EBL, high aspect ratios with an emphasis on large thicknesses that might complicate etching.

Although features such as tight gaps between resonators can lead to higher quality factors since they can allow better coupling and thus better electromagnetic field localization within the metasurface, the priority throughout this work was given to ease of fabricability. Hence, the patterns designs were kept geometrically simple, and the aforementioned critical features were avoided.

3.3.2. Mie Resonances

Recent research has focused on developing new types of metasurfaces that incorporate Mie resonances to achieve specific functionalities. For example, Mie resonances can be used to achieve selective absorption or transmission of light at certain wavelengths or polarization states, which can be useful for solar energy harvesting or display technologies. Mie resonances can also be used to enhance light-matter interactions in biological or chemical sensing applications, where small changes in refractive index or molecular properties can be detected through changes in the resonance properties. The properties of Mie resonances depend on several factors, including the shape, size, and refractive index of the subwavelength structures. For example, spherical nanoparticles with diameters comparable to the wavelength of incident light can exhibit Mie resonances that are characterized by sharp spectral features and high scattering cross sections. Other shapes, such as cylinders and disks, can also exhibit Mie resonances, but their properties may differ depending on the aspect ratio and orientation of the structures [39, 43].

In this work, the types of Mie resonances were identified by measuring the transmission of each unit cell as a function of geometrical parameters, followed by an analysis of the electric field distribution in the near-field. The latter is a broadly accepted practice employed to univocally identify the character of the resonance, since the displacement currents generated in the near-field of the dielectric resonators can be univocally associated to electric (ED) or magnetic dipole (MD) type responses [31, 39]. Mixed dipoles and multipole resonances can also be found in dielectric resonators, but they were not investigated in this thesis.

Three types of structures will be discussed in the following paragraphs:

- The **bare metasurface**: patterned TiO_2 on a glass substrate.
- The **passive structure**: the bare metasurface surrounded by the molecular aggregate thin film with a constant refractive index (**n**) corresponding to the value of **n** at high wavelengths.
- The **active structure**: the bare metasurface surrounded by the molecular aggregate thin film as an absorbing material with its refractive index depending on the wavelength.

The bare metasurface will be used to identify the resonance and fine tune the geometrical parameters. The passive structure will instead be important to estimate how introducing another high-index material influences the resonance and in particular the near-field electromagnetic field distribution (or mode volume). The active structure is analysed to estimate the extent of coupling between the photonic resonators and the excitonic active material, eventually exposing the presence of polaritons under the right conditions.

The unit cell of the Mie resonances is shown in the left panel of Figure 3.5.

Parameter sweeps

Knowing that the magnetic dipole resonance can be generated when the wavelength of light within the dielectric resonator is comparable to the particle's diameter $D = \lambda/n$ the preliminary dimensions of the resonators can be roughly estimated. Fine tuning of the size and spacing of the resonators within the unit cell will then be required to achieve stronger light-matter interactions and resonances with a stronger electric or magnetic dipole character.

The resonance can be initially identified by a pronounced dip in transmittance, associated to a strong interaction between light and matter, meaning that the electromagnetic field of the incoming radiation has been localized within the patterned dielectric and redistributed throughout space according to the specific geometry and the surrounding refractive index.

The approach adopted was to perform batch simulations in which the radius of the resonator would be varied systematically from 100 nm to 200 nm in steps of 10 nm, while keeping all other geometrical features constant. To keep the period between the unit cells constant the size of the unit cell must be expressed as a function of the radius. Accounting for fabrication tolerances and constraints, the gap between the resonators has been set to 100 nm in the x direction and 75 nm in the y direction, meaning that the size of the unit cell can be written as

$$X = 100 + 2 \cdot Radius$$

and

$$Y = 75 + 2 \cdot Radius$$

with all quantities expressed in nanometers. The thickness of the TiO_2 layer was kept fixed at 200 nm throughout all simulations to allow batch fabrication of multiple geometries per run.

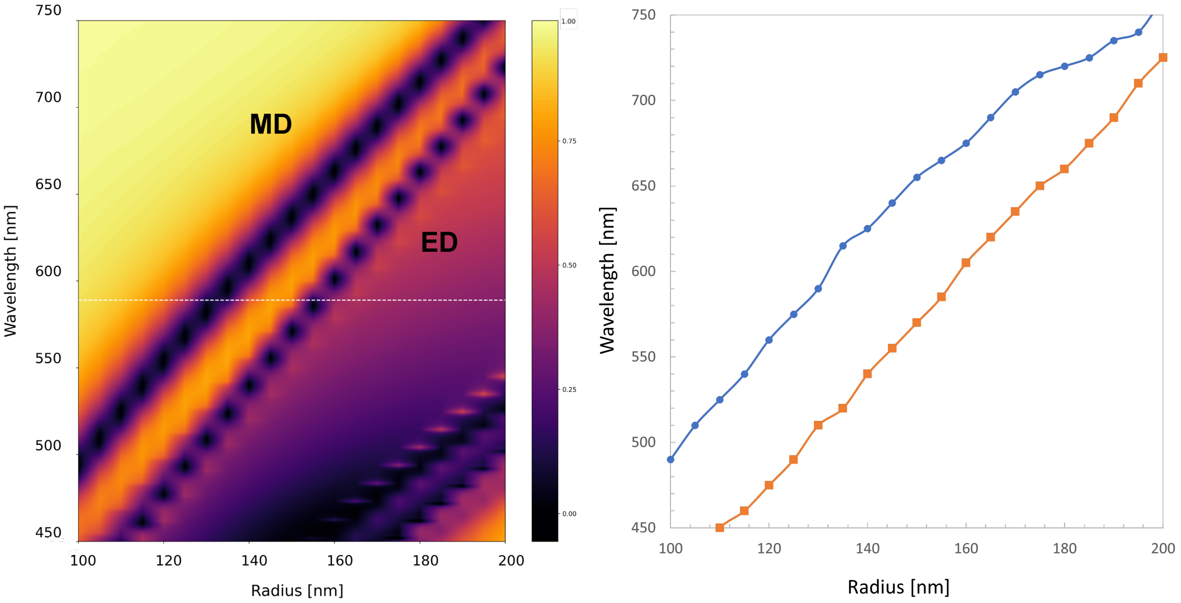

(a) (b)

Figure 3.4: a) Normal-incidence transmission spectra of cylinders of multiple radii in the form of a 2D colormap. b) Magnetic dipole (MD) and electric dipole (ED) resonances forming bands as a function of the radii of the cylindrical resonators.

Figure 3.4a represents the normal-incidence radius-sweep plot, two bands can be distinguished by a dip in transmittance that shifts with the radius. The higher wavelength band can be attributed to the magnetic dipole resonance, while the lower wavelength band can be identified as the electric dipole resonance. An increase in volume of the resonators, shown in this figure by higher radii ($R > 150\ nm$), allows the multipole resonances to arise at lower wavelengths.

Magnetic Dipole Mie Resonance

The magnetic dipole resonance was found for a radius of 130 nm, a thickness of 200 nm, and a unit cell size of 360 nm along the x direction and 335 nm along the y direction. The quality factor of this resonance in its passive mode has been estimated to be $Q \approx 150$.

As shown in 3.5 the magnetic dipole Mie resonance can be univocally identified by the characteristic electric field distribution along a plane parallel to the direction of excitation that crosses the resonator.

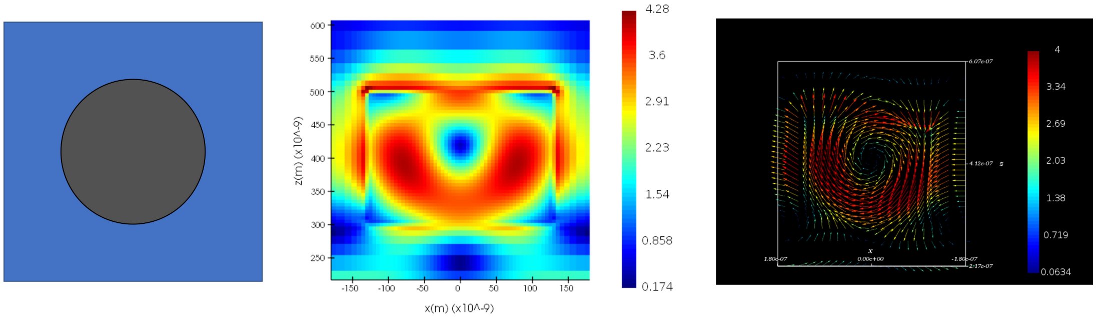

Figure 3.5: a) Top view of the unit cell. b,c) Electric field distribution for the magnetic dipole (MD) Mie resonance. The latter univocally identifies the optical resonance.

Electric Dipole Mie Resonance

The electric dipole resonance was found for a radius of 155 nm, a thickness of 200 nm, and a unit cell size of 410 nm along the x direction and 385 nm along the y direction. The quality factor of this optical mode in its passive form has been calculated to be $Q \approx 79$.

As for the magnetic dipole Mie resonance, the electric dipole response can be identified by its characteristic electric field distribution (3.6).

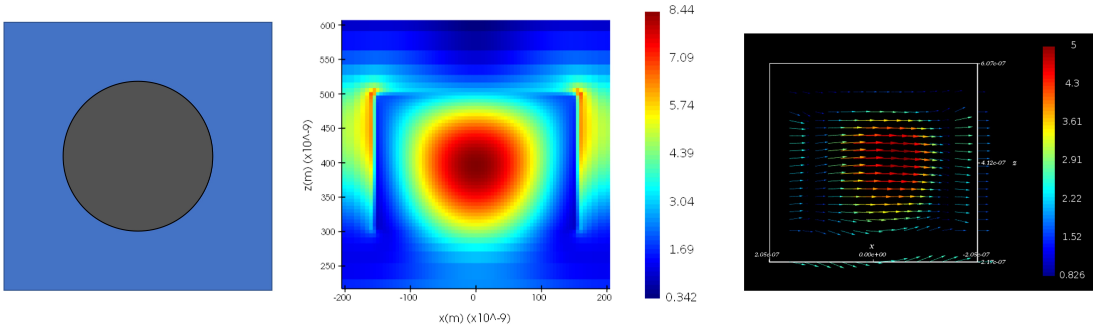

Figure 3.6: a) Top view of the unit cell. b,c) Electric field distribution for the electric dipole (ED) Mie resonance. The latter univocally identifies the optical resonance.

As briefly mentioned before, after finding the optical resonance for the bare metasurface it's important to investigate how the passive and active structure introduced in the previous paragraphs behave.

The presence of an additional layer in close proximity with the metasurface with a refractive index higher than the background (air) will inevitably alter the optical response of the metasurface. Understanding how the response changes with thickness allows us to predict the robustness of the resonance under different sets of conditions that cannot always be precisely controlled during thin-film deposition because the way the TDBC layer will lay on the metasurface depends on a variety of parameters such as the surface tension of all materials in contact, the viscosity of the spincoating solution, and the filling ratio of the resonators.

As shown in the left panel of Figure 3.7, varying the thickness of the passive molecular aggregate between 30 nm and 300 nm considerably shifts the resonance wavelength.

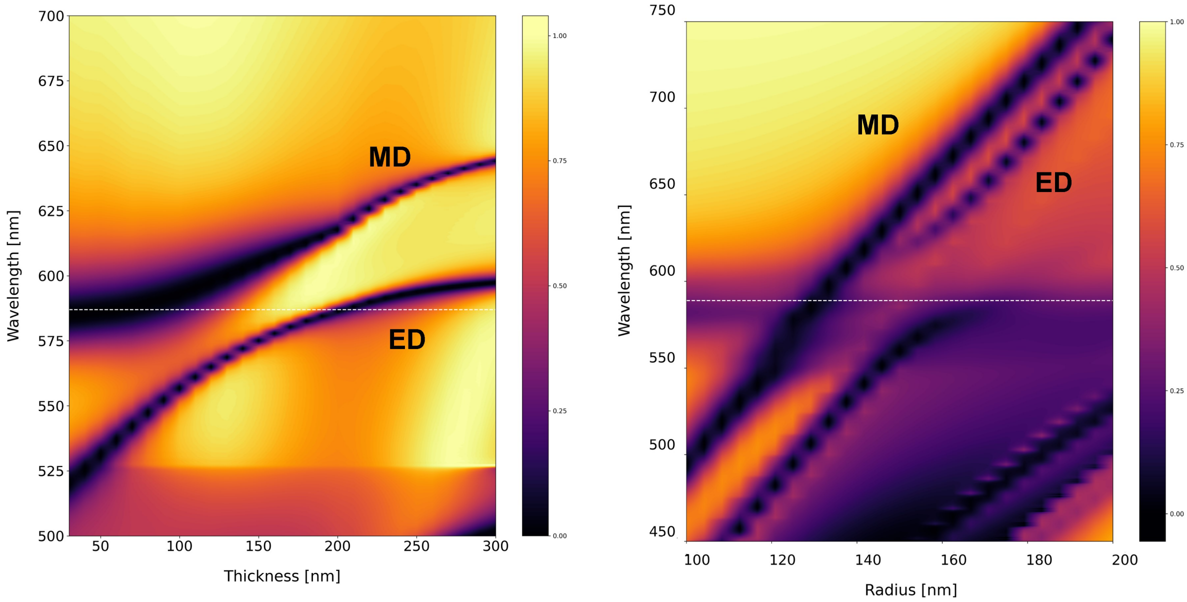

Figure 3.7: 2D colormap representing the MD and ED bands formed by sweeping the thickness of the TDBC molecular aggregate thin film in its passive form (left). 2D colormap representing the MD and ED bands formed by sweeping the radii of the dielectric resonators with the TDBC molecular thin film in its active form (right).

The presence of the passive film does not pose an issue since the electric field distribution of the resonance will not be affected, hence both resonances will retain their magnetic and electric dipoles character (Figures 3.5 and 3.6). Both resonances can thus be deemed robust under the presence of the molecular aggregate thin film.

Additionally, readers might note that the linewidths of the resonances are both reduced meaning that their quality factor increases, this should not be surprising since the presence of a higher refractive index close to the metasurface will increase the localization of the incoming radiation and slow its decay in time.

The same simulation setup was used to investigate the optical response of the two resonances when the molecular aggregate thin film behaves as an active dissipative material, hence with both real and imaginary permittivity expressed as a function of wavelength.

The radius-sweep for this configuration can also be found in the right panel of Figure 3.7, there the two Mie bands can be seen to be perturbed by the presence of the absorbing TDBC thin film.

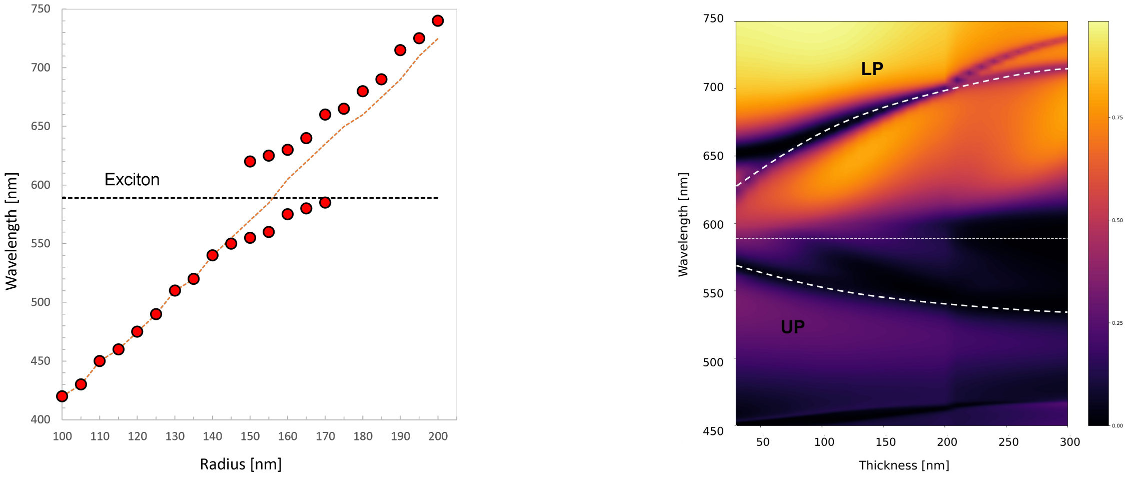

(a) (b)

Figure 3.8: a)Exciton-polariton bands arising due to the coupling between the ED-based metasurface ($R = 155\ nm$) and the absorbing molecular aggregate thin film. b) Exciton-polariton bands arising due to the coupling between the ED-based metasurface and the absorbing molecular aggregate thin film as a function of the thickness of the active dissipative molecular aggreate film.

Both bands split into two distinct peaks each for the radii associated to the on-resonance configurations (MD and ED). These additional peaks not found in the original bare structure can be attributed to the formation of exciton-polaritons in the weak coupling regime. In this system, the off-resonance behaviour of the structure is highlighted by using the radii as a detuning parameter forming the exciton-polariton bands (3.8a) with a splitting of roughly $E_{splitting} \approx 230\ meV$ for the ED mode.

The robustness of the resonance was once again tested by sweeping the thickness of the aggregate thin film while in its dissipative form. As can be seen in Figure 3.8b, the optical response of the device is greatly affected by the presence of films of different thicknesses. The exciton-polariton bands mentioned in the previous paragraphs can still be found for all thicknesses. Although for thicknesses higher than 70 nm the lower polariton band is overshadowed by the MD resonance, the polaritons will still be present for all other instances as can be confirmed by analysing the electric field distribution at the wavelength of interest.

The designs associated to the R=120 nm and R=130 nm resonators were also simulated to test the robustness of the, respectively, MD and ED optical resonances. Figures 3.9 and 3.10 show that the response of the material shifts in wavelength but still retains its respective optical character. Both designs seem to be able to couple strongly enough with the surrounding active molecular aggregate thin film to form both upper (UP) and lower (LP) polaritons, although the UP band is almost completely overshadowed by the higher order resonances present at lower wavelengths.

Further and clearer evidence of the arisal of polaritons in these structures will be given in the next chapter.

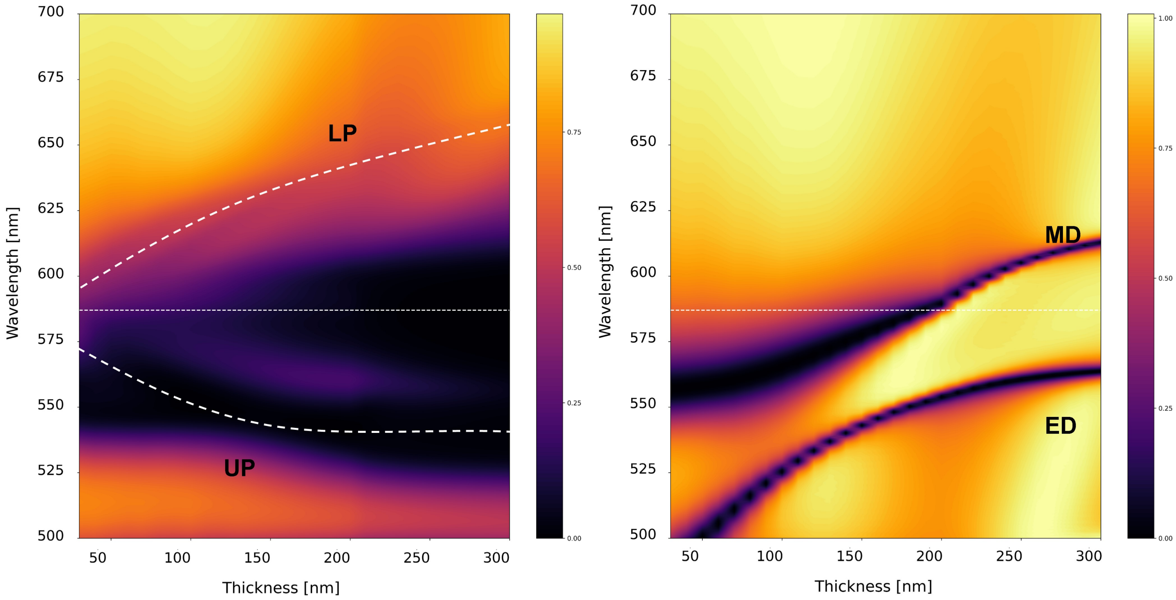

Figure 3.9: 2D colourmap representing the transmittance of the passive (right) and active (left) structures with respect to different thicknesses of the TDBC thin film for the MD resonance configuration (R=120 nm). The upper (UP) and lower polaritons (LP) are identified by the white dashed lines.

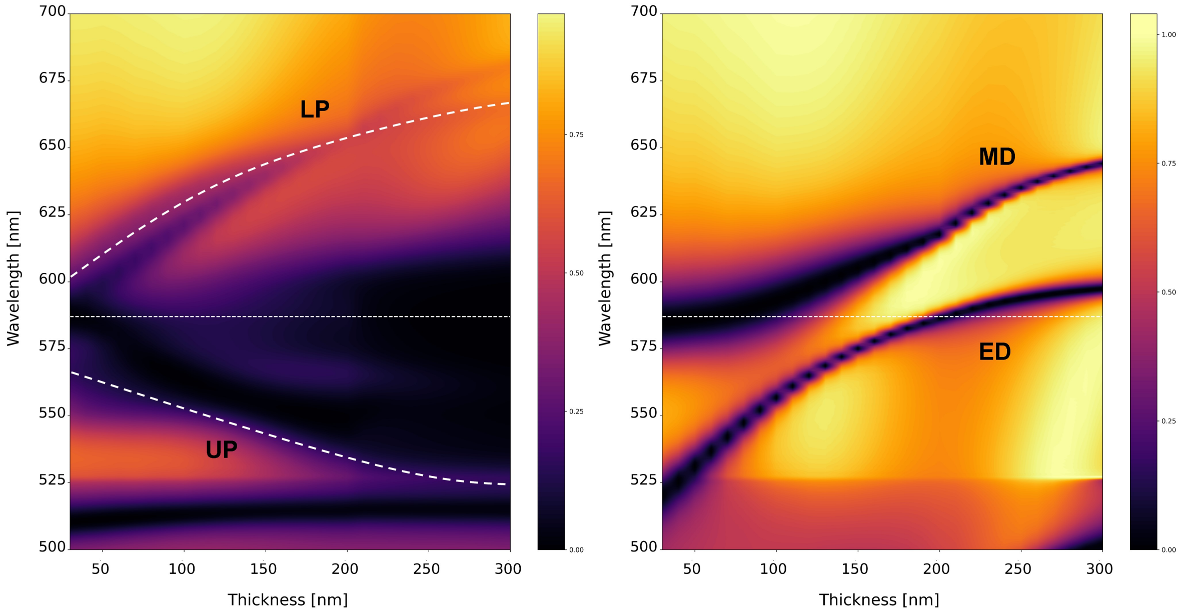

Figure 3.10: 2D colourmap representing the transmittance of the passive (right) and active (left) structures with respect to different thicknesses of the TDBC thin film for the ED resonance configuration (R=130 nm). The upper (UP) and lower polaritons (LP) are identified by the white dashed lines.

Angle-Resolved Transmittance

Angle-resolved transmittance measurements can be used to study the dispersion of exciton-polaritons, as further proof of their manifestation in a hybrid photonic device.

All simulated angle-resolved spectra have been calculated with COMSOL Multiphysics by sweeping the angle of incidence of the incoming optical excitation. The response of the material for multiple angles is captured by a monitor in the far-field measuring the amount of light that is transmitted after crossing the device. The exciton-polariton optical signature can be associated to dips in transmittance after light passes through the metasurface covered by the active molecular aggregate thin film. Angle-resolved transmittance spectra will also display the exciton-polaritons dispersion, allowing us to distinguish them from other optical resonances such as higher-order multipoles and accidental BICs.

Being a strong emitter, the TDBC thin film will inevitably absorb a considerable portion of the incoming excitation, hence the spectrum will always show a broad dip in transmittance around the absorption wavelength (587 nm), meaning that the exciton-polaritons might be overshadowed if the splitting energy is not larger than the absorption linewidth.

This issue has been solved by setting the imaginary refractive index of the aggregate to zero at all wavelengths, so that the TDBC thin film can be considered as an active layer with no dissipative phenomena, thus allowing the formation of exciton-polaritons without the simultaneous formation of a broad dip in transmission associated with absorption from the molecular aggregate.

Mie Resonances in Passive Structures

The thickness of the aggregate thin film has been set to 260 nm to match the experimental results that will be discussed in the next chapter. Figure 3.11 (a) shows the dispersion of the metasurface in its passive form for resonators of $R = 130\ nm$. The MD and ED bands can be seen at respectively 637 nm and 600 nm, meaning that with a 260 nm thick TDBC film the MD resonance cannot be directly utilised with this exact design, while the ED mode will be able to interact with the molecular aggregate film. On the other hand, for $R = 155\ nm$ the ED band (Figure 3.11 (c)) extends to the resonance wavelength of 587 nm for higher angles of incidence.

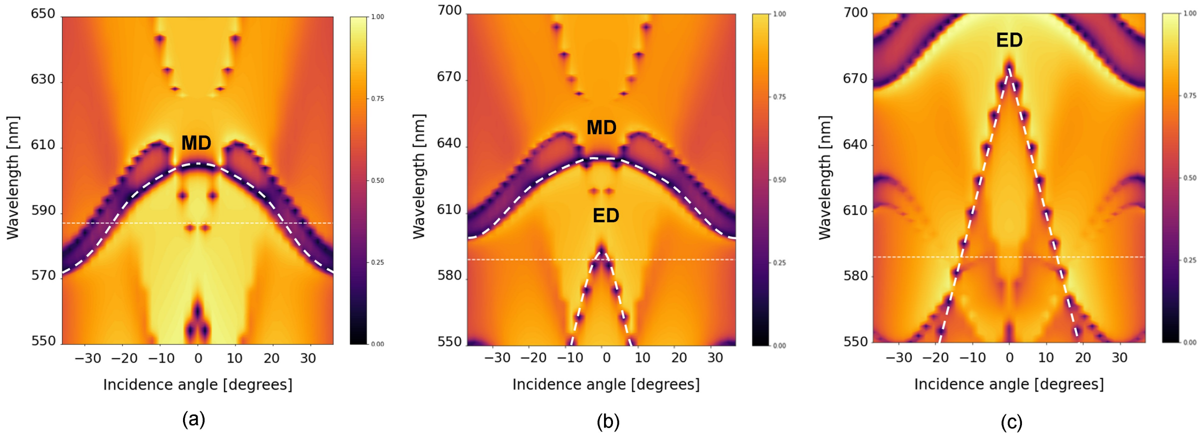

(a)
(b)
(c)

Figure 3.11: Simulated angle-resolved transmission spectra for cylindrical resonators of radii $R = 120\ nm$ (a), $R = 130\ nm$ (b), and $R = 155\ nm$ (c) covered by the TDBC film in its passive form. The angular dispersion of the resonances (white dashed lines) was designed to overlap with the excitonic peak to couple efficiently.

The MD mode can be found as a working resonance at normal incidence for the structure with R=120 nm when the molecular aggregate film is 260 nm thick. This is shown in Figure 3.11 (c), further evidence will also be presented in the next chapter on experimental measurements.

Exciton-polaritons in Active Structures

This section will present evidence of the formation of exciton-polaritons bands in the active structures of the Mie resonances based designs.

Exciton polaritons form when excitons and photons strongly interact in a material. This can occur when spatially confined excitons are subjected to strong optical resonances that localize the electromagnetic field within the same volume. The strong interaction leads to the formation of polaritons, which are hybrid quasiparticles that have both excitonic and photonic characteristics.

The formation of polaritons is typically characterized by a splitting of the exciton resonance into two polariton branches in the reflectivity or photoluminescence spectrum, as well as a modification of the dispersion relation of the polaritons compared to the dispersion of the uncoupled excitons and photons.

The normal-incidence transmission spectra of the R=120 nm (MD Figure 3.12 (a)) and R=130 nm (ED Figure 3.12 (c)) metasurfaces have been utilized to roughly estimate the spectral position of the exciton-polaritons. The exciton-polariton peaks should, in theory, retain some of the photonic character associated to the optical resonance to which the exciton coupled, meaning that the various dips in transmittance found in both spectra can be investigated by analysing their electric field distribution in space since the latter will be shared between the two exciton-polaritons and the photonic resonance.

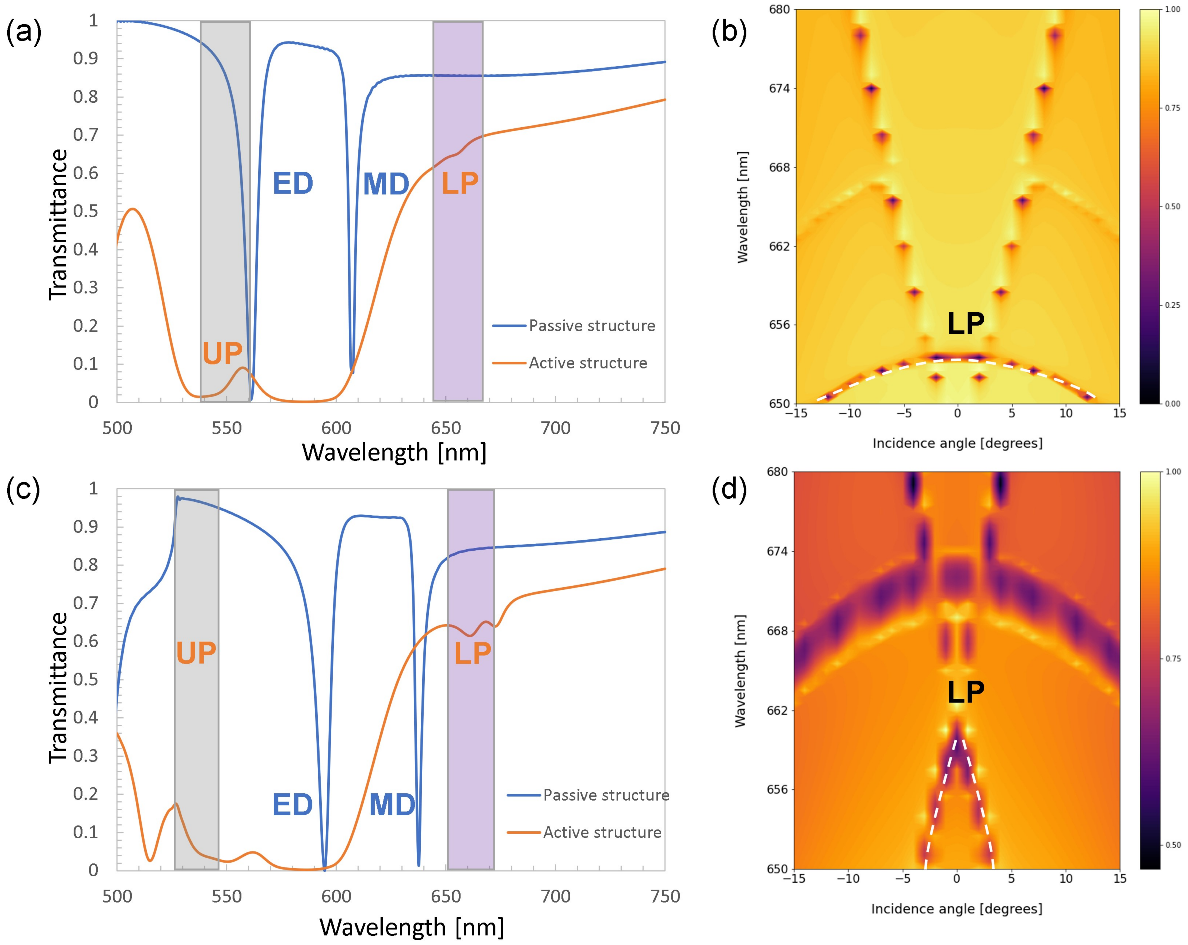

Figure 3.12: a) Simulated normal-incidence transmittance spectrum for cylindrical resonators of $R = 120\ nm$ in its passive (blue) and active (orange) form. b) Simulated angle-resolved transmittance spectrum highlighting the lower polariton band for the MD-based resonance ($R = 120\ nm$). c) Simulated normal-incidence transmittance spectrum for a cylindrical resonator of $R = 130\ nm$ in its passive (blue) and active (orange) form. d) Simulated angle-resolved transmittance spectrum highlighting the lower polariton band for the ED-based resonance ($R = 130\ nm$).

As highlighted in Figure 3.12 (a), both the lower (LP) and upper (UP) polaritons can be identified for the MD-based device (R=120 nm).

In order to confirm their presence the angle-resolved transmission spectrum for the active non-dissipative structure has been simulated (Figure 3.12 (b)) at values of wavelengths surrounding the resonance wavelength of the polaritons as identified in Figure 3.12 (a). The energy splitting of this design can be evaluated as $E_{splitting} \approx 318\ meV$.

The same process of analysis has been repeated for the ED-based device (R=130 nm). Figure 3.12 (c) highlights the spectral position of the polaritons, while 3.12 (d) shows the angular dispersion of the lower polariton. For this design, the energy splitting of the exciton-polaritons is $E_{splitting} \approx 400\ meV$. Both estimates of the energy splitting should be taken as rough estimates due to the fact that in both cases the upper polariton is not a well-defined peak and its electric field distribution is affected by the nearby multipole resonances.

3.3.3. Quasi-Bound States in the Continuum

A bound state in the continuum (BIC) is a mathematical concept arising from the interference between a continuum of propagating modes and a localized resonant mode that results in a mode bound to the structure with a finite lifetime. This occurs because the localised mode has no radiative pathway to dissipate itself, hence it will remain confined within the continuum without any possibility to radiate [28].

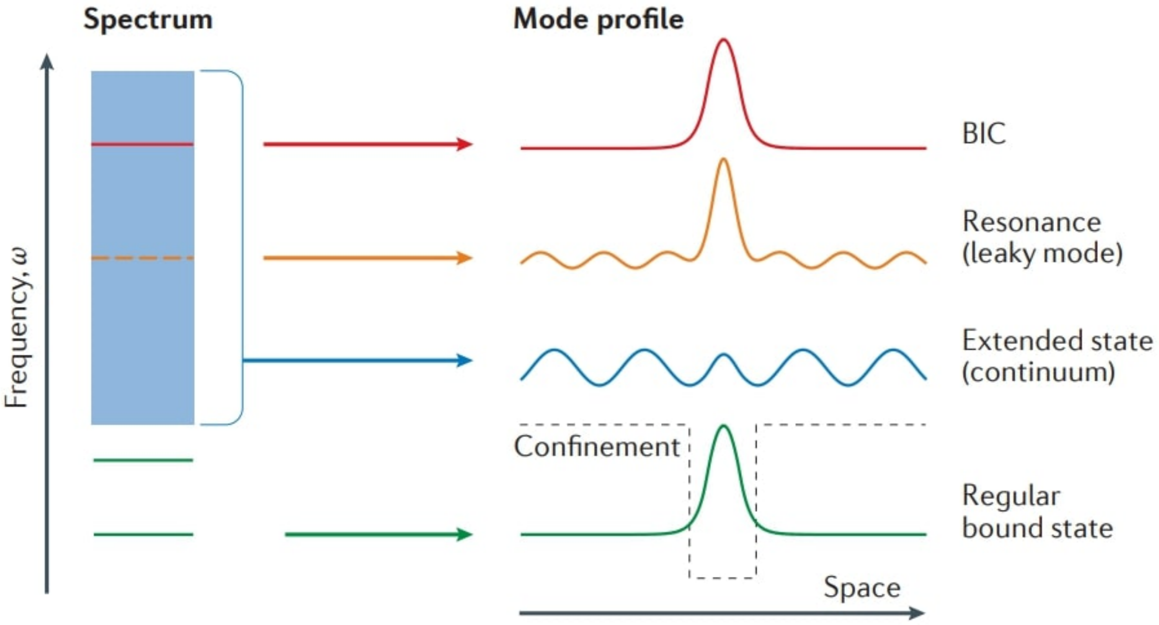

Figure 3.13: Schematic representation of the formation of a bound state in the continuum [28].

Consequently, BICs are dark modes with an infinite quality factor and vanishing linewidth, hence they cannot be directly utilised to enhance light-matter interactions.

Experimentally, bound states in the continuum can be exploited by introducing a perturbation into the system and creating a quasi-bound state in the continuum (Q-BIC). These perturbations include, but are not limited to, finite sample size, unit cell asymmetries, radiative and non-radiative losses.

A signature feature of Q-BICs is that they can exhibit high quality factors that approach infinity for values of the asymmetry parameters close to zero. The radiative Q-factor (Q_{rad}) dependence on the asymmetry parameter has been shown to follow the law: [35, 42, 70, 73]

$$Q_{\text{rad}}(\theta) = Q_0[\alpha(\theta)]^{-2}.$$

A wide variety of unit cell designs have been proposed to fabricate high Q metasurfaces [42, 55]. This work will focus on Q-BICs induced by breaking the in-plane inversion symmetry of the unit cell [35].

Electric Dipole Quasi-Bound State in the Continuum

The Q-BIC resonance analysed in this work has been found for the unit cell shown in Figure 3.14, in which the asymmetry parameter introduced is associated to the angle the ellipsoidal resonators have with respect to the z axis perpendicular to the plane the metasurface lies in. The resonance arises at the resonance wavelength for $R_x = 50\ nm$, $R_y = 135\ nm$, and a unit cell spanning 440 nm in the x direction and 660 nm in the y direction.

The asymmetry parameter has been limited to $\theta = 60 - 70°$to achieve high Q-factors while still accounting for fabrication tolerances. In fact, although asymmetry angles closer to $90°$ would yield much higher quality factors, the disruption of the unit cell symmetry has to be considered within the context of nanofabrication. The aspect ratio (in this case defined as R_y/R_x) of the ellipsoidal resonators would not break the unit cell symmetry when fabrication tolerances are accounted for.

This configuration has been identified as an electric dipole quasi-bound state in the continuum by inspecting the electric field distribution in the plane perpendicular to the incoming radiation (x-y plane). The EM field distribution found in Figure 3.14 closely matches the data found in literature [35].

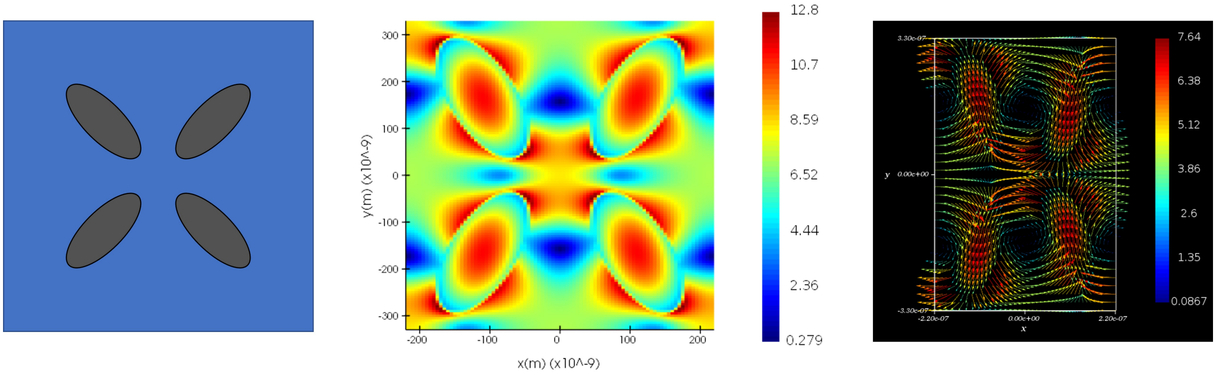

Figure 3.14: a) Top view of the unit cell. b,c) Electric field distribution for the ED quasi-bound state in the continuum resonance. The latter univocally identifies the optical resonance.

Geometrical Sweeps

The quality factor of the Q-BIC will depend on the value of the parameter that breaks the in-plane symmetry. This dependence is shown in Figure 3.15 for the configuration in question. The highest quality factor was calculated for $\theta = 85°$ with a value of 9589. Higher values of Q-factors are found for higher asymmetry angles, but as mentioned in the previous paragraphs this work focused on lower asymmetry angles to aid fabricability.

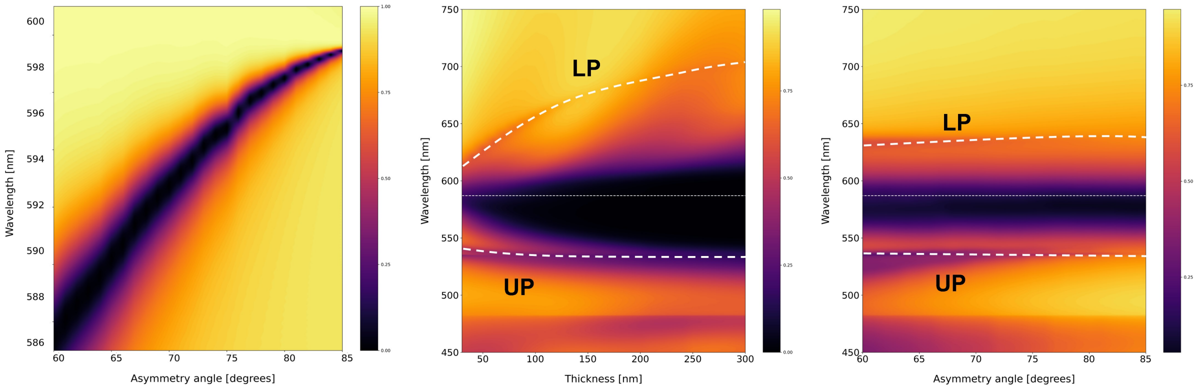

(a) (b) (c)

Figure 3.15: a) 2D colourmap representing the relation between the parameter of asymmetry (θ) and the resonance linewidth of the passive structure of the electric dipole quasi-bound state in the continuum optical resonance, showing the linewidth becoming infinitely small towards the condition for a perfect BIC (θ=90). b-c) 2D colourmap of the optical response of the ED Q-BIC resonance to changes in thickness (b) of the TDBC film and the asymmetry parameter (c) for the active structure.

Analogously to what has been done for the two Mie resonance-based designs, the robustness of the resonance has been tested with respect to different thicknesses of the TDBC thin film (Figure 3.15 (b)).

The dependence of the exciton-polariton bands dispersion from the angle of asymmetry of the unit cell can be found in the last panel of Figure 3.15. As shown by the low curvature of the bands, both exciton-polariton bands seem to be weakly dependent on the asymmetry parameter. This further supports the decision to work at higher asymmetry parameters and thus easier to fabricate structures, since a higher Q-factor does not seem to strongly affect the splitting of the polaritons and thus the coupling regime.

Angle-Resolved Transmittance

The angle-resolved transmission spectra are once again used to investigate the dispersion of the exciton-polaritons.

The normal-incidence transmittance spectrum (Figure 3.16) was used to roughly estimate the wavelength of the exciton-polaritons peaks before computing the full angular dispersion of this design.

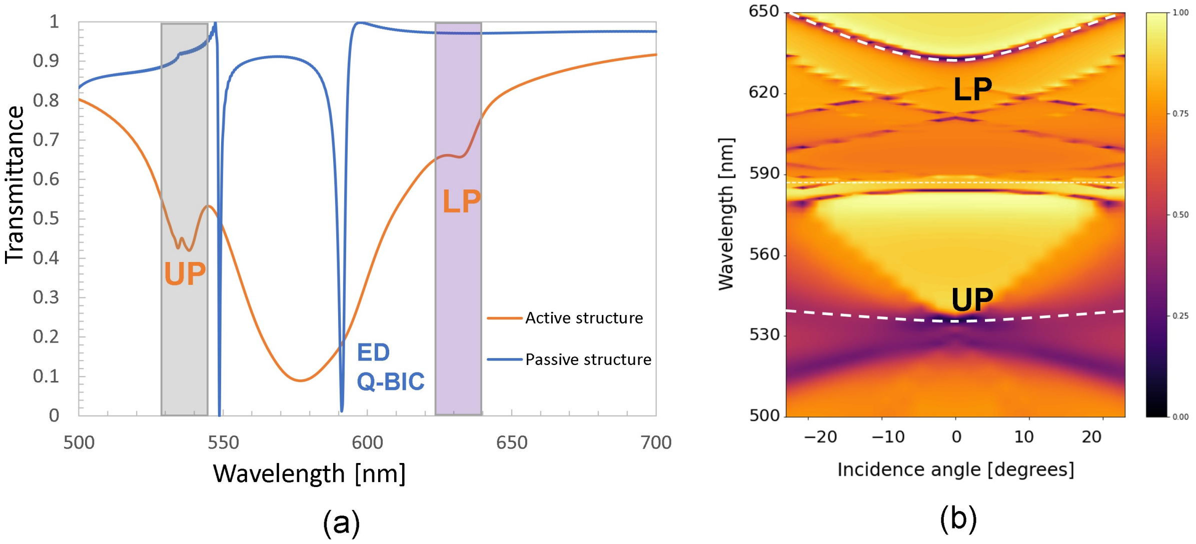

Figure 3.16: a) Simulated normal-incidence transmittance spectrum for the ED Q-BIC structure in its passive (blue) and active (orange) form. b) Simulated angle-resolved transmittance spectrum highlighting the lower polariton band for the ED Q-BIC structure formed due to strong coupling between the metasurface and the active non-dissipative molecular aggregate thin film.

Figure 3.17 shows the dispersion of the passive structure, with the electric dipole quasi-bound state in the continuum resonance matching the absorption wavelength of the molecular aggregate thin film (highlighted by the dashed white line). The band around 600 nm can be attributed to a perfect bound state in the continuum becoming a quasi-BIC due to the angle of incidence disrupting the in-plane symmetry of the unit cell. The band seen at lower wavelengths can instead be attributed to a higher order resonance.

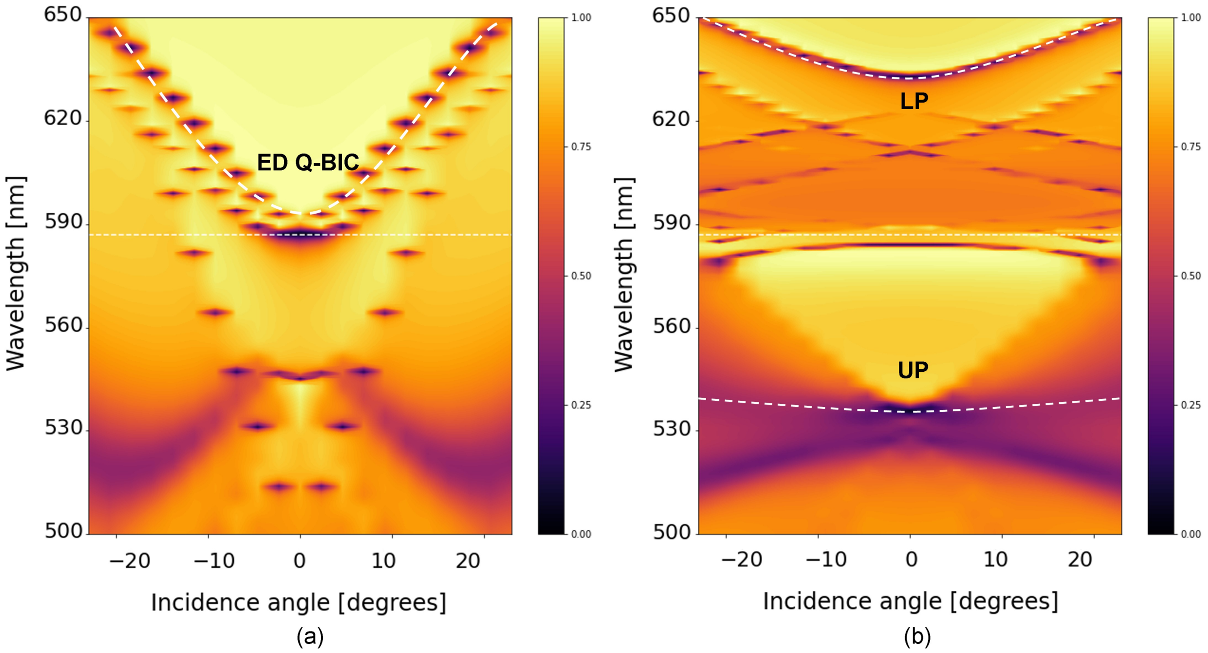

Figure 3.17: a) Simulated angle-resolved spectrum showing the angular dispersion of the ED Q-BIC resonance for the passive structure. b) Simulated angle-resolved transmittance spectrum highlighting the upper and lower polariton bands for the ED Q-BIC structure formed due to strong coupling between the metasurface and the active non-dissipative molecular aggregate thin film. The emergence of exciton-polaritons occurs because of the strong coupling between the active film and the metasurface.

It should be noted that the discretization of the bands is due to the simulation not having enough wavelength resolution to fully resolve the narrow linewidth of the high quality factor resonance.

The response of the metasurface when covered by the active non-dissipative TDBC film is shown in Figure 3.17. The lower (LP) and upper polariton (UP) bands are highlighted by the white dashed lines, the energy splitting in this configuration reaches a value of $E_{splitting} \approx 370\ meV$.

3.3.4. Quality Factor

The quality factor of a resonance can be broadly defined as the ratio between the energy stored and the energy loss per cycle of oscillation. It is a measure of how long light can be confined within a cavity before it escapes or completely dissipates because of losses. The Q-factor of a cavity depends on various factors such as the cavity material, geometry, and the presence of any lossy elements [65].

The values of quality factors found throughout this manuscript have been computed in Lumerical - FDTD [2]. Although it's possible to compute the quality factor of an optical cavity by measuring the full width at half maximum (FWHM), it is not the most reliable method since the FWHM for high quality factor resonances would not be correctly defined if the resonance linewidth and lifetime is limited by the time of simulation (i.e. the simulation does not converge).

Hence, the more general definition of the quality factor will be adopted

$$Q = \frac{-2\pi f_r log_{10}(e)}{2m}$$

where $\mathrm{f_r}$ is the resonant frequency of the optical mode and m is the slope of the electric field decay.

Knowing that the time domain signal of the electric field can be defined as

$$E(t) = e^{\mathrm{-r}(\alpha\ \mathrm{-\ iw_r})}u(t)$$

with α being the decay constant, the slope (m) of the decay can be related to the quality factor (Q) through the linear envelope function

$$log_{10}(|E(t)|) = \frac{-w_r t}{2Q} log_{10}(e) = mt$$

which leads to

$$Q = \frac{-w_r log_{10}(e)}{2m}.$$

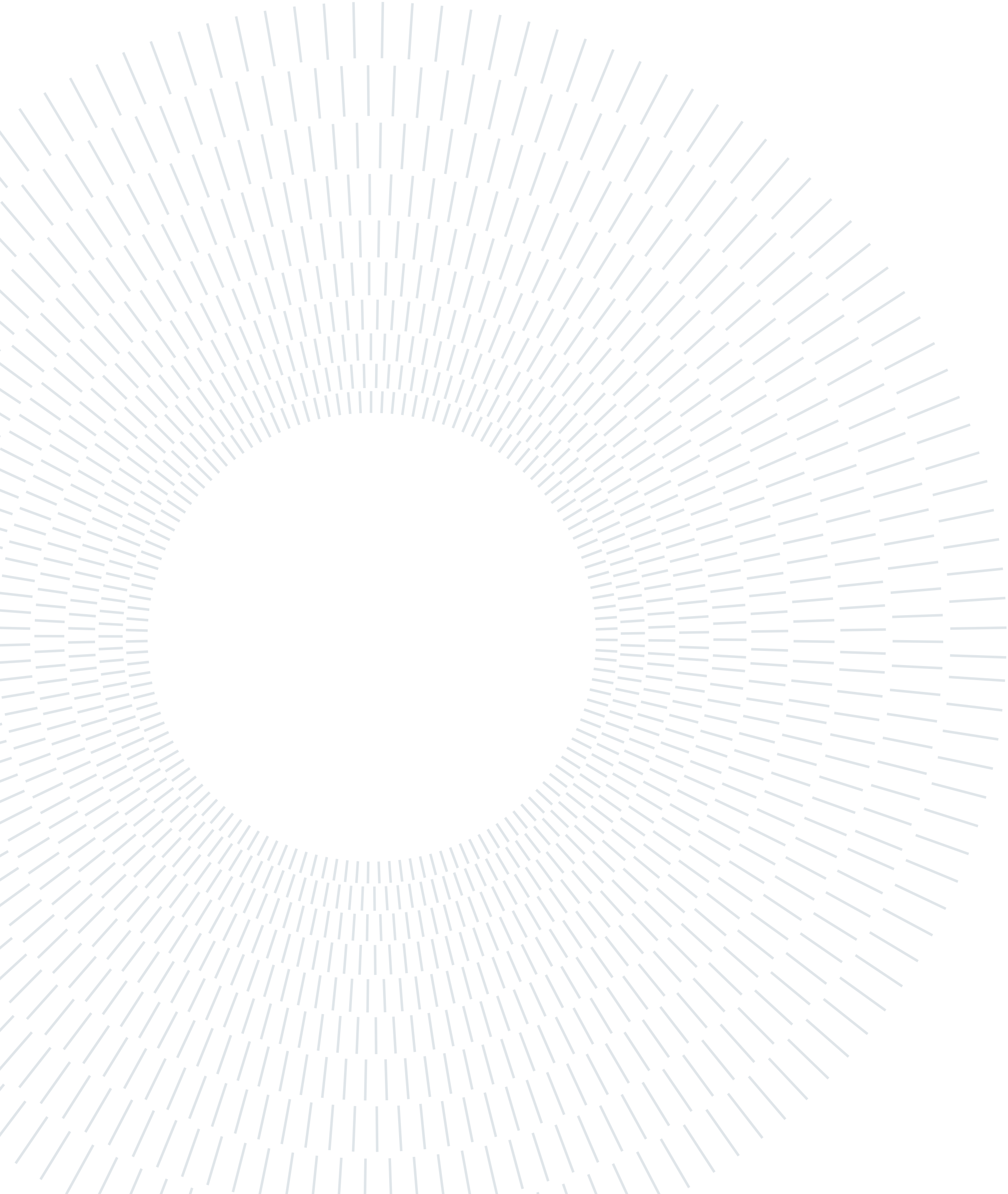

4 | Materials and Methods

4.1. Materials

The devices presented in this thesis are composed of a multilayer structure, consisting of three distinct materials stacked on top of each other. The bottom layer is a 1 mm thick quartz substrate. The middle layer is a 200 nm thick TiO_2 metasurface. The top layer is a thin film of TDBC J-aggregate (Figure 4.1 (a)).

The choice of these specific materials was based on their optical properties and mutual compatibility. The quartz substrate was selected for its high transparency in the visible range and mechanical stability. The TiO_2 metasurface was chosen for its ability to support a variety of optical resonances, as well as its high real refractive index and negligeable dissipative losses in the visible spectrum. The TDBC J-aggregate was selected for its strong absorption and emissivity in the visible spectrum, along with the ability to manifest superradiance.

The fabrication process involved deposition techniques such as sputtering and spin-coating, as well as nanofabrication techniques such as electron beam lithography and dry etching.

4.1.1. Sputtering of TiO_2 thin films

The first step of fabrication of the metasurfaces is the deposition of 200 nm TiO_2 thin films on top of a 1 mm thick quartz substrate. The latter is cleaned beforehand by sonication in water, acetone, and isopropanol for 5 minutes per step.

The TiO_2 thin film is deposited by sputtering at a vacuum pressure of roughly $10^{-7} mbar$ in a Ar atmosphere and a power of 150 W with deposition rate ranging from 1.75 to 2.35 $\frac{nm}{min}$ depending on the physical position of the substrates with respect to the 99.99% titanium dioxide target.

The uniformity of the deposited films was evaluated by measuring the reflection at four distinct points per sample with a microspectrophotometer and then comparing the spectra with those obtained by FDTD Lumerical simulations. Knowledge of the refractive index of TiO_2 made it so the reflection peaks of the spectra could only shift due to changes in thickness. The experimental spectra could thus be fitted by simulated data of different thicknesses to evaluate the real thickness of the deposited layer.

4.1.2. Synthesis and Deposition of TDBC Thin Films

The molecular aggregate 5,6-Dichloro-2-[[5,6-dichloro-1-ethyl-3-(4-sulfobutyl)-benzimidazol-2-ylidene]-propenyl]-1-ethyl-3-(4-sulfobutyl)-benzimidazolium hydroxide, inner salt, sodium salt (TDBC Figure 4.1 (b)) is a water-soluble cyanine dye that undergoes self-assembly in water to form highly ordered structures known as J-aggregates (Figure 4.1 (c) and (d)).

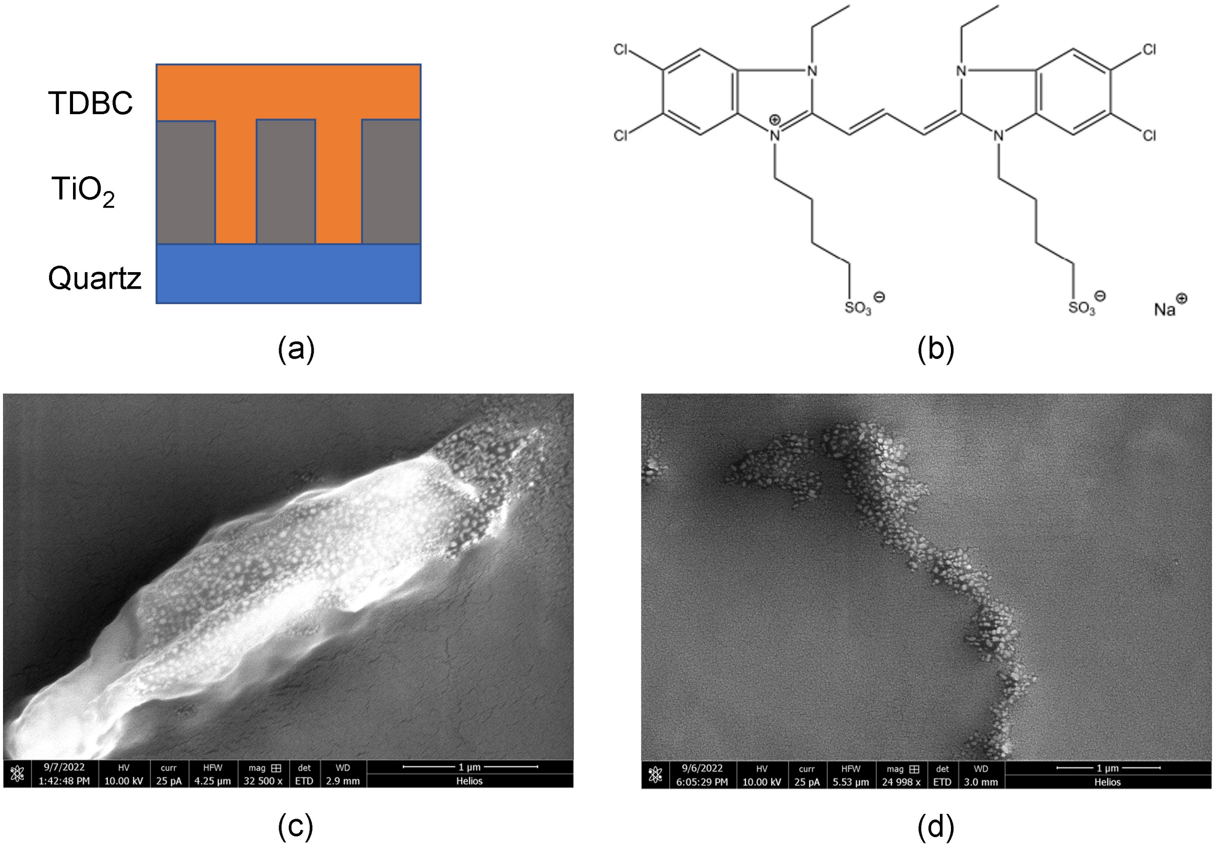
TDBC
TiO2
Quartz
(a)
Cl
Cl
N
N
N
N
Cl
Cl
SO3
SO3
Na
(b)
9/7/2022 1:42:48 PM
HV 10.00 kV
curr 25 pA
HFW 4.25 µm
mag 32 500 x
det ETD
WD 2.9 mm
1 µm
Helios
(c)
9/6/2022 6:05:29 PM
HV 10.00 kV
curr 25 pA
HFW 5.53 µm
mag 24 998 x
det ETD
WD 3.0 mm
1 µm
Helios
(d)

Figure 4.1: a) Side view of the schematic representation of the fully integrated device. b) Structural formula of 5,6-Dichloro-2-[[5,6-dichloro-1-ethyl-3-(4-sulfobutyl)-benzimidazol-2-ylidene]-propenyl]-1-ethyl-3-(4-sulfobutyl)-benzimidazolium hydroxide, inner salt, sodium salt in its monomeric form. c) and d) SEM images of fully formed TBDC J-aggregates in two distinct supramolecular structures covered by a thin layer of gold.

Cyanine dyes share a common molecular structure consisting of a highly conjugated polymethine chain linking two nitrogen atoms. The presence of side branches and other sterically significant structures creates a wide range of possible cyanine dyes with distinct morphologies and optical properties.

The self-assembly process occurs due to the high conjugation of the single monomeric unit that allows the formation of highly ordered structures due to the balance between the π-π interactions of highly polarizable groups and the electrostatic interactions of opposite charges. More specifically, TDBC forms J-aggregates in water due to the hydrophobic effect: water acts as a poor solvent for the monomeric units, hence mutual aggregation between different units is favoured with respect to solvation [57].

Being driven mainly by dispersion forces between the nearest neighbor molecules created by high polarizability of π-electrons of the polymethine chain, the process of J-aggregate formation in water depends on the dye structure, its concentration and also on the solvent conditions, such as the concentration of ions and pH [10]. Solvents are capable of shielding the charges that drive aggregation, hence the solvent determines the extent of the solvophobic interactions. Given a certain solvent and a set of physical conditions, the main driving force behind aggregation is the concentration of monomeric units in solution, following a generally linear trend with an increase in concentration.

Differently from the vast majority of other cyanine dyes, TDBC is only stable in its J-aggregate form (head-to-tail conformation), hence no H-aggregates morphologies (face-to-face conformation) will form in water. This is a great advantage for a variety of reasons, the most important of which is that H-aggregates could be a parasitic resonance with considerably lower electronic coupling and subradiant nature [60, 69].

4.1.2.1. Synthesis of TDBC

The process of self-assembly is a spontaneous aggregation mechanism that is strongly dependent on the chemical environment and on the physical conditions. It is therefore important to establish the optimal aggregation conditions to ensure that the final product has the right optical properties and morphology.

In this work, the two main parameters that have been tuned are the concentration and the growth time. It should be noted that these parameters are not known to alter the aggregation pathway directly, but they will still affect the final aggregate.

Growth Time

Room temperature aggregation of TDBC in deionized water occurs almost instantly once the monomeric units are introduced in solution, as can be seen by the sudden change in colour to pink.

This set of experiments was performed in order to determine the value of time required to reach the saturation point at which the balance between solvation and the solvophobic effect is still in favour of the latter, and thus of aggregation. This means that at all growth times below the saturation value, the growth of the aggregate will be favoured with respect to its dissolution in water and thus into its less aggregated form. Additionally, special care has to be taken to avoid aggregate degradation which can be easily induced by exposure to light, hence the growth solution must be covered from light at all times to ensure long-term storability.

Assuming that the self-assembly kinetics are concentration dependent, these experiments must be conducted at the same starting concentration to determine the saturation growth time univocally. The results that will be shown below refer to a starting concentration of $2.5\frac{mg}{mL}$ of TDBC in deionized water. The steady-state emission of the solution was then measured over varying periods of time.

At first, the solution was measured over the span of 1 hour, by taking measurements every 5 minutes (Figure 4.2a).

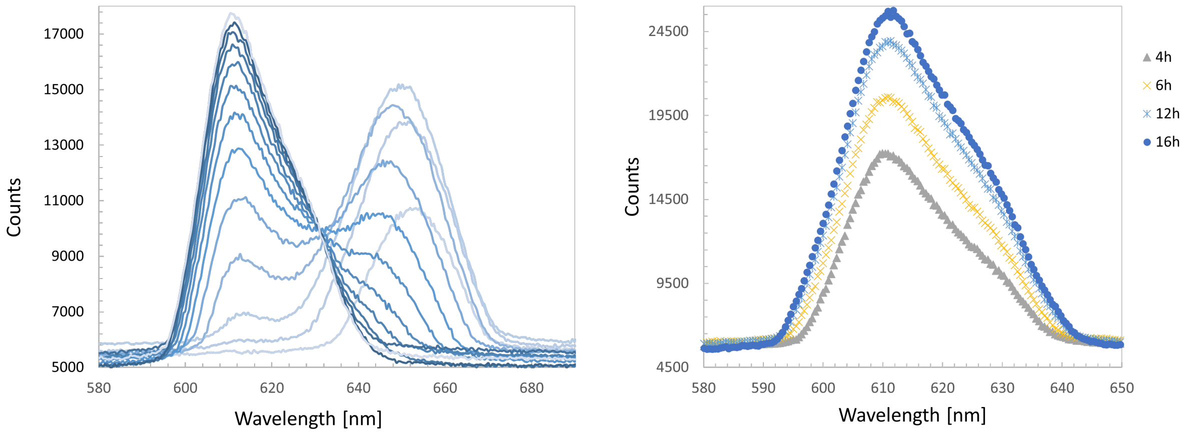

(a) (b)

Figure 4.2: Photoluminescence spectrum during the first hour (a) and 16 hours (b) of in-solution growth of the TDBC J-aggregate. The photoluminescence peak if the J-aggregate is shown to be growing in intensity with time, meaning that the monomers have not yet fully converted into J-aggregates.

The plot clearly shows that 1 hour is not sufficient for the monomeric units to be fully converted into grown aggregates.

Consequently, the growth time of an identical solution was monitored over wider periods of time up to 16 hours (Figure 4.2b).

Other measurements were also performed for longer times, but the increase in intensity for the peak associated to the grown aggregate was deemed negligible, hence growth times around the 16 hours mark can be taken as a good starting point to optimize other growth parameters. Non-negligible degradation of the aggregate was observed if the solution was left exposed to light over multiple days.

Monomer Concentration

In order to find the optimal concentration of TDBC in water, a series of solutions of increasing concentrations have been left to aggregate for 24 hours. The solutions were then mixed with a PVA matrix and spincoated into thin films so that the solid-state steady-state photoluminescence could be measured (Figure 4.3a). The point of these measurements is to find the point of diminishing returns for the starting concentration.

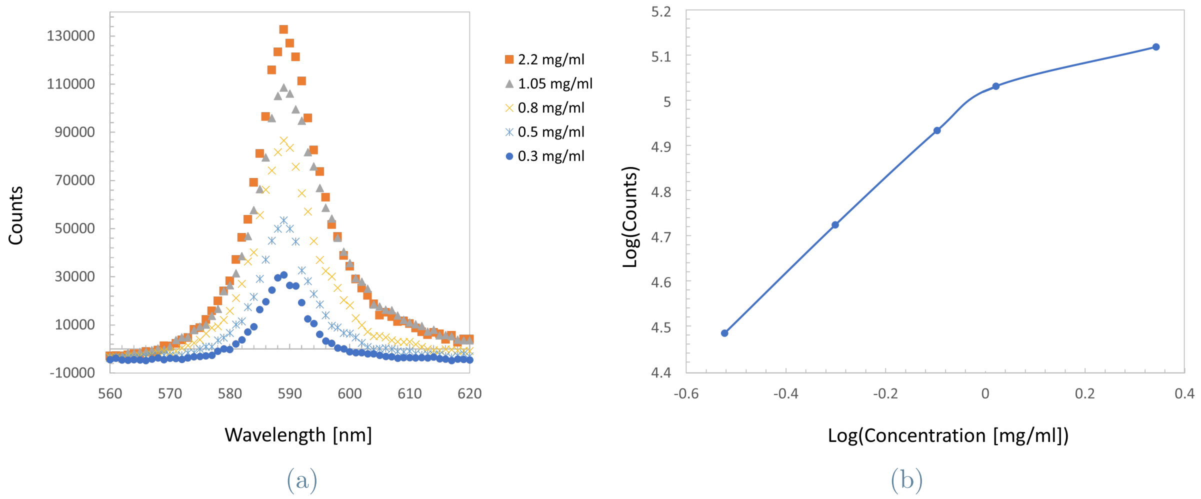

(a) (b)

Figure 4.3: a) Photoluminescence spectrum of grown TDBC J-aggregate thin films of different starting monomer concentrations. b) Double logarithmic plot of grown TDBC J-aggregate thin films of different starting monomer concentrations showing the peak emittance reaching saturation with increasing monomer concentrations.

As can be seen in the double logarithmic plot in Figure 4.3b, the peak photoluminescence of the J-aggregate band follows the typical concentration related trend associated to J-aggregates [37] up to a concentration of roughly $2.2\frac{mg}{mL}$ at which point the trend seems to slow down suggesting some form of saturation. Slightly higher concentrations were also tested, but the increase in photoluminescence was negligeable and the solutions showed physical deposits of aggregates, meaning that the saturation concentration for solubility in water had already been reached in the meantime.

Optimized Synthesis of TDBC J-aggregates in a PVA matrix

The cyanine dye TDBC (5,6-Dichloro-2-[[5,6-dichloro-1-ethyl-3-(4-sulfobutyl)-benzimidazol-2-ylidene]-propenyl]-1-ethyl-3-(4-sulfobutyl)-benzimidazolium hydroxide, inner salt, sodium salt) was acquired from Biosynth Carbosynth in its monomeric form (CAS: 18462-64-1). TDBC was dissolved in DI water in a concentration of $2.5\frac{mg}{mL}$ and left to aggregate for 24 hours at room temperature, covered from light exposure. A solution of $64\frac{mg}{mL}$ of Poly(vinyl alcohol) purchased from Sigma Aldrich (CAS: 9002-89-5, Mw 85,000-124,000, 99+% hydrolysed) was prepared by further polymerizing PVA in DI water for 4 hours at 90°C under constant stirring.

The grown TDBC molecular aggregate and the PVA solution were then mixed in a 1:1 ratio. The addition of PVA is required to ensure better filmability by supplying a stable matrix to the aggregate.

1 mm thick quartz substrates were cleaned by ultra-sonication in DI water, acetone, and isopropanol for 10 minutes each. The substrates were then thoroughly dried with N_2 so as not to dissolve the water-soluble molecular aggregates during the spincoating step.

A volume of 100 µL of the mixed TDBC-PVA solution was then spincoated at 2000 rpm for 60 seconds on top of the cleaned quartz substrates. The film was further dried at 4000 rpm for 30 seconds.

4.2. Nanofabrication of Dielectric Metasurfaces

4.2.1. Electron Beam Lithography of TiO_2 [53]

Working with metasurfaces in the visible spectrum implies the need to fabricate large arrays of resonators with feature sizes in the order of tens up to hundreds of nanometers. Being restricted to such small dimensions makes it so that fabrication tolerances are particularly unforgiving, especially if the metasurface has to have an high quality factor and transmittance.

Within this context the most suitable fabrication technique to produce such restrictive geometrical features is electron beam lithography (EBL).

Electron beam lithography is able to create precise nanopatterns by using a focused electron beam to alter the solubility of a resist across a surface. After irradiation, the change in solubility of the resist (often caused by electron beam induced chain scission) causes the latter to be selectively removed by a developer.

Physical Constraints and Defects

The ultrahigh resolution of this technique is a direct consequence of using high energy electrons, currently sub-10 nm feature sizes have been reported by both resist manufacturers and researchers [15, 45]. When electrons impact the resist they scatter, causing an inevitable broadening of the beam, thus the practical resolution that can be achieved is lower than the starting beam spot size. This phenomenon, associated to backscattered and secondary lateral electrons, is known as the proximity effect and in order to achieve better resolutions it must be kept under control by reducing the dosage in critical areas that might be associated to overexposure. High energy electrons will easily forward scatter within the resist and undergo further scattering, which is especially prevalent in thicker resists. This can lead to the exposure of regions that are not being directly exposed by the e-beam [41].

Additionally, being based on the phenomenon of interaction between electrons and a generic material, the latter should be able to electrically conduct so as to avoid charging effects that may cause beam distortion and lead to fabrication artifacts.

Physically speaking this means that the feature size that can be produced is not only dependent on the beam resolution, and thus on the energy of the incoming electrons and the resist employed, but it also depends on the adjacent areas that have already been exposed to the e-beam and more importantly to the leftover charges in the form of secondary electrons propagating laterally throughout the surface of the resist. It should now be clear that employing a non-conductive material for EBL is a great disadvantage and, in some cases, might be prohibitive. Manufacturers are able to produce commercial resists that act as conductive thin layers that can thus help disperse charges that might otherwise be accumulated on the surface during the process. Further grounding of the surface can be achieved by applying carbon tape to connect the sample to the sample holder.

It should be noted that the sequential nature of writing associated to EBL makes it a fabrication process that is not feasibly for mass production due to its long writing times. Nevertheless, it remains the most refined technique that can be employed to produce high-resolution nanoscale patterns.

Medusa 82 Resist Without Hard Mask

The first fabrication attempts to pattern 200 nm TiO_2 were made by employing the high-resolution negative resist Medusa 82 (product SX AR-N 8200/1 from Allresist) reported to reach resolutions down to 10 nm.

The fabrication steps followed the procedure provided by the manufacturer (Figure 4.4) of the resist and developer:

1. Spincoat 50 nm of resist on top of the sample.
2. Softbake the coated sample at 150°C for 10 minutes.
3. Expose the sample at an acceleration voltage of 30 kV and at 1000 $\mu C/cm^2$.
4. Hardbake the exposed sample at 170°C for 10 minutes to enhance the sensitivity of the exposed resist to the developer.
5. Place the exposed sample in the respective developer (AR 300-44) for 90 seconds, followed by 30 seconds of rinsing in deionized water.

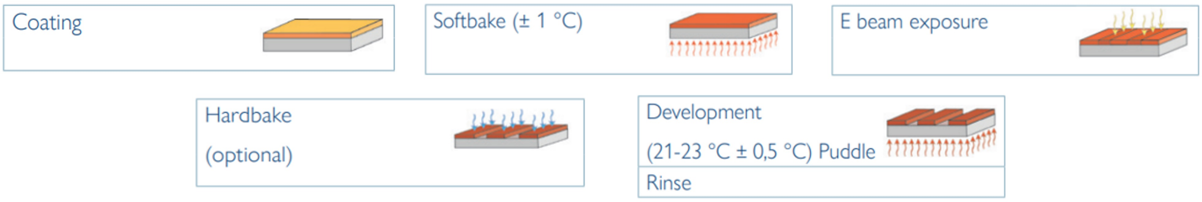

Figure 4.4: Schematic representation of the sample preparation according to the resist supplier (Allresist).

As will be discussed in the chapter on dry etching, this fabrication attempt did not succeed since the resist was too thin to survive the time required to etch the underlying titanium dioxide 200 nm film. The option of increasing the resist thickness was considered even if it would decrease the feature size resolution for reasons explained above. However, the following etching attempts revealed that it would not solve the issue, since the etching rates associated to the full anisotropic 200 nm etching needed for the pattern would still not be suitable to the higher resist thickness.

Charging effects did not seem to pose an issue in terms of geometrical features, although they negatively affected SEM imaging (Figure 4.5 and 4.6, hence no additional charge dissipative film (e.g. Electra 92 from Allresist) was spincoated on top of the resist.

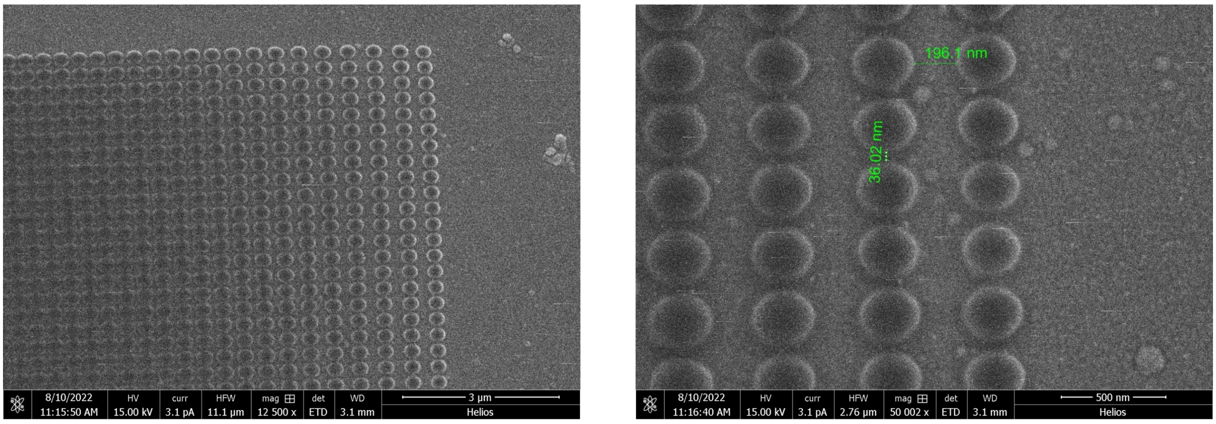
8/10/2022 11:15:50 AM | HV 15.00 kV | curr 3.1 pA | HFW 11.1 µm | mag 12 500 x | det ETD | WD 3.1 mm | 3 µm | Helios
196.1 nm
36.02 nm
8/10/2022 11:16:40 AM | HV 15.00 kV | curr 3.1 pA | HFW 2.76 µm | mag 50 002 x | det ETD | WD 3.1 mm | 500 nm | Helios

Figure 4.5: SEM images of TiO_2 Mie resonances based metasurface after EBL exposure.

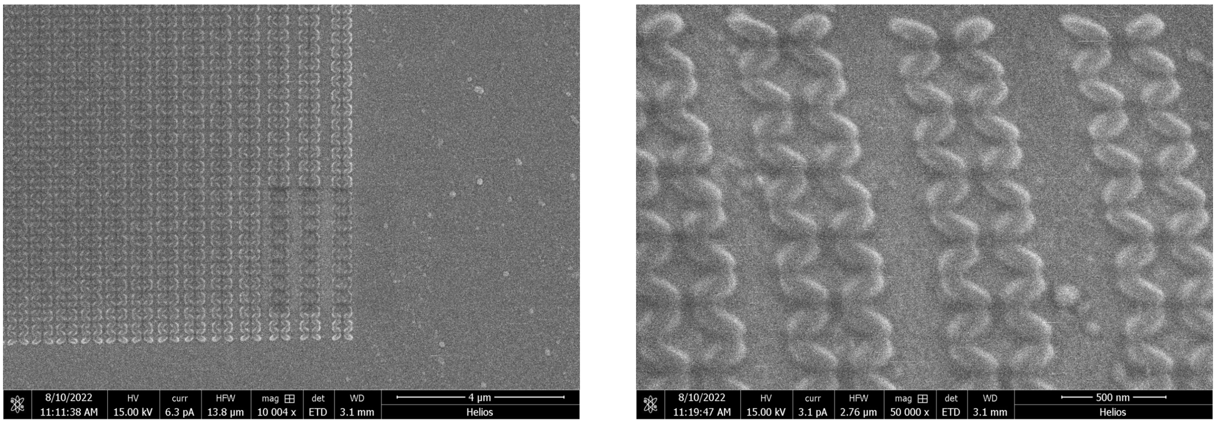
8/10/2022 11:11:38 AM | HV 15.00 kV | curr 6.3 pA | HFW 13.8 µm | mag 10 004 x | det ETD | WD 3.1 mm | 4 µm | Helios
8/10/2022 11:19:47 AM | HV 15.00 kV | curr 3.1 pA | HFW 2.76 µm | mag 50 000 x | det ETD | WD 3.1 mm | 500 nm | Helios

Figure 4.6: SEM images of TiO_2 BIC-based metasurface after EBL exposure.

HSQ Resist with Cr Hard Mask

A more successful attempt at fabrication was made in collaboration with the Institute of Materials Research and Engineering (IMRE) A*STAR.

In this case a 30 nm chromium hard mask was deposited on top of the 200 nm titanium dioxide film to serve as a protective layer during the etching step. Additionally, the resist chosen was HSQ, a negative resist with resolutions comparable to those achievable with Medusa 82, but with better dry etch resistance. A 120 nm HSQ thin film was spin coated at 5000 rpm for 60 seconds, followed by a softbake step at 140°C for 3 minutes. The sample was then exposed through EBL at dosages varying between 0.9 to 1.2 $\frac{\mu s}{dot}$, with the best results later found to be associated to the 1.1 and 1.2 $\frac{\mu s}{dot}$ dosages. The exposed sample was immersed in a salty developer (1 wt.% NaOH and 4 wt.% NaCl in deionized water) for 4 minutes, followed by a rinse in deionized water.

The fabricated structures appeared to be more uniform in size and spatial distribution, with overall fewer defects (Figures 4.8 and 4.9).

4.2.2. Dry Etching of TiO_2

The last step of the fabrication process corresponds with the dry etching of the TiO_2 thin film to transfer the pattern written by the EBL in the previous step. Wet etching has not been considered as a suitable technique due to the impossibility of creating anisotropic patterns with good resolution.

Etching TiO_2 is notoriously difficult due to its high dry etching resistance to most gas compositions. A variety of compositions were tested by subjecting thin films of TiO_2 of known thicknesses to different operating conditions.

Medusa 82 Resist without Hard Mask

As already mentioned, the first fabrication attempts have been made by using the Medusa 82 resist from Allresist, without a chromium hard mask.

The absence of the latter implies that the etching rate of the resist layer must be low enough to survive while the whole 200 nm of TiO_2 below are etched.

Throughout the last few decades, many papers have highlighted the distinction between chemical and physical etching in order to achieve the best possible resolution, anisotropy and surface roughness. The common consensus among researchers is that physical etching often aids chemical etching to create more anisotropic structures, while chemical etching does most of the bulk work in terms of etching rate. Elements such as oxygen and argon are thus often added to gas mixtures to favour physical etching and prevent undercutting at the expense of a lower etching rate. The gas mixtures that have been tested during fabrication in this work follow this same logic since the TiO_2 layer that must be patterned is 200 nm thick, hence in the range of anisotropic etching.

Generally, the etching rate increases with an increased concentration of F atoms in the gas mixture and the operating power. Although these trends are still valid, etching a complex geometrical pattern requires more fine tuning to achieve good etching anisotropy, selectivity, resolution, and surface morphology [1, 4, 26, 34]. The formation of both temporary and permanent side products during the process must also be considered [14].

Table 4.1 show the combinations of gas mixtures, operating powers, and etching times were tested to estimate the best combination of parameters.

In all attempts, the resist was etched much faster than the TiO_2 200 nm layer beneath, leading to overetching of the latter and unsuccessful pattern transfer. Consequently, these compositions cannot be deemed applicable to produce TiO_2 patterns of this thickness.

Gas mixture	Composition [sccm]	Power [W]	Etching rate [nm/min]
CF_4:Ar	18 : 6	30	2.5
		40	2.5 - 3
		100	Very inhomogeneous
CF_4	25	80	6 - 8
CHF_3:O_2	18 : 6	40	4.5
		100	5 – 6.8
CHF_3	23	40	1.2
		100	6.5 - 8.5

Table 4.1: Table of all operating parameters tested to dry etch TiO_2

HSQ Resist with Cr Hard Mask

A series of successful dry etching attempts have been possible with the support of our collaborators in IMRE A*STAR. Their state of the art facilities allow for precise control of the etching parameters for a variety of materials, meaning that a 40 nm chromium thin film can be deposited on top of the titanium dioxide layer in order to act as a hard mask to then be subsequently etched without loss of resolution or anisotropy.

This process (Figure 4.7) uses an hydrogen silsesquioxane resin based negative resist (HSQ) that is very similar to the Medusa 82 resist described above. After EBL, the sample is immersed in a salty developed (1 wt.% NaOH and 4 wt.% NaCl in deionized water) for roughly 4 minutes and is then rinsed with deionized water to halt development.

Following development, the HSQ layer will have been patterned according to what has been written during EBL, hence the chromium hard mask underneath can now be selectively etched to expose the TiO_2 bottom layer. The chromium thin film is etched using inductively-coupled plasma reactive ion etching (ICP-RIE) with a mixture of Cl_2 and O_2.

The TiO_2 can now be selectively etched with CHF_3 gas. During this process the top HSQ layer will gradually etch eventually exposing the Cr hard mask underneath. The latter will act as a protective layer since its etching rate in CHF_3 is much lower than that of TiO_2.

Depending on the thickness of the TiO_2 layer, a leftover thin film of chromium might be left on top of the now patterned TiO_2. Being a dissipative material by nature, it is important for the residual chromium to be removed so as not to worsen the optical properties of the device. To do so the sample is immersed in commercially available chromium liquid etchant for a few minutes. The sample is then rinsed in deionized water and IPA, and then dried with N_2.

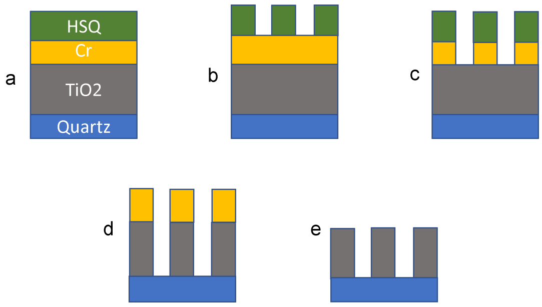
a
HSQ
Cr
TiO2
Quartz
b
c
d
e

Figure 4.7: Schematic representation of the fabrication process using a chromium hard mask. a) Unpatterned sample. b) EBL exposure and development of HSQ resist. c) ICP-RIE of Cr hard mask. d) CHF_3 RIE of TiO_2. e) Cr wet etching.

Figures 4.8 and 4.9 show the metasurfaces throughout the improved fabrication process.

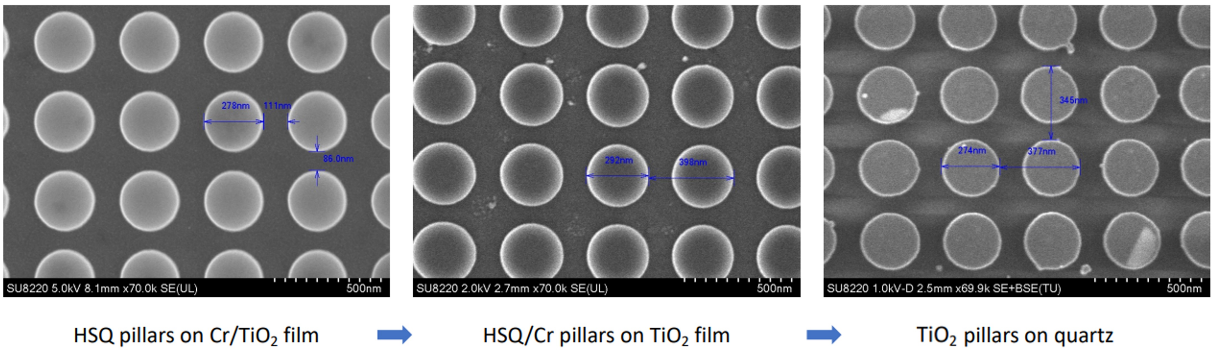
278nm
111nm
86.0nm
SU8220 5.0kV 8.1mm x70.0k SE(UL)
500nm
292nm
398nm
SU8220 2.0kV 2.7mm x70.0k SE(UL)
500nm
345nm
274nm
377nm
SU8220 1.0kV-D 2.5mm x69.9k SE+BSE(TU)
500nm

HSQ pillars on Cr/TiO_2 film → HSQ/Cr pillars on TiO_2 film → TiO_2 pillars on quartz

Figure 4.8: SEM images of the cylinders-based metasurface throughout the fabrication process.

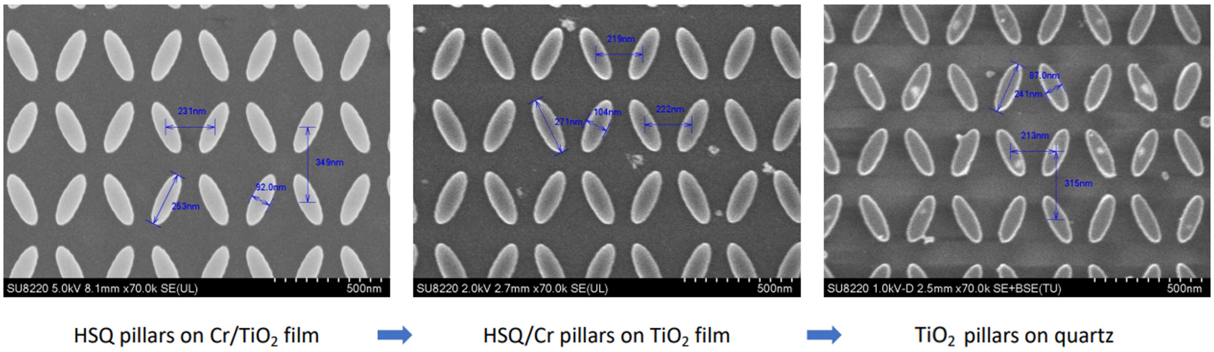
231nm
349nm
253nm
92.0nm
SU8220 5.0kV 8.1mm x70.0k SE(UL)
500nm
219nm
271nm
104nm
222nm
SU8220 2.0kV 2.7mm x70.0k SE(UL)
500nm
87.0nm
241nm
213nm
315nm
SU8220 1.0kV-D 2.5mm x70.0k SE+BSE(TU)
500nm

HSQ pillars on Cr/TiO_2 film → HSQ/Cr pillars on TiO_2 film → TiO_2 pillars on quartz

Figure 4.9: SEM images of the BIC-based metasurface throughout the fabrication process.

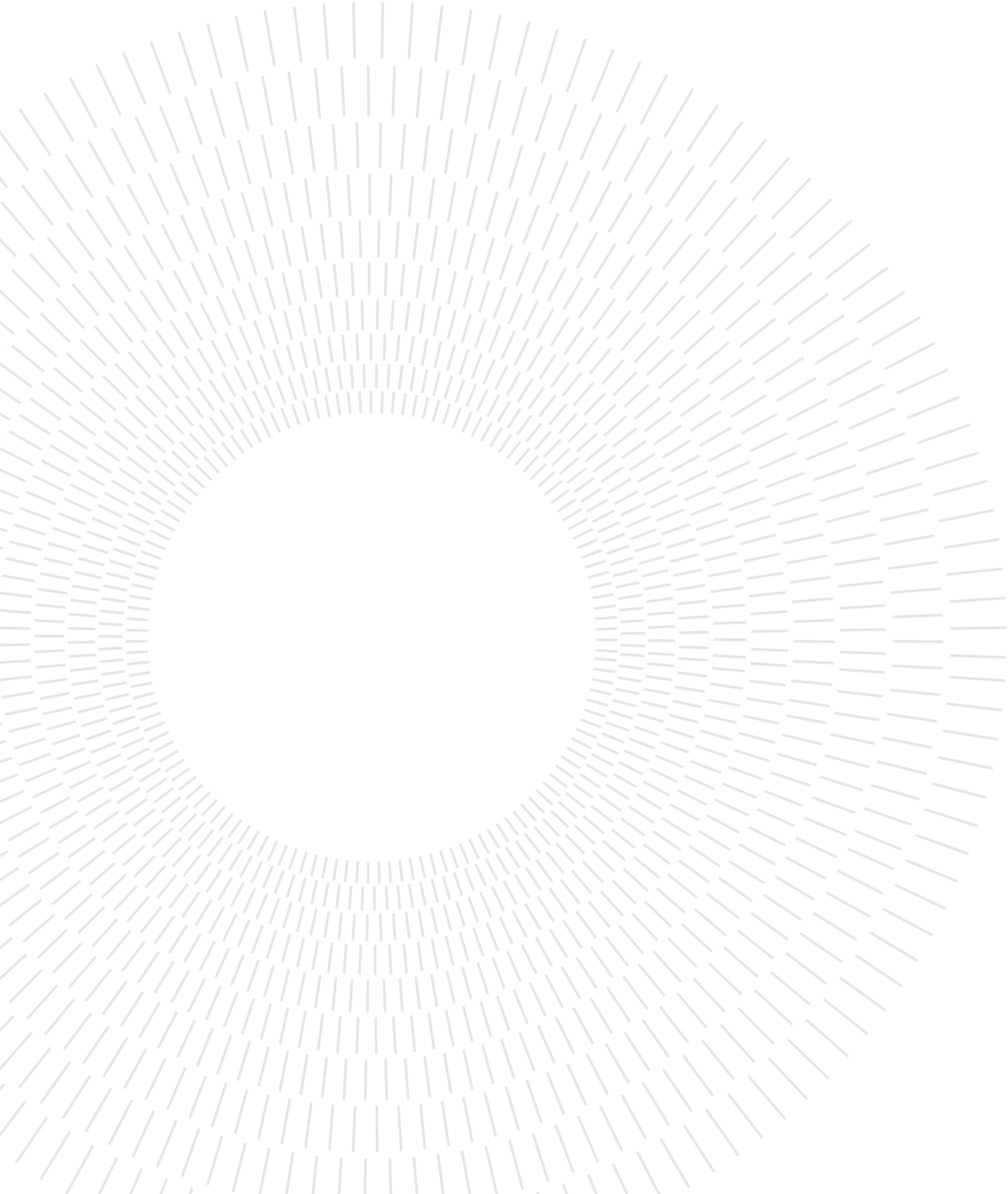

5 | Experimental Results and Discussion

5.1. Characterization of Dielectric Metasurfaces

5.1.1. Normal-incidence Transmittance

The bare fabricated metasurfaces have been characterized by normal-incidence transmittance measurements to confirm the success of fabrication by comparing the spectra of the various arrays to the simulated results.

The schematics of the fabricated structures can be seen in Figure (5.1).

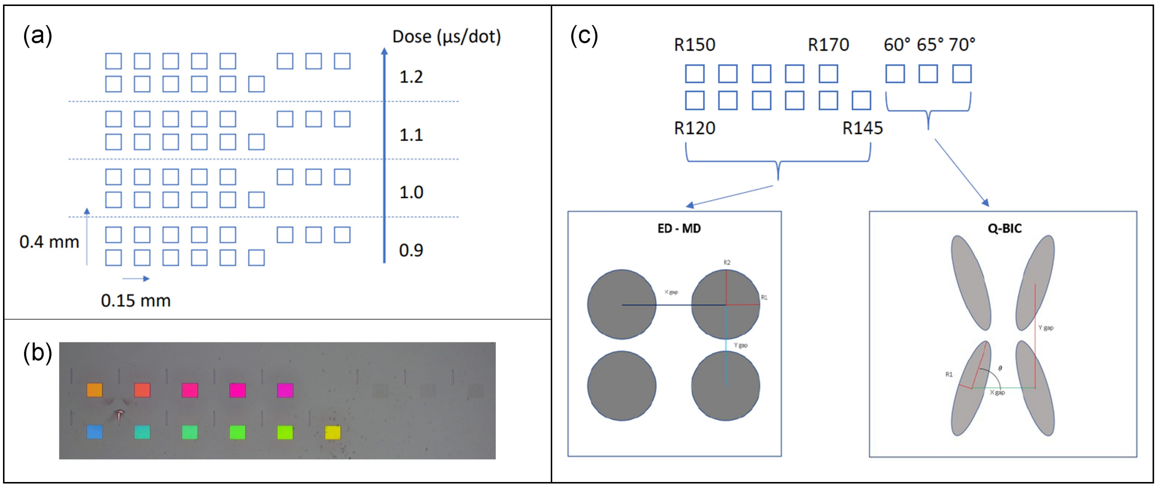
(a)
Dose (μs/dot)
1.2
1.1
1.0
0.9
0.4 mm
0.15 mm
(b)
(c)
R150
R170
60° 65° 70°
R120
R145
ED - MD
R2
X gap
R1
Y gap
Q-BIC
Y gap
R1
θ
X gap

Figure 5.1: Schematic representation of the fabricated arrays. a) Sequence of arrays associated to different dosages employed during EBL. b) Optical micrograph for one of the EBL dosages. c) Schematic representation of the unit cells for the three optical resonances.

The simplified schematics of the optical setup utilized to measure the normal-incidence transmittance is shown in the inset of Figure 5.2.

The normal-incidence spectra of the arrays associated with the MD and ED resonances of the sample that will be referred to as S1 from now on can be seen on the left and right of Figure 5.2 respectively.

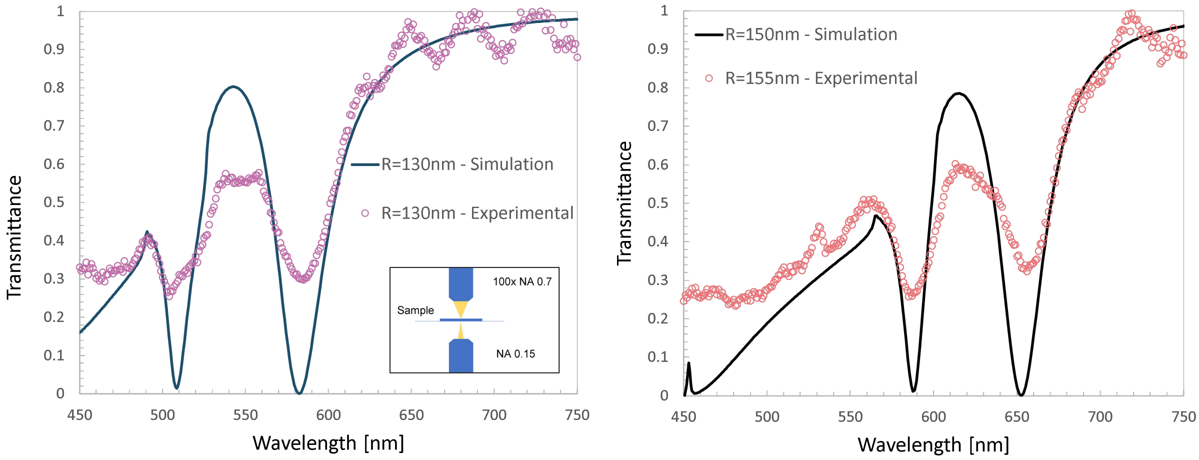

Figure 5.2: Experimental (dotted) and simulated (continuous line) transmittance spectra of the magnetic dipole (left) and electric dipole (right) Mie resonances. The respective dips in transmittance are shown to overlap with the emission wavelength of the J-aggregate (589 nm). The inset shows the simplified schematics of the optical setup used for the measurements.

The MD resonance (left panel of Figure 5.2) seems to precisely match the simulated results. The ED resonance (right panel of Figure 5.2) is slightly blueshifted with respect to the simulated results due to fabrication tolerances, meaning that the resonance that matches the experimental results is associated with the array of radius $R = 155\ nm$).

In both cases, the overall lower values of transmittance can be attributed to inevitable fabrication tolerances and intrinsic Ohmic losses of the TiO_2 thin film. This should not pose an issue since the presence of the TDBC thin film will increase the resonance strength due to its high refractive index, as shown for the passive structure in the chapter on simulations and as will also be shown by the angle-resolved photoluminescence measurements in this chapter.

These measurements have been repeated for all arrays, allowing us to evaluate the quality of fabrication for each dosage and sample. Figure 5.3 shows the normal-incidence transmittance spectrum for the radius sweep associated to the highest dosage, these results can be compared to the simulated spectra in the right panel of the same figure. The match between the experimental results for this sample can be considered as excellent, hence the metasurfaces in this sample can be used as substrates for the TDBC thin film deposition step.

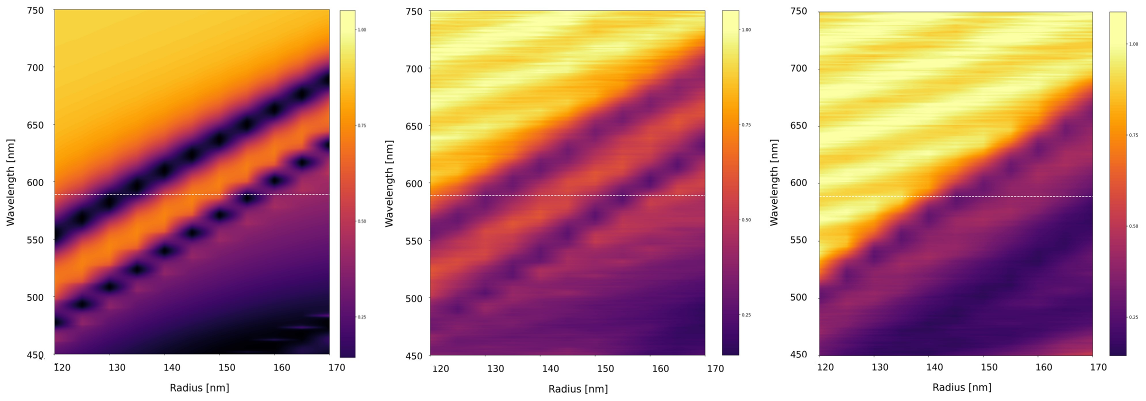

(a) (b) (c)

Figure 5.3: Comparison between the simulated (a) and experimental (b,c) normal-incidence transmittance for unit cells of different radii for samples S1 and S2. The MD and ED bands are shown to perfectly match between the experimental and calculated results for S1. The bands of the fabricated arrays of sample S2 are blueshifted with respect to the simulated results because of fabrication tolerances.

The two bands associated to the dips in transmittance found in both the simulated and experimental spectra can be seen to match the bands highlighted in Figure 3.4b.

A less successful fabrication attempt (sample S2) is shown in Figure 5.3. In this case, every resonance of each array is blueshifted with respect to the simulated data. This shift can be attributed to overetching of the structures since the error seems to be of systematic nature for the whole sample.

The transmittance spectra of three Q-BIC arrays fabricated in S1 are shown in Figure 5.4. The measured transmittance is compared with the simulated results to highlight that none of the arrays can exhibit the Q-BIC mode in terms of both resonance strength and linewidth. This failure can be attributed to the strict fabrication constraints required for the successful emergence of Q-BIC in fabricated structures. Furthermore, the extent of periodicity of the array determines the linewidth or Q-factor of quasi-bound states in the continuum, resulting in a reduction of these quantities in real finite metasurfaces, irrespective of fabrication tolerances.

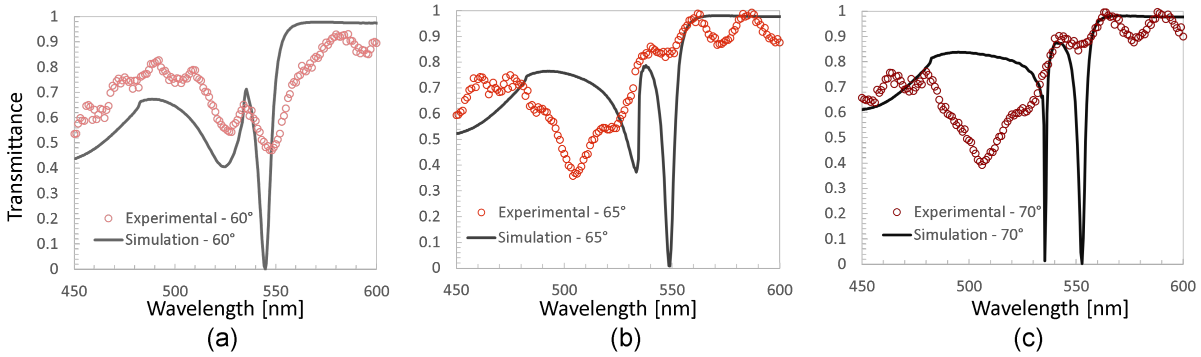

Figure 5.4: Experimental normal-incidence transmittance measurements for the Q-BIC resonances in sample S1 shown not to match the experimental results due to fabrication tolerances.

As previously noted in the chapter on simulation results, the resonance wavelength of the bare metasurface does not match that of the TDBC emission peak since the presence of the high refractive index emissive thin film will inevitably alter the spectral position of the optical resonance, Therefore, the design of the metasurface should be based on the optical spectrum of the passive metasurface instead of the bare one. Moreover, this type of Q-BIC has been shown to be highly sensitive to refractive index changes around the resonators [42], providing further justification for this design decision.

5.2. Characterization of J-Aggregates Thin Films

The normal photoluminescence spectrum of the TDBC:PVA thin film is shown in Figure 5.5. The peak around 589 nm is associated to the emission from the grown J-aggregates, while the low-intensity peak around 535 nm is attributed to the leftover monomers that can still be found in the PVA matrix.

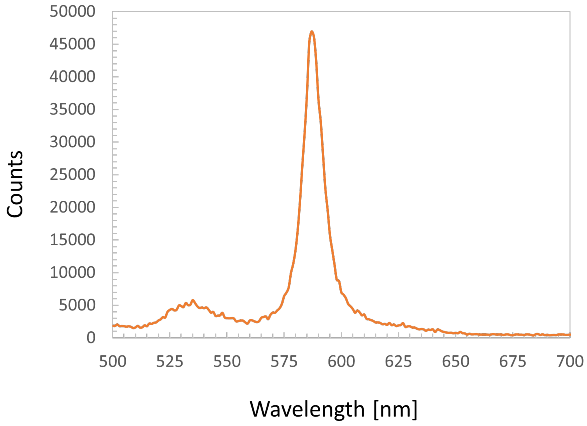

Figure 5.5: Experimental normal-incidence photoluminescence spectrum of TDBC J-aggregates dispersed in a PVA matrix showing the low-intensity 535 nm monomer emission and the significantly stronger 589 nm J-aggregate emission.

All details regarding the specific experimental parameters used to optimize the growth of the molecular aggregates that will be measured in this section can be found in Chapter 4.2.2.

5.2.1. Photoluminescence as a Function of Pumping Power

The optical properties of J-aggregates have been shown to be influenced by the pumping power used to excite their emission [27]. The reason being that the ordered chain of unit molecules found in aggregates are able to couple with each other and radiate coherently (Chapter 2.2.1), meaning that the resulting emission will depend on the number of units that are coupled and thus to the pumping power they are subjected to.

This phenomenon can be quantified by measuring the response of the aggregates to different excitation powers. Theoretically, the maximum of photoluminescence should be proportional to the square number of coupled monomers, experimentally the coherence length of the aggregate is strongly dependent on environmental conditions and is often limited to a just a few tens of units [6, 49, 69] with the higher values associated with lower temperatures. These limitations will inevitably alter the response of the aggregates, the photoluminescence dependence on the pumping power will not emerge as a typical square law, and the threshold for cooperative emission will not be as sharp.

To highlight this characteristic property of J-aggregates a series of normal-incidence photoluminescence measurements have been performed on a TDBC:PVA thin film on a 1 mm quartz substrate. The film has been excited by a pulsed laser at an excitation wavelength of 405 nm with a repetition rate of 80 MHz over a range of roughly $10 - 90\ \mu W$ of excitation power with a 100x objective.

Figures 5.6a and 5.6b show the response of two identical samples subjected to varying excitation powers. Both samples manifest a non-linear response of the aggregate with respect to the pumping power, but the amount of data points cannot be deemed sufficient to make any definitive conclusion.

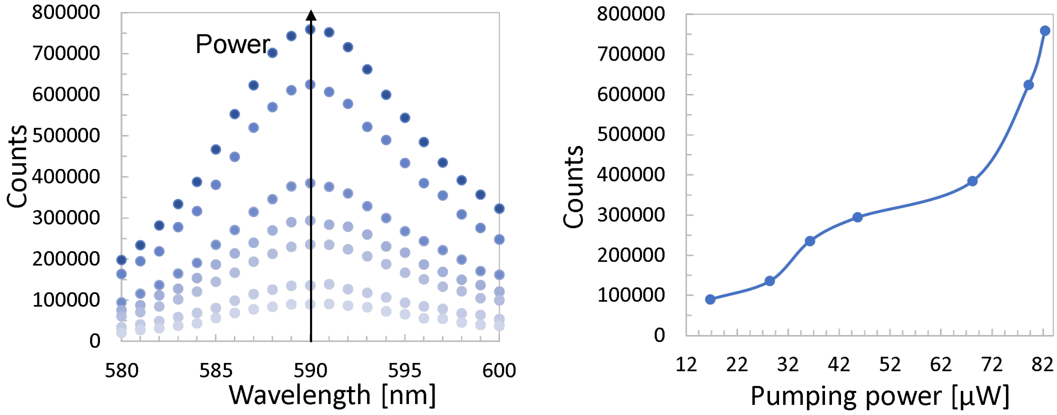

(a) Sample A

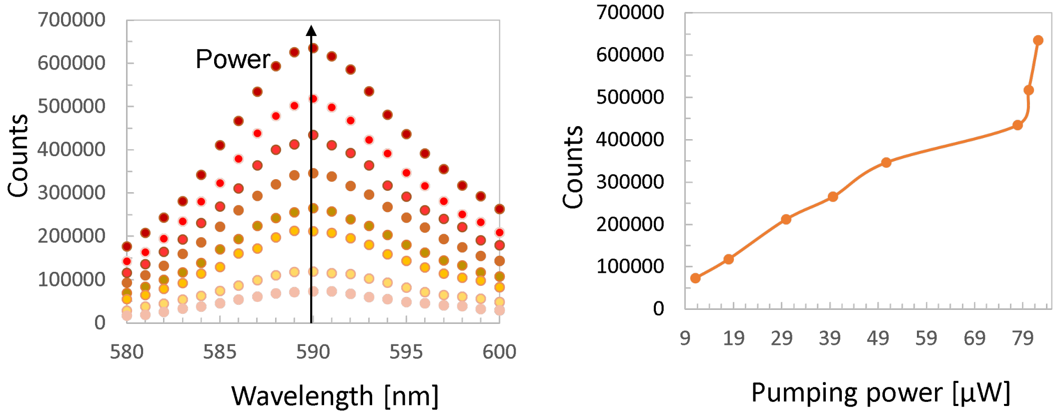

(b) Sample B

Figure 5.6: a) PL measurements as a function of pumping power for sample A. b) PL measurements as a function of pumping power for sample B. Both samples show preliminary evidence of non-linear emission.

In order to be able to make more conclusive statements on the emergence of cooperativity more data points are required. A combination of optical filters and glass slides has been employed to modulate the pumping power (Figure 5.7 (a,b)). Additionally, in view of the higher number of measurements to be performed on the same spot, the optical path of the laser was covered between each measurement so as to reduce the exposure of the sample to the laser to avoid photobleaching. In these sets of experiments, a final measurement at the highest power in the range was performed and its peak intensity was compared to that of the first measurement in the set to confirm that photobleaching had not taken place.

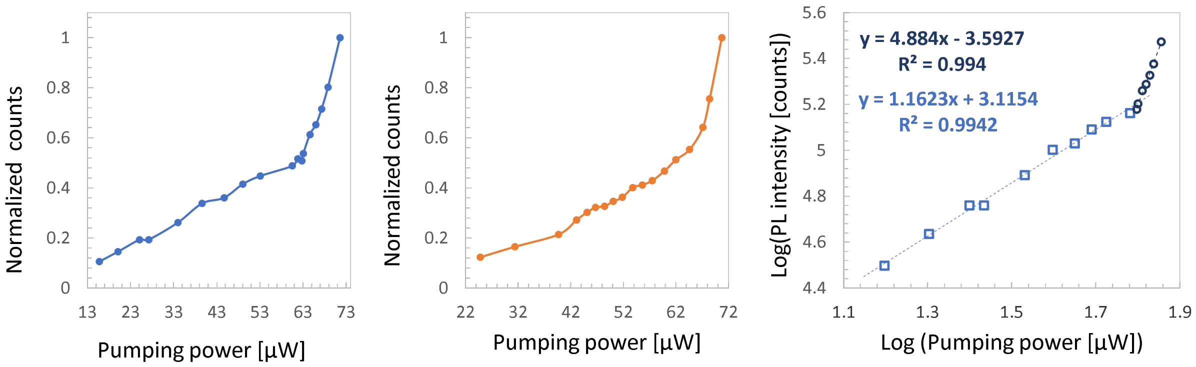

(a) (b) (c)

Figure 5.7: a,b) Normal-incidence photoluminescence measurements for sample A (a) and B (b). c) Double logarithmic plot of the normalized peak intensity of photoluminescence against the pumping power showing a noticeable change in trend associated to cooperative emission.

A closer look at the data in Figure 5.7 shows that the optical response of the aggregate can be split into two regions by a pumping power threshold of roughly $P_{threshold} = 60\ \mu W$. This behaviour is further highlighted in the double logarithmic plot in Figure 5.7. While the data points before the threshold can be fit with the equation of a straight line, those following the threshold power are perfectly fit by the exponential function $f(x) = x^{4.884} \cdot 10^{-3.5927}$ meaning that the optical behaviour of the aggregate has undergone a substantial change after what has been identified as the pumping threshold. This shift in response could be attributed to preliminary evidence of the emergence of cooperativity of emission associated to more coupled aggregate sub-units induced by the increased pumping power. An analogous behaviour has also been found in the response of sample B.

5.3. Characterization of the Coupled System

5.3.1. Angle-resolved Photoluminescence Measurements

Angle-resolved photoluminescence (ARPL) measurements were performed for the final device in order to study the influence that the presence of a metasurface designed to work on-resonance with the emission wavelength of the (TDBC) thin film has on the emissive properties of the latter.

These measurements aim to investigate two phenomena in particular:

- The extent of coupling between the incoming photons, the optical cavity, and the molecular aggregates thin film. With the possibility to observe exciton-polaritons in the event of strong light-matter coupling.
- The influence the optical bands associated to the metasurface have on the directionality of emission of the molecular aggregates. With possible implications related to the phenomenon of controlled superradiance.

Regarding the fist point, exciton-polaritons are hybrid quasiparticles that are formed from the coupling of light and matter. They can be observed as a series of peaks in the ARPL spectrum of a device. The ability to observe polaritons experimentally can depend on a number of factors, including the strength of the coupling between light and matter, the intensity of the excitation, and the experimental techniques that are used.

The spectral fingerprint of exciton-polaritons that can be identified in ARPL spectra is the presence of dispersion bands arising from the dependence of the polariton peaks from the angle of emission. This angle dependence exists due to the hybrid nature of these quasi-particles [3]. The polariton bands will share some characteristic of the exictonic band and some of the photonic band of the metasurface. Under favorable conditions, both the upper and lower polariton bands may emerge. However, the lower polariton is typically easier to observe experimentally, since it has a lower energy and greater stability than the upper polariton.

To perform ARPL measurements, the sample is irradiated with a beam of light, which excites electrons in the sample to higher energy states. These excited electrons then relax back to their ground state by emitting a photon of light. The emitted photons are detected at different angles in order to highlight the angle-dependent emissive behavior of the sample.

The setup schematics can be found in Figure 5.8.

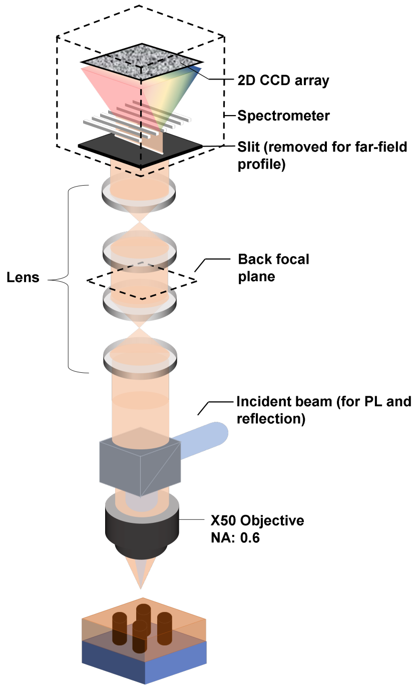
2D CCD array
Spectrometer
Slit (removed for far-field profile)
Back focal plane
Lens
Incident beam (for PL and reflection)
X50 Objective
NA: 0.6

Figure 5.8: Schematics of the optical setup utilized for AR-PL measurements.

The ARPL spectra have been captured using an inverted optical microscope (Nikon Ti-U), a spectrograph (Acton IsoPlane SCT 320), and a charged-coupled detector (CCD, Andor iDus 420). A system of lenses was used to project the back focal plane of the collection objective (Nikon x50, $NA = 0.6$) onto the slit of the spectrograph (Figure 5.8). The excitation wavelength has initially been set to 400 nm.

The ARPL spectrum for the resonators with $R = 120\ nm$, associated to the normal-incidence magnetic dipole Mie resonance is shown on the right in Figure 5.9. The broad emission band with no angle dependence centered at 590 nm is associated to the exciton of the TDBC thin film. The other bands with a strong angle dependence can instead be attributed to the photonic bands of the metasurface as shown in the left panel of Figure 5.9. The low intensity to noise ratio for this array can be attributed to the low pumping wavelength of 400 nm which is far from the peak absorption of the molecular aggregate, and to the optical resonance being detuned from the exciton resonance wavelength due to fabrication tolerances thus making the metasurface a less optimal cavity. These issues lead to an overall lower coupling strength between the exciton and the metasurface. Regardless, the structure is able to reach the weak coupling regime as shown by the optical bands being populated by photons at energies different from that of the pure excitonic state.

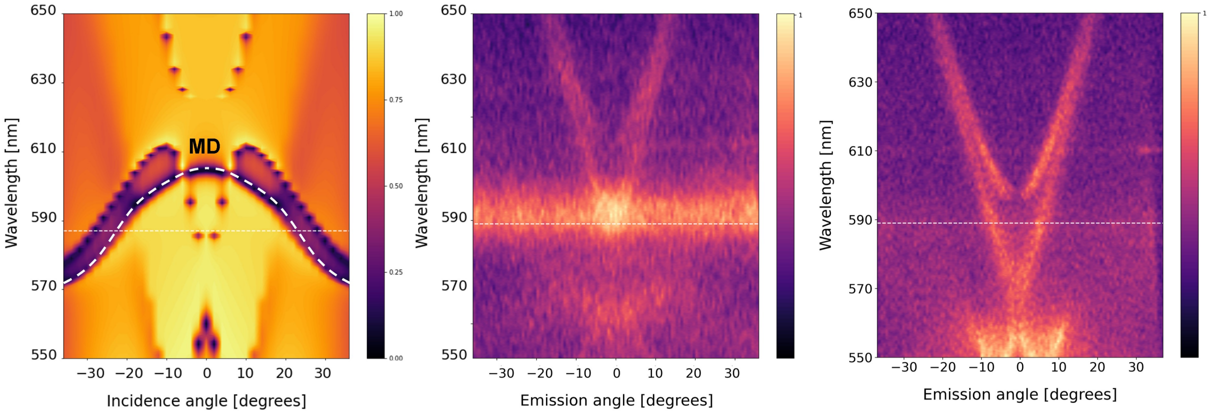

(a) (b) (c)

Figure 5.9: Simulated passive spectrum (a) and measured ARPL spectrum (b,c) for the normal-incidence MD dipole resonance of two distinct samples (S1 in (b) and S3 in (c)) showing varying degrees of coupling between the J-aggregate thin film and the dielectric metasurface.

Although samples S1 and S3 were fabricated following the same experimental parameters and procedures, the optical response of the device between the two is clearly different as shown by the ARPL spectra in Figure 5.9 (b,c). In particular, while sample S1 shows a broad excitonic peak centered at 589 nm with no angle-dependence and weakly populated photonic bands, sample S3 instead shows a very weak excitonic peak and much more defined photonic bands. This allows us to qualitatively assess that the coupling between the dielectric metasurface and the molecular aggregate thin film is stronger for sample S3 since the exciton has been imparted with a strong angular dependence of emission. This trend holds true for all spectra attributed to sample S3 as will be shown in the following paragraphs.

Analogous measurements have been made for the normal-incidence ED ($R = 130\ nm$), the higher angles ED ($R = 155\ nm$), and the ED Q-BIC (ellipsoidal pillars) arrays analysed in Chapter 3.3.4. The comparisons are showed, respectively, in Figures 5.10, 5.11, 5.12.

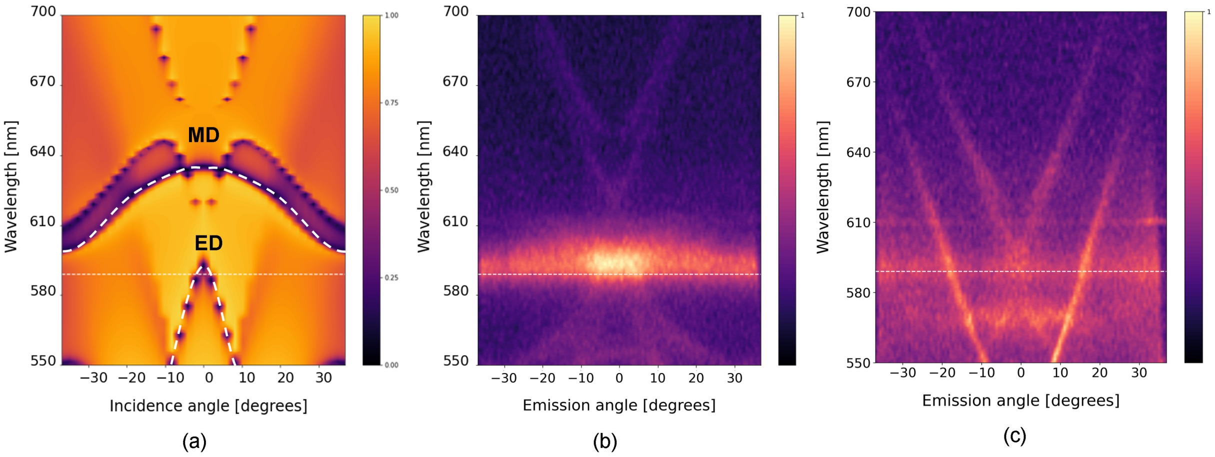

Figure 5.10: Simulated passive spectrum (a) and measured ARPL spectrum (b,c) for the normal-incidence ED resonance of two distinct samples (S1 in (b) and S3 in (c)) showing varying degrees of coupling between the J-aggregate thin film and the dielectric metasurface.

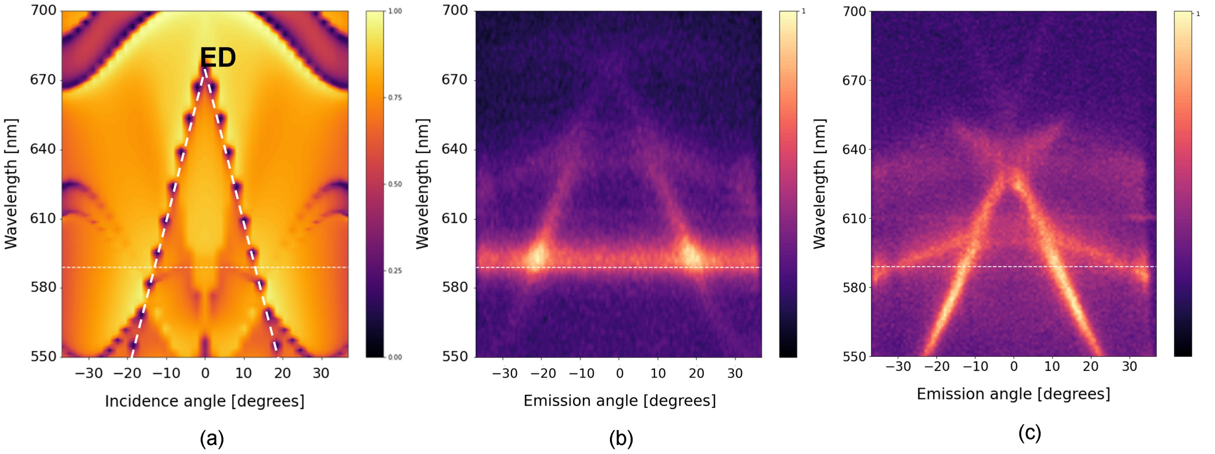

Figure 5.11: Simulated passive spectrum (a) and measured ARPL spectrum (b,c) for the higher angles ED resonance of two distinct samples (S1 in (b) and S3 in (c)) showing varying degrees of coupling between the J-aggregate thin film and the dielectric metasurface.

As shown by the ARPL in Figures 5.10 and 5.11, the coupling between the metasurface and the TDBC thin film for these two arrays is much better compared to the normal-incidence MD (Figure 5.9) and ED Q-BIC (Figure 5.12) resonances. Both of these structures are able to couple with the exciton efficiently enough to show a sizeable difference in the directionality of emission of the J-aggregates. In fact, the angle-independent emission band of the exciton has now been imparted with an angle-dependent emissive behavior due to the available photonic bands of the metasurfaces.

In this context, the photons associated with the incoming 400 nm radiation are localized within the TDBC thin film by the interaction with the resonators and are then able to excite the 589 nm emission from the J-aggregates. The newly emitted photons are then affected by the optical resonance of the metasurface and thus further localized within the TiO_2 resonators. This last step allows the emitted photons to be confined within the optical bands of the metasurface, leading to angle-dependent emission.

As already mentioned earlier in this chapter, the fabrication attempt for the ED quasi-bound state in the continuum did not succeed due to considerable overetching of the ellipsoidal resonators as already confirmed by SEM imaging (Figure 4.9) and normal-incidence transmittance measurements (Figure 5.4). This can also be seen in Figure 5.12, in which the optical bands of the Q-BIC can be identified but it is considerably redshifted with respect to the excitonic resonance.

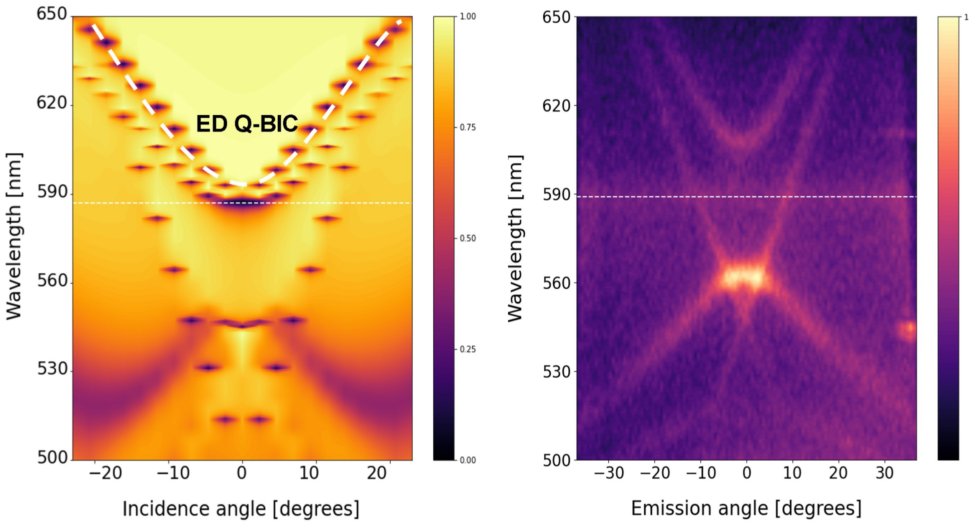

(a) (b)

Figure 5.12: Simulated passive spectrum (a) and measured ARPL spectrum (b) for the symmetry protected electric dipole quasi-bound state in the continuum optical resonance. The band structure of the measured spectrum perfectly matches the shape of the simulated band structure but is redshifted and thus not overlapping with excitonic peak.

These sets of measurements demonstrate that the directionality of emission of J-aggregates based thin film can be tuned by weakly coupling to dielectric metasurfaces. As shown above, the extent of coupling and directionality imparted to the aggregates depends on fabrication tolerances. Hence, in order to be able to precisely impose directionality to the emissive aggregates further improvements in nanofabrication techniques are necessary.

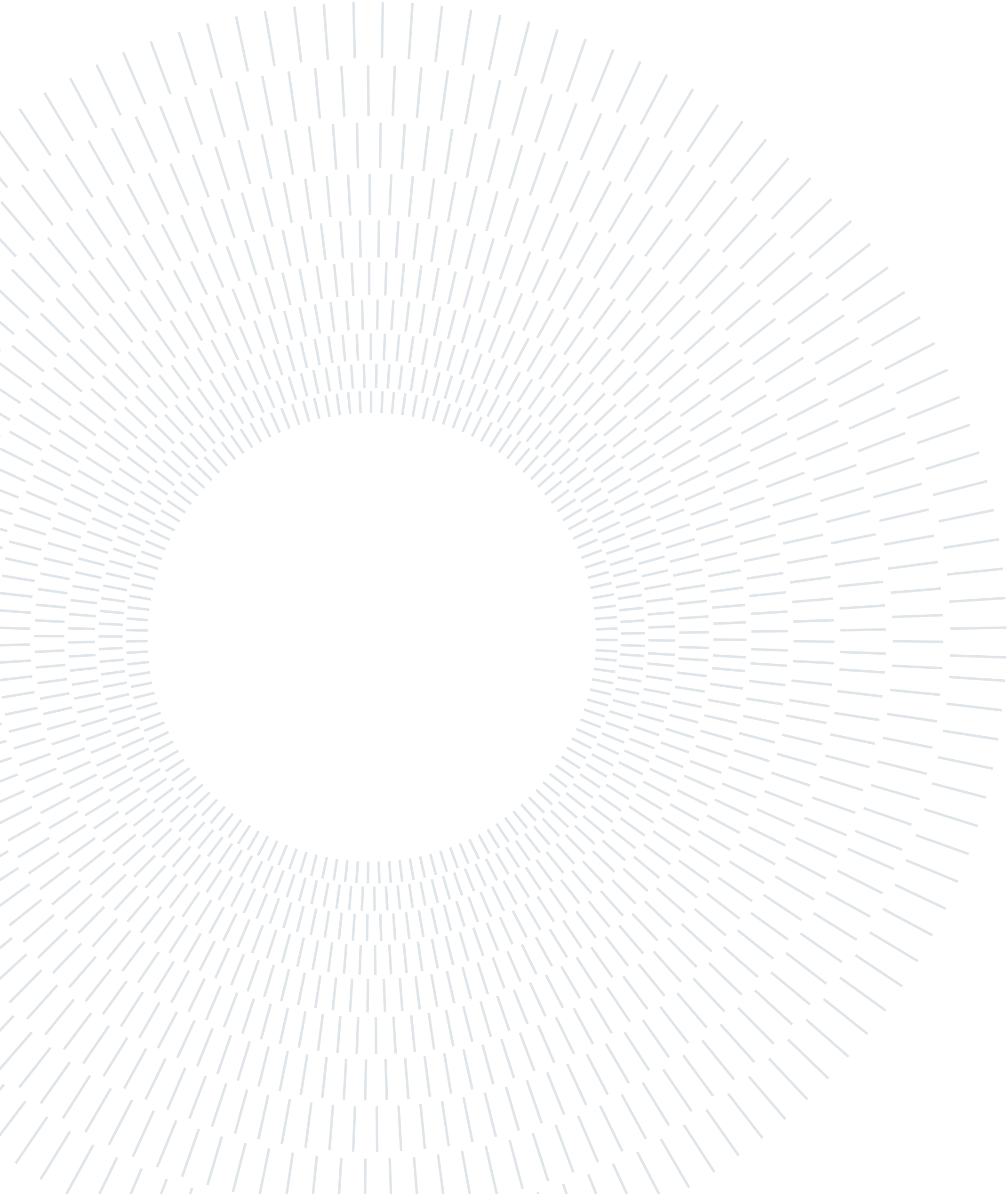

6 | Conclusions and Future Work

The aim of this thesis was to design dielectric metasurfaces with optical resonances that would overlap with the molecular exciton of J-aggregates so that the response of the latter could be investigated and could be tuned, in terms of its directionality and strength of emission. Additionally, this would serve as ground work to further push the limits of these unique hybrid systems to foster the emergence of superradiance in J-aggregates.

To achieve this, the behavior of J-aggregates thin films coupled to dielectric metasurfaces operating under a variety of optical resonances in the visible spectrum and at room temperature has been thoroughly investigated. Through careful design, accounting for the inevitable presence of fabrication tolerances, robust optical resonances were achieved, overcoming some of the challenges of nanofabrication and paving the way for the design of resonators with more complex geometries. The emissive couterpart of the device was also tuned in terms of its synthesis and deposition so that it would not bottleneck the performance of the device.

The fabricated metasurfaces were then integrated with the tuned emissive J-aggregates thin film so that the coupling between the two structures would allow us to study their interaction and the shift in optical response of the latter. To do so the band structure of the fully integrated device was first simulated and then investigated through angle-resoved photoluminescence measurements so that a direct comparison between simulated and experimental data could be made. This process allowed us to study the effects that different resonant cavities, working under distinct types of optical resonances, have on the emissive behaviour of J-aggregates.

These measurements showed that the two structures were able to couple efficiently and thus the incoming photons, localized by the metasurface, were able to strongly excite the molecular aggregate thin film and cause the newly emitted photons to populate the band structure of the metasurface leading to a change in both wavelength and directionality of emission. The latter was shown to be highly tunable with changes in the geometry of the resonators, allowing us to control the generally angle-independent emission of J-aggregates to be directional. This phenomenon was demonstrated with varying degrees of success but was nonetheless shown to be reproducible between different samples, with the only difference being the extent of coupling between the two materials which has been qualitatively evaluated by comparing the shift in angle-dependence of the weakly coupled excitonic emission between different samples.

Additionally, the decay rate of the excited states of J-aggregates is increased due to both the intrinsic properties of the aggregates and the Purcell effect induced by the metasurface working as an optical cavity. This phenomenon can be further enhanced by inducing superradiance in the J-aggregates, meaning that even faster devices could be theoretically fabricated. In this regard, the metasurface could foster room-temperature superradiance by localizing the electromagnetic field of the incoming excitation between the J-aggregates, leading to the development of ultrasfast and high-directionality devices with a reduced power threshold for the emergence of superradiance.

Within this context, further improvements in the quality of the fabricated metasurfaces will provide researchers with more strongly coupled systems and the formation of exciton-polaritons whose directionality and rate of emission could be tuned by the specific design of the metasurface as was demonstrated for the weakly coupled excitons. Another advantage of molecular aggregates based thin films is that the refractive index of the TDBC:PVA film can be tuned by changes in concentration of both components, opening up further opportunities of tuning the radiative properties of the emissive component in the device.

This work has bridged the gap between the field of molecular excitons and metasurfaces, establishing foundational work to further develop hybrid devices with tunable directionality and rate of emission. Being able to foster superradiance at room temperature would mean demonstrating the first evidence of non-isolated superradiant J-aggregates, thus allowing researchers to develop ultrafast and high-directionality emitters at room temperature and in the visible spectrum.

Bibliography

[1] Dry etch chemistries for tio2 thin films. doi: 10.1016/S0169-4332(01)00562-1.

[2] Quality factor calculations for a resonant cavity, ansys optics. URL `https://optics.ansys.com/hc/en-us/articles/360041611774-Quality-factor-calculations-for-a-resonant-cavity`.

[3] The physics of exciton-polariton condensates.

[4] R. Adzhri, M. K. Arshad, M. F. Fathil, U. Hashim, A. R. Ruslinda, R. M. Ayub, S. C. Gopinath, C. H. Voon, K. L. Foo, M. N. Nuzaihan, A. H. Azman, and M. Zaki. Reactive ion etching of tio2 thin film: The impact of different gaseous. *2015 IEEE Regional Symposium on Micro and Nanoelectronics (RSM)*, 12 2015. doi: 10.1109/RSM.2015.7354999.

[5] A. Ambrosio. Structuring visible light with dielectric metasurfaces. *Journal of Optics*, 20: 113002, 10 2018. ISSN 2040-8986. doi: 10.1088/2040-8986/AAE3D0.

[6] S. B. Anantharaman, J. Kohlbrecher, G. Rainò, S. Yakunin, T. Stöferle, J. Patel, M. Kovalenko, R. F. Mahrt, F. A. Nüesch, and J. Heier. Enhanced room-temperature photoluminescence quantum yield in morphology controlled j-aggregates. *Advanced Science*, 8: 1903080, 2 2021. ISSN 2198-3844. doi: 10.1002/ADVS.201903080.

[7] S. Balci. Ultrastrong plasmon-exciton coupling in metal nanoprisms with j-aggregates. *Optics letters*, 38:4498, 11 2013. ISSN 1539-4794. doi: 10.1364/OL.38.004498.

[8] J. J. Baumberg, J. Aizpurua, M. H. Mikkelsen, and D. R. Smith. Extreme nanophotonics from ultrathin metallic gaps. *Nature materials*, 18:668–678, 7 2019. ISSN 1476-4660. doi: 10.1038/S41563-019-0290-Y.

[9] M. Biliroglu, G. Findik, J. Mendes, D. Seyitliyev, L. Lei, Q. Dong, Y. Mehta, V. V. Temnov, F. So, and K. Gundogdu. Room-temperature superfluorescence in hybrid perovskites and its origins. *Nature Photonics 2022 16:4*, 16:324–329, 3 2022. ISSN 1749-4893. doi: 10.1038/s41566-022-00974-4.

[10] B. Birkan, D. Gülen, and S. Özçelik. Controlled formation of the two-dimensional ttbc j-aggregates in an aqueous solution. *Journal of Physical Chemistry B*, 110:10805–10813, 6

2006. ISSN 15206106. doi: 10.1021/JP0573846. URL `https://pubs.acs.org/doi/abs/10.1021/jp0573846`.

[11] C. F. Bohren and D. R. Huffman. Absorption and scattering of light by small particles. *Absorption and Scattering of Light by Small Particles*, 4 1998. doi: 10.1002/9783527618156.

[12] C. Bonnand, J. Bellessa, and J. C. Plenet. Properties of surface plasmons strongly coupled to excitons in an organic semiconductor near a metallic surface. *Physical Review B - Condensed Matter and Materials Physics*, 73:245330, 6 2006. ISSN 10980121. doi: 10.1103/PHYSREVB.73.245330/FIGURES/8/MEDIUM.

[13] H. T. Chen, Z. Zhou, M. Sukharev, J. E. Subotnik, and A. Nitzan. Interplay between disorder and collective coherent response: Superradiance and spectral motional narrowing in the time domain. *Physical Review A*, 106:053703, 11 2022. ISSN 24699934. doi: 10.1103/PHYSREVA.106.053703/FIGURES/8/MEDIUM.

[14] K. R. Choi, J. C. Woo, Y. H. Joo, Y. S. Chun, and C. I. Kim. Dry etching properties of tio2 thin films in o2/cf4/ar plasma. *Vacuum*, 92:85–89, 2013. ISSN 0042207X. doi: 10.1016/J.VACUUM.2012.11.009.

[15] D. R. Cumming, S. Thoms, S. P. Beaumont, and J. M. Weaver. Fabrication of 3 nm wires using 100 kev electron beam lithography and poly(methyl methacrylate) resist. *Applied Physics Letters*, 68:322, 8 1998. ISSN 0003-6951. doi: 10.1063/1.116073.

[16] A. S. Davydov. Theory of molecular excitons. *Theory of Molecular Excitons*, 1971. doi: 10.1007/978-1-4899-5169-4.

[17] R. H. Dicke, P. Physical, and I. Aboratory. Coherence in spontaneous radiation processes. *Physical Review*, 93:99, 1 1954. ISSN 0031899X. doi: 10.1103/PhysRev.93.99.

[18] P. A. Dmitriev, E. Lassalle, L. Ding, Z. Pan, D. C. J. Neo, V. Valuckas, R. Paniagua-Dominguez, J. K. W. Yang, H. V. Demir, and A. I. Kuznetsov. Hybrid dielectric-plasmonic nanoantenna with multiresonances for subwavelength photon sources. 6 2022. doi: 10.1021/acsphotonics.2c01332.

[19] X. Du, L. Xiong, X. Zhao, S. Chen, J. Shi, and G. Li. Dual-band bound states in the continuum based on hybridization of surface lattice resonances. *Nanophotonics*, 11:4843–4853, 12 2022. ISSN 21928614. doi: 10.1515/NANOPH-2022-0427/ASSET/GRAPHIC/J_NANOPH-2022-0427_FIG_007.JPG.

[20] A. Eisfeld, C. Marquardt, A. Paulheim, and M. Sokolowski. Superradiance from two dimensional brick-wall aggregates of dye molecules: The role of size and shape for the temperature dependence. *Physical Review Letters*, 119:097402, 8 2017. ISSN 10797114. doi: 10.1103/PHYSREVLETT.119.097402/FIGURES/3/MEDIUM.

[21] A. B. Evlyukhin, S. M. Novikov, U. Zywietz, R. L. Eriksen, C. Reinhardt, S. I. Bozhevolnyi, and B. N. Chichkov. Demonstration of magnetic dipole resonances of dielectric nanospheres in the visible region. *Nano letters*, 12:3749–3755, 7 2012. ISSN 1530-6992. doi: 10.1021/NL301594S.

[22] H. Fidder, J. Knoester, and D. A. Wiersma. Superradiant emission and optical dephasing in j-aggregates. *CPL*, 171:529–536, 8 1990. ISSN 0009-2614. doi: 10.1016/0009-2614(90)85258-E.

[23] H. Fidder, J. Terpstra, and D. A. Wiersma. Dynamics of frenkel excitons in disordered molecular aggregates. *The Journal of Chemical Physics*, 94:6895, 8 1998. ISSN 0021-9606. doi: 10.1063/1.460220.

[24] J. Grad, G. Hernandez, and S. Mukamel. Radiative decay and energy transfer in molecular aggregates: The role of intermolecular dephasing. *Physical Review A*, 37:3835, 5 1988. ISSN 10502947. doi: 10.1103/PhysRevA.37.3835.

[25] G. Y. Guralchuk, I. K. Katrunov, R. S. Grynyov, A. V. Sorokin, S. L. Yefimova, I. A. Borovoy, and Y. V. Malyukin. Anomalous surfactant-induced enhancement of luminescence quantum yield of cyanine dye j-aggregates. *The Journal of Physical Chemistry C*, 112:14762–14768, 2008. ISSN 1932-7447. URL `https://www.academia.edu/34631053/Anomalous_Surfactant_Induced_Enhancement_of_Luminescence_Quantum_Yield_of_Cyanine_Dye_J_Aggregates`.

[26] S. Ha, R. Janissen, Y. Y. Ussembayev, M. M. van Oene, B. Solano, and N. H. Dekker. Tunable top-down fabrication and functional surface coating of single-crystal titanium dioxide nanostructures and nanoparticles. *Nanoscale*, 8:10739–10748, 5 2016. ISSN 2040-3372. doi: 10.1039/C6NR00898D.

[27] C. Hettich, C. Schmitt, J. Zitzmann, S. Kühn, I. Gerhardt, and V. Sandoghdar. Nanometer resolution and coherent optical dipole coupling of two individual molecules. *Science (New York, N.Y.)*, 298:385–389, 10 2002. ISSN 1095-9203. doi: 10.1126/SCIENCE.1075606.

[28] C. W. Hsu, B. Zhen, A. D. Stone, J. D. Joannopoulos, and M. Soljacic. Bound states in the continuum. *Nature Reviews Materials 2016 1:9*, 1:1–13, 7 2016. ISSN 2058-8437. doi: 10.1038/natrevmats.2016.48.

[29] Y. Intaravanne and X. Chen. Recent advances in optical metasurfaces for polarization detection and engineered polarization profiles. *Nanophotonics*, 9:1003–1014, 5 2020. ISSN 21928614. doi: 10.1515/NANOPH-2019-0479/XML.

[30] M. Iwanaga, T. Mano, and N. Ikeda. Superlinear photoluminescence dynamics in plasmon-quantum-dot coupling systems. *ACS Photonics*, 5:897–906, 3 2018. ISSN 23304022. doi: 10.1021/ACSPHOTONICS.7B01142/SUPPL_FILE/PH7B01142_SI_001.PDF.

[31] S. Jahani and Z. Jacob. All-dielectric metamaterials. *Nature nanotechnology*, 11:23–36, 1 2016. ISSN 1748-3395. doi: 10.1038/NNANO.2015.304.

[32] F. Jahnke, C. Gies, M. Aßmann, M. Bayer, H. A. Leymann, A. Foerster, J. Wiersig, C. Schneider, M. Kamp, and S. Höfling. Giant photon bunching, superradiant pulse emission and excitation trapping in quantum-dot nanolasers. *Nature Communications 2016 7:1*, 7:1–7, 5 2016. ISSN 2041-1723. doi: 10.1038/ncomms11540.

[33] M. Kasha, H. R. Rawls, and M. A. El-Bayoumi. The exciton model in molecular spectroscopy.

[34] S. G. Kim, K. C. Yang, Y. J. Shin, K. N. Kim, D. W. Kim, J. Y. Lee, Y. H. Kim, and G. Y. Yeom. Etch characteristics of si and tio2 nanostructures using pulse biased inductively coupled plasmas. *Nanotechnology*, 31, 4 2020. ISSN 1361-6528. doi: 10.1088/1361-6528/AB7C75.

[35] K. Koshelev, S. Lepeshov, M. Liu, A. Bogdanov, and Y. Kivshar. Asymmetric metasurfaces with high- q resonances governed by bound states in the continuum. *Physical Review Letters*, 121:193903, 11 2018. ISSN 10797114. doi: 10.1103/PHYSREVLETT.121.193903/FIGURES/4/MEDIUM.

[36] A. E. Krasnok, A. E. Miroshnichenko, P. A. Belov, Y. S. Kivshar, A. E. Miroshnichenko, I. S. Maksymov, A. R. Davoyan, C. Simovski, P. Belov, and Y. S. Kivshar. All-dielectric optical nanoantennas. *Optics Express, Vol. 20, Issue 18, pp. 20599-20604*, 20:20599–20604, 8 2012. ISSN 1094-4087. doi: 10.1364/OE.20.020599.

[37] K. Kreger, H.-W. Schmidt, R. Hildner, J. L. Bricks, Y. L. Slominskii, I. D. Panas, and A. P. Demchenko. Fluorescent j-aggregates of cyanine dyes: basic research and applications review. *Methods and Applications in Fluorescence*, 6:012001, 12 2017. ISSN 2050-6120. doi: 10.1088/2050-6120/AA8D0D.

[38] A. I. Kuznetsov, A. E. Miroshnichenko, Y. H. Fu, J. Zhang, and B. Lukyanchukl. Magnetic light. *Scientific reports*, 2, 2012. ISSN 2045-2322. doi: 10.1038/SREP00492.

[39] A. I. Kuznetsov, A. E. Miroshnichenko, M. L. Brongersma, Y. S. Kivshar, and B. Luk'yanchuk. Optically resonant dielectric nanostructures. *Science*, 354, 11 2016. ISSN 10959203. doi: 10.1126/SCIENCE.AAG2472/ASSET/09279978-9118-4F9D-87D7-13E96218B962/ASSETS/GRAPHIC/354_AAG2472_FA.JPEG.

[40] K. H. Li, X. Liu, Q. Wang, S. Zhao, and Z. Mi. Ultralow-threshold electrically injected algan nanowire ultraviolet lasers on si operating at low temperature. *Nature Nanotechnology 2014 10:2*, 10:140–144, 1 2015. ISSN 1748-3395. doi: 10.1038/nnano.2014.308.

[41] J. A. Liddle, G. M. Gallatin, and L. E. Ocola. Resist requirements and limitations for

nanoscale electron-beam patterning. *Materials Research Society Symposium - Proceedings*, 739:19–30, 2002. ISSN 02729172. doi: 10.1557/PROC-739-H1.5.

[42] M. Liu and D. Y. Choi. Extreme huygens' metasurfaces based on quasi-bound states in the continuum. *Nano Letters*, 18:8062–8069, 12 2018. ISSN 15306992. doi: 10.1021/ACS.NANOLETT.8B04774/SUPPL_FILE/NL8B04774_SI_001.PDF.

[43] W. Liu, Z. Li, H. Cheng, and S. Chen. Dielectric resonance-based optical metasurfaces: From fundamentals to applications. *iScience*, 23:101868, 12 2020. ISSN 2589-0042. doi: 10.1016/J.ISCI.2020.101868.

[44] B. S. Luk'Yanchuk, N. V. Voshchinnikov, R. Paniagua-Domínguez, and A. I. Kuznetsov. Optimum forward light scattering by spherical and spheroidal dielectric nanoparticles with high refractive index. *ACS Photonics*, 2:993–999, 7 2015. ISSN 23304022. doi: 10.1021/ACSPHOTONICS.5B00261/SUPPL_FILE/PH5B00261_SI_001.PDF.

[45] V. R. Manfrinato, L. Zhang, D. Su, H. Duan, R. G. Hobbs, E. A. Stach, and K. K. Berggren. Resolution limits of electron-beam lithography toward the atomic scale. *Nano letters*, 13: 1555–1558, 4 2013. ISSN 1530-6992. doi: 10.1021/NL304715P.

[46] S. J. Masson and A. Asenjo-Garcia. Universality of dicke superradiance in arrays of quantum emitters. *Nature Communications 2022 13:1*, 13:1–7, 4 2022. ISSN 2041-1723. doi: 10.1038/s41467-022-29805-4.

[47] F. Meinardi, M. Cerminara, A. Sassella, R. Bonifacio, and R. Tubino. Superradiance in molecular h aggregates. *Physical Review Letters*, 91:247401, 12 2003. ISSN 10797114. doi: 10.1103/PHYSREVLETT.91.247401/FIGURES/2/MEDIUM.

[48] D. Melnikau, D. Savateeva, A. Susha, A. L. Rogach, and Y. P. Rakovich. Strong plasmon-exciton coupling in a hybrid system of gold nanostars and j-aggregates. *Nanoscale Research Letters*, 8:1–6, 3 2013. ISSN 1556276X. doi: 10.1186/1556-276X-8-134/FIGURES/6.

[49] J. Moll, S. Daehne, J. R. Durrant, and D. A. Wiersma. Optical dynamics of excitons in j aggregates of a carbocyanine dye. *The Journal of Chemical Physics*, 102:6362, 6 1998. ISSN 0021-9606. doi: 10.1063/1.1703017.

[50] M. Müller, A. Paulheim, A. Eisfeld, and M. Sokolowski. Finite size line broadening and superradiance of optical transitions in two dimensional long-range ordered molecular aggregates. *The Journal of chemical physics*, 139, 7 2013. ISSN 1089-7690. doi: 10.1063/1.4813521.

[51] L. Novotny and N. V. Hulst. Antennas for light. *Nature Photonics 2011 5:2*, 5:83–90, 2 2011. ISSN 1749-4893. doi: 10.1038/nphoton.2010.237.

[52] Y. Obara, K. Saitoh, M. Oda, and T. Tani. Room-temperature fluorescence lifetime of pseudoisocyanine (pic) j excitons with various aggregate morphologies in relation to micro-

cavity polariton formation. *International journal of molecular sciences*, 13:5851–5865, 5 2012. ISSN 1422-0067. doi: 10.3390/IJMS13055851.

[53] S. Prakash and J. Yeom. Advanced fabrication methods and techniques. *Nanofluidics and Microfluidics*, pages 87–170, 2014. doi: 10.1016/B978-1-4377-4469-9.00004-4.

[54] E. M. Purcell, H. C. Torrey, and R. V. Pound. Resonance absorption by nuclear magnetic moments in a solid. *Physical Review*, 69, 1 1946. doi: 10.1103/PhysRev.69.37.

[55] M. Qin, S. Xiao, S. Xiao, W. Liu, M. Ouyang, T. Yu, T. Yu, T. Wang, and Q. Liao. Strong coupling between excitons and magnetic dipole quasi-bound states in the continuum in ws<sub>2</sub>-tio<sub>2</sub> hybrid metasurfaces. *Optics Express, Vol. 29, Issue 12, pp. 18026-18036*, 29:18026–18036, 6 2021. ISSN 1094-4087. doi: 10.1364/OE.427141.

[56] G. Rainò, M. A. Becker, M. I. Bodnarchuk, R. F. Mahrt, M. V. Kovalenko, and T. Stöferle. Superfluorescence from lead halide perovskite quantum dot superlattices. *Nature 2018 563:7733*, 563:671–675, 11 2018. ISSN 1476-4687. doi: 10.1038/s41586-018-0683-0.

[57] U. D. Rossi, J. Moll, M. Spieles, G. Bach, S. Dähne, J. Kriwanek, and M. Lisk. Control of the j-aggregation phenomenon by variation of the n-alkyl-substituents. *Journal für Praktische Chemie/Chemiker-Zeitung*, 337:203–208, 1 1995. ISSN 1521-3897. doi: 10.1002/PRAC.19953370144.

[58] M. K. Schmidt, R. Esteban, J. J. Sáenz, I. Suárez-Lacalle, S. Mackowski, and J. Aizpurua. Dielectric antennas–a suitable platform for controlling magnetic dipolar emission. *Optics express*, page 13636, 6 2012. ISSN 1094-4087. doi: 10.1364/OE.20.013636.

[59] T. Shi, Z. L. Deng, G. Geng, X. Zeng, Y. Zeng, G. Hu, A. Overvig, J. Li, C. W. Qiu, A. Alù, Y. S. Kivshar, and X. Li. Planar chiral metasurfaces with maximal and tunable chiroptical response driven by bound states in the continuum. *Nature Communications 2022 13:1*, 13: 1–8, 7 2022. ISSN 2041-1723. doi: 10.1038/s41467-022-31877-1.

[60] F. C. Spano. The spectral signatures of frenkel polarons in h- and j-aggregates. *Accounts of Chemical Research*, 43:429–439, 3 2010. ISSN 00014842. doi: 10.1021/AR900233V/ASSET/IMAGES/MEDIUM/AR-2009-00233V_0001.GIF.

[61] I. Staude, A. E. Miroshnichenko, M. Decker, N. T. Fofang, S. Liu, E. Gonzales, J. Dominguez, T. S. Luk, D. N. Neshev, I. Brener, and Y. Kivshar. Tailoring directional scattering through magnetic and electric resonances in subwavelength silicon nanodisks. *ACS Nano*, 7:7824–7832, 9 2013. ISSN 19360851. doi: 10.1021/NN402736F/ASSET/IMAGES/MEDIUM/NN-2013-02736F_0008.GIF.

[62] A. Taflove and S. C. Hagness. The finite-difference time-domain method third edition. pages 51–273, 2005.

[63] J. B. Trebbia, Q. Deplano, P. Tamarat, and B. Lounis. Tailoring the superradiant and subradiant nature of two coherently coupled quantum emitters. *Nature Communications 2022 13:1*, 13:1–9, 5 2022. ISSN 2041-1723. doi: 10.1038/s41467-022-30672-2.

[64] P. Törmö and W. L. Barnes. Strong coupling between surface plasmon polaritons and emitters: a review. *Reports on Progress in Physics*, 78:013901, 12 2014. ISSN 0034-4885. doi: 10.1088/0034-4885/78/1/013901.

[65] K. J. Vahala. Optical microcavities. *Nature 2003 424:6950*, 424:839–846, 2003. ISSN 1476-4687. doi: 10.1038/nature01939.

[66] P. Vasa, R. Pomraenke, G. Cirmi, E. D. Re, W. Wang, S. Schwieger, D. Leipold, E. Runge, G. Cerullo, and C. Lienau. Ultrafast manipulation of strong coupling in metal-molecular aggregate hybrid nanostructures. *ACS Nano*, 4:7559–7565, 12 2010. ISSN 19360851. doi: 10.1021/NN101973P/SUPPL_FILE/NN101973P_SI_003.ZIP.

[67] Z. Wang, T. Li, A. Soman, D. Mao, T. Kananen, and T. Gu. On-chip wavefront shaping with dielectric metasurface. *Nature Communications 2019 10:1*, 10:1–7, 8 2019. ISSN 2041-1723. doi: 10.1038/s41467-019-11578-y.

[68] Q. Wei, L. Huang, T. Zentgraf, and Y. Wang. Optical wavefront shaping based on functional metasurfaces. *Nanophotonics*, 9:987–1002, 5 2020. ISSN 21928614. doi: 10.1515/NANOPH-2019-0478/ASSET/GRAPHIC/J_NANOPH-2019-0478_FIG_002.JPG.

[69] F. Würthner, T. E. Kaiser, and C. R. Saha-Möller. J-aggregates: from serendipitous discovery to supramolecular engineering of functional dye materials. *Angewandte Chemie (International ed. in English)*, 50:3376–3410, 4 2011. ISSN 1521-3773. doi: 10.1002/ANIE.201002307.

[70] J. Xiang, Y. Xu, J. D. Chen, and S. Lan. Tailoring the spatial localization of bound state in the continuum in plasmonic-dielectric hybrid system. *Nanophotonics*, 9:133–142, 1 2020. ISSN 21928614. doi: 10.1515/NANOPH-2019-0341/ASSET/GRAPHIC/J_NANOPH-2019-0341_FIG_006.JPG.

[71] P. Xie, Z. Liang, Z. Li, W. Wang, W. Wang, T. Xu, X. Kuang, L. Qing, D. Li, and J. Yi. Coherent and incoherent coupling dynamics in a two-dimensional atomic crystal embedded in a plasmon-induced magnetic resonator. *Physical Review B*, 101:045403, 1 2020. ISSN 24699969. doi: 10.1103/PHYSREVB.101.045403/FIGURES/5/MEDIUM.

[72] A. Yoshida and N. Kometani. Effect of the interaction between molecular exciton and localized surface plasmon on the spectroscopic properties of silver nanoparticles coated with cyanine dye j-aggregates. *Journal of Physical Chemistry C*, 114:2867–2872, 2 2010. ISSN 19327447. doi: 10.1021/JP9081454/ASSET/IMAGES/MEDIUM/JP-2009-081454_0009.GIF.

[73] N. Yu and F. Capasso. Flat optics with designer metasurfaces. *Nature materials*, 13: 139–150, 2014. ISSN 1476-4660. doi: 10.1038/NMAT3839.

[74] Q. Zhao, J. Zhou, F. Zhang, and D. Lippens. Mie resonance-based dielectric metamaterials. *Materials Today*, 12:60–69, 12 2009. ISSN 1369-7021. doi: 10.1016/S1369-7021(09)70318-9.

List of Figures

2.1 Schematic representation of the spectral changes following the formation of H- and J- aggregates in cyanine dyes [37]. 6
2.2 Fluorescence spectra of two coupled terrylene molecules as a function of pumping power, showing the arisal of a pump fluence dependent peak associated with the emergence of cooperative emission [27]. 8

3.1 a) Electric and magnetic field vector components for a cubic unit cell in the Yee lattice [62]. b) Schematic representation of the leapfrog phenomenon introduced by Yee in his algorithm [62]. 12
3.2 Schematic representation of the possible positions the TDBC thin film might assume after spincoating. a) TDBC film between the TiO_2 pillars. b) TDBC film perfectly on top of the metasurface. c) TDBC film completely filling the free volume of the metasurface. 13
3.3 a) Real (blue) and imaginary (orange) refractive index of the TDBC:PVA thin film. b) Refractive index of the TiO_2 thin film. 14
3.4 a) Normal-incidence transmission spectra of cylinders of multiple radii in the form of a 2D colormap. b) Magnetic dipole (MD) and electric dipole (ED) resonances forming bands as a function of the radii of the cylindrical resonators. 20
3.5 a) Top view of the unit cell. b,c) Electric field distribution for the magnetic dipole (MD) Mie resonance. The latter univocally identifies the optical resonance. . . . 21
3.6 a) Top view of the unit cell. b,c) Electric field distribution for the electric dipole (ED) Mie resonance. The latter univocally identifies the optical resonance. 21
3.7 2D colormap representing the MD and ED bands formed by sweeping the thickness of the TDBC molecular aggregate thin film in its passive form (left). 2D colormap representing the MD and ED bands formed by sweeping the radii of the dielectric resonators with the TDBC molecular thin film in its active form (right). 22
3.8 a)Exciton-polariton bands arising due to the coupling between the ED-based metasurface ($R = 155\ nm$) and the absorbing molecular aggregate thin film. b) Exciton-polariton bands arising due to the coupling between the ED-based metasurface and the absorbing molecular aggregate thin film as a function of the thickness of the active dissipative molecular aggreate film. 23

3.9 2D colourmap representing the transmittance of the passive (right) and active (left) structures with respect to different thicknesses of the TDBC thin film for the MD resonance configuration (R=120 nm). The upper (UP) and lower polaritons (LP) are identified by the white dashed lines. 25

3.10 2D colourmap representing the transmittance of the passive (right) and active (left) structures with respect to different thicknesses of the TDBC thin film for the ED resonance configuration (R=130 nm). The upper (UP) and lower polaritons (LP) are identified by the white dashed lines. 25

3.11 Simulated angle-resolved transmission spectra for cylindrical resonators of radii $R = 120\ nm$ (a), $R = 130\ nm$ (b), and $R = 155\ nm$ (c) covered by the TDBC film in its passive form. The angular dispersion of the resonances (white dashed lines) was designed to overlap with the excitonic peak to couple efficiently. 27

3.12 a) Simulated normal-incidence transmittance spectrum for cylindrical resonators of $R = 120\ nm$ in its passive (blue) and active (orange) form. b) Simulated angle-resolved transmittance spectrum highlighting the lower polariton band for the MD-based resonance ($R = 120\ nm$). c) Simulated normal-incidence transmittance spectrum for a cylindrical resonator of $R = 130\ nm$ in its passive (blue) and active (orange) form. d) Simulated angle-resolved transmittance spectrum highlighting the lower polariton band for the ED-based resonance ($R = 130\ nm$). 28

3.13 Schematic representation of the formation of a bound state in the continuum [28]. 30

3.14 a) Top view of the unit cell. b,c) Electric field distribution for the ED quasi-bound state in the continuum resonance. The latter univocally identifies the optical resonance. 31

3.15 a) 2D colourmap representing the relation between the parameter of asymmetry (θ) and the resonance linewidth of the passive structure of the electric dipole quasi-bound state in the continuum optical resonance, showing the linewidth becoming infinitely small towards the condition for a perfect BIC (θ=90). b-c) 2D colourmap of the optical response of the ED Q-BIC resonance to changes in thickness (b) of the TDBC film and the asymmetry parameter (c) for the active structure. 32

3.16 a) Simulated normal-incidence transmittance spectrum for the ED Q-BIC structure in its passive (blue) and active (orange) form. b) Simulated angle-resolved transmittance spectrum highlighting the lower polariton band for the ED Q-BIC structure formed due to strong coupling between the metasurface and the active non-dissipative molecular aggregate thin film. 33

3.17 a) Simulated angle-resolved spectrum showing the angular dispersion of the ED Q-BIC resonance for the passive structure. b) Simulated angle-resolved transmittance spectrum highlighting the upper and lower polariton bands for the ED Q-BIC structure formed due to strong coupling between the metasurface and the active non-dissipative molecular aggregate thin film. The emergence of exciton-polaritons occurs because of the strong coupling between the active film and the metasurface. 34

4.1 a) Side view of the schematic representation of the fully integrated device. b) Structural formula of 5,6-Dichloro-2-[[5,6-dichloro-1-ethyl-3-(4-sulfobutyl)-benzimidazol-2-ylidene]-propenyl]-1-ethyl-3-(4-sulfobutyl)-benzimidazolium hydroxide, inner salt, sodium salt in its monomeric form. c) and d) SEM images of fully formed TBDC J-aggregates in two distinct supramolecular structures covered by a thin layer of gold. 38
4.2 Photoluminescence spectrum during the first hour (a) and 16 hours (b) of in-solution growth of the TDBC J-aggregate. The photoluminescence peak if the J-aggregate is shown to be growing in intensity with time, meaning that the monomers have not yet fully converted into J-aggregates. 40
4.3 a) Photoluminescence spectrum of grown TDBC J-aggregate thin films of different starting monomer concentrations. b) Double logarithmic plot of grown TDBC J-aggregate thin films of different starting monomer concentrations showing the peak emittance reaching saturation with increasing monomer concentrations. . . 41
4.4 Schematic representation of the sample preparation according to the resist supplier (Allresist). 44
4.5 SEM images of TiO_2 Mie resonances based metasurface after EBL exposure. . . . 45
4.6 SEM images of TiO_2 BIC-based metasurface after EBL exposure. 45
4.7 Schematic representation of the fabrication process using a chromium hard mask. a) Unpatterned sample. b) EBL exposure and development of HSQ resist. c) ICP-RIE of Cr hard mask. d) CHF_3 RIE of TiO_2. e) Cr wet etching. 49
4.8 SEM images of the cylinders-based metasurface throughout the fabrication process. 49
4.9 SEM images of the BIC-based metasurface throughout the fabrication process. . 49

5.1 Schematic representation of the fabricated arrays. a) Sequence of arrays associated to different dosages employed during EBL. b) Optical micrograph for one of the EBL dosages. c) Schematic representation of the unit cells for the three optical resonances. 51

5.2 Experimental (dotted) and simulated (continuous line) transmittance spectra of the magnetic dipole (left) and electric dipole (right) Mie resonances. The respective dips in transmittance are shown to overlap with the emission wavelength of the J-aggregate (589 nm). The inset shows the simplified schematics of the optical setup used for the measurements. 52
5.3 Comparison between the simulated (a) and experimental (b,c) normal-incidence transmittance for unit cells of different radii for samples S1 and S2. The MD and ED bands are shown to perfectly match between the experimental and calculated results for S1. The bands of the fabricated arrays of sample S2 are blueshifted with respect to the simulated results because of fabrication tolerances. 53
5.4 Experimental normal-incidence transmittance measurements for the Q-BIC resonances in sample S1 shown not to match the experimental results due to fabrication tolerances. 54
5.5 Experimental normal-incidence photoluminescence spectrum of TDBC J-aggregates dispersed in a PVA matrix showing the low-intensity 535 nm monomer emission and the significantly stronger 589 nm J-aggregate emission. 55
5.6 a) PL measurements as a function of pumping power for sample A. b) PL measurements as a function of pumping power for sample B. Both samples show preliminary evidence of non-linear emission. 56
5.7 a,b) Normal-incidence photoluminescence measurements for sample A (a) and B (b). c) Double logarithmic plot of the normalized peak intensity of photoluminescence against the pumping power showing a noticeable change in trend associated to cooperative emission. 57
5.8 Schematics of the optical setup utilized for AR-PL measurements. 59
5.9 Simulated passive spectrum (a) and measured ARPL spectrum (b,c) for the normal-incidence MD dipole resonance of two distinct samples (S1 in (b) and S3 in (c)) showing varying degrees of coupling between the J-aggregate thin film and the dielectric metasurface. 60
5.10 Simulated passive spectrum (a) and measured ARPL spectrum (b,c) for the normal-incidence ED resonance of two distinct samples (S1 in (b) and S3 in (c)) showing varying degrees of coupling between the J-aggregate thin film and the dielectric metasurface. 61
5.11 Simulated passive spectrum (a) and measured ARPL spectrum (b,c) for the higher angles ED resonance of two distinct samples (S1 in (b) and S3 in (c)) showing varying degrees of coupling between the J-aggregate thin film and the dielectric metasurface. 61

5.12 Simulated passive spectrum (a) and measured ARPL spectrum (b) for the symmetry protected electric dipole quasi-bound state in the continuum optical resonance. The band structure of the measured spectrum perfectly matches the shape of the simulated band structure but is redshifted and thus not overlapping with excitonic peak. 62

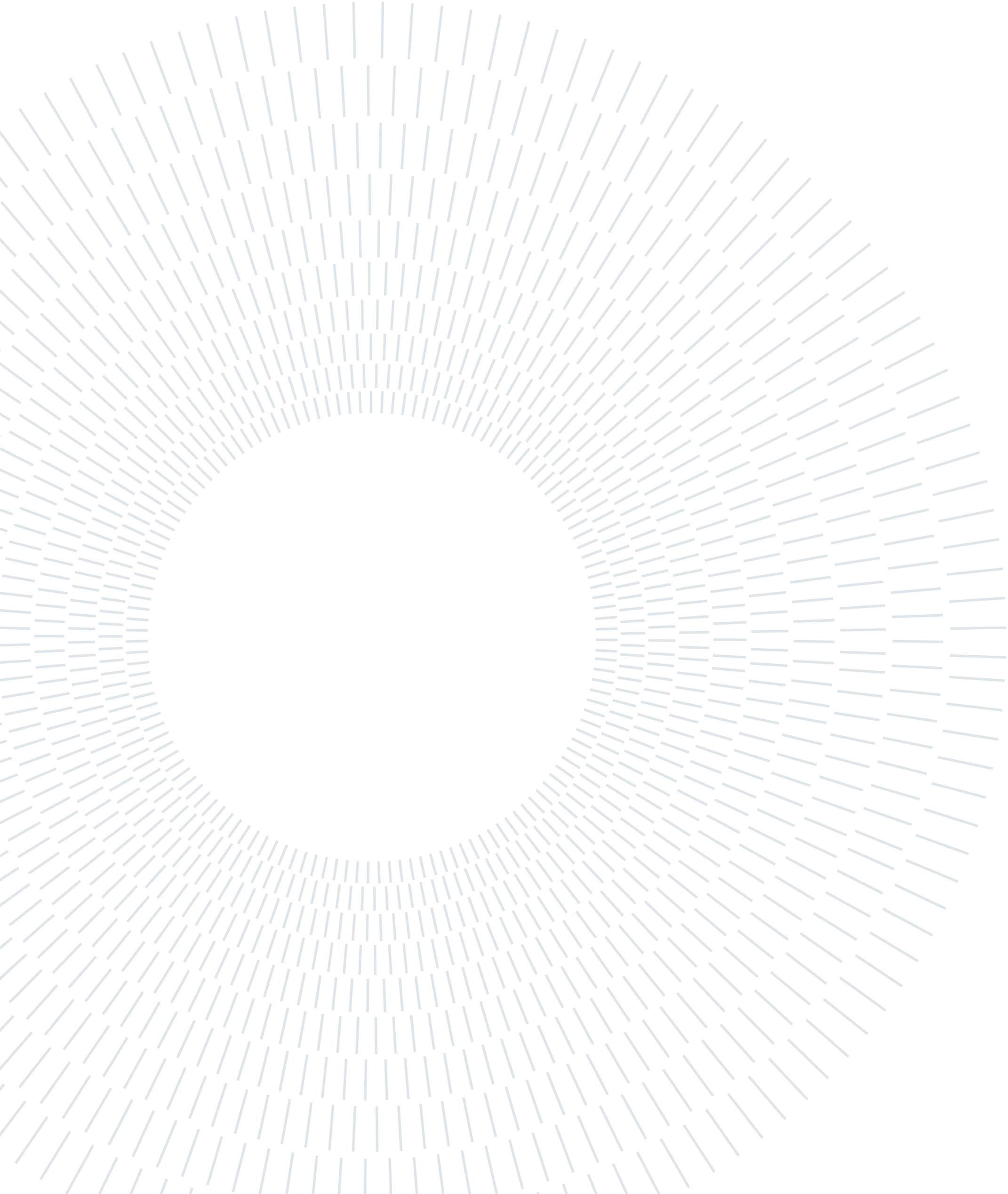

List of Tables

4.1 Table of all operating parameters tested to dry etch TiO_2 48

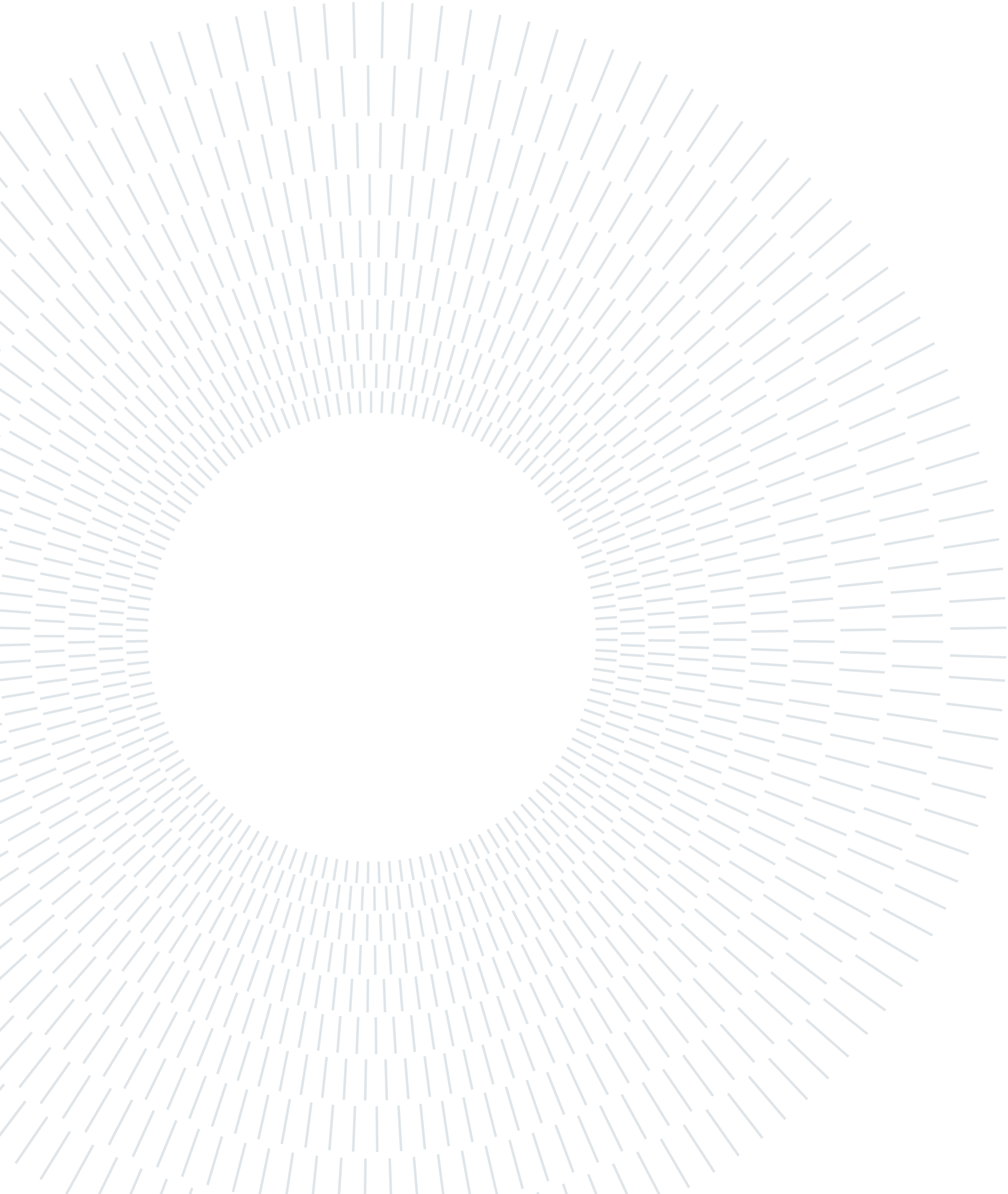

Acknowledgements

All work presented in this thesis has been supervised by Professor Cesare Soci from the Centre of Disruptive Photonic Technologies in Nanyang Technological University (NTU), Singapore, and co-supervised by Professor Guglielmo Lanzani from the Center for Nano Science and Technology (CNST), IIT, Milan.

The author would also like to specifically express his gratitude towards Dr. Giorgio Adamo for helping with the fabrication process and overall structure of the project; Dr. Jingyi Tian for aiding the design process; Dr. Maciej Klein for his help during the pump fluence measurements; PhD candidate Yutao Wang for his experimental work on angle-resolved photoluminescence.

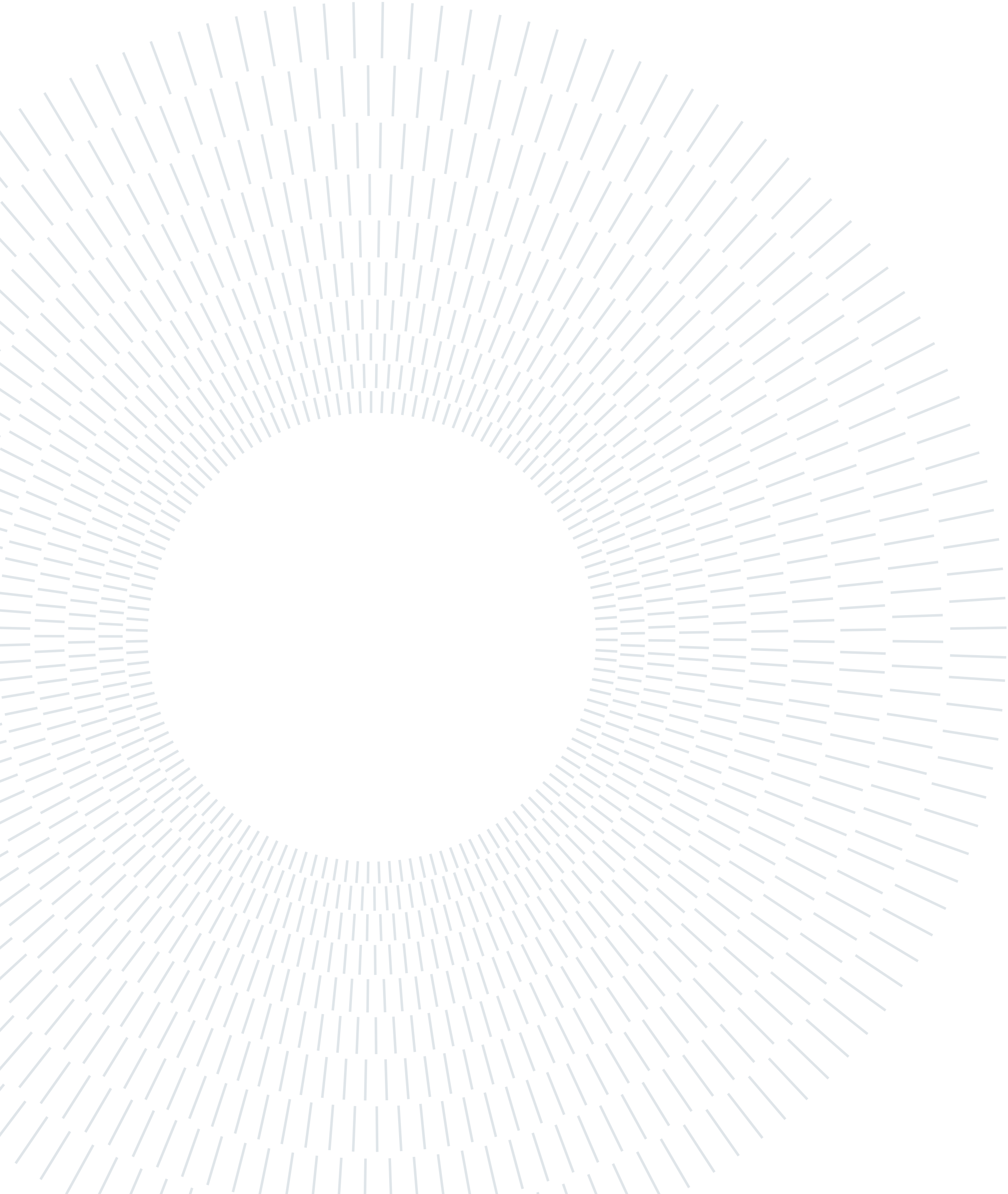This work would not have been possible without the help provided by the Institute of Materials Research and Engineering (IMRE), A*STAR, for the fabrication of the TiO_2 metasurfaces. Special thanks to Dr. Mengfei Wu for her work with electron-beam lithography and coordination of the efforts between all other contributors from IMRE: Febi Tjiptoharsono (etching); Vytautas Valuckas, Bhumika Chaudhary, and Yuxiang Zhang (SEM imaging).